In vivo evaluation of hepatic hemodynamics and tissue morphology on the basis of diffuse reflectance spectroscopy

Dissertation submitted for the degree of
Doctor of Philosophy
in Engineering
March, 2017

by
Sharmin Akter

Tokyo University of Agriculture and Technology
Graduate School of Bio-Applications and Systems Engineering
Koganei, Tokyo, Japan

CONTENTS

Chapter 1

Introduction

1.1 General Review for tissue Optics

Biomedical optics is often considered as a new scientific field, even if the optical diagnosis of tissue has a long history in medicine. Optical spectroscopy techniques have in recent years been increasingly investigated in the search for novel, minimally or non-invasive and low cost methods for numerous applications in the field of medicine. The common basis of these optical techniques is that physiological, morphological or biochemical alterations related to the advancement of disease, affecting the light-tissue interaction, that can be effectively determined in spectroscopic measurements. Reflectance spectroscopy is a well-known, easy manageable technique to get information about optical properties of biological tissues. Probe based diffuse reflectance spectroscopy, utilizes light delivered and collected through a optical fiber probe, having the ability of measuring structural and functional property of tissue noninvasively and without causing damage to the tissue [1]. A large variety of spectroscopic techniques have been proposed to characterize the tissue property and pathology, such as, Raman spectroscopy, fluorescence spectroscopy, phosphorescence spectroscopy, and diffuse reflectance spectroscopy. The work presented in current dissertation will be restricted to the diffuse reflectance spectroscopy and spectrocolorimetry in the wavelength range of 400-900 nm and focus on its application to diagnose the hepatic ischemia-reperfusion injury of *in vivo* rat evoked by occlusion of hepatic portal.

When light enters into the biological tissue, it is diffusely reflected. Light propagation in the biological tissue is dependent upon the absorption coefficient (μ_a), and reduced scattering coefficient (μ_s') of the tissue, where μ_a relates to the chromophore concentrations of

chromophores in the tissue such as oxygenated hemoglobin, deoxygenated hemoglobin, and Cytochrome c oxidase, and μ_s' describes the scatterers size and density. The dominant absorber in the biological tissue is hemoglobin, and because of different absorption shape of oxy- and deoxyhemoglobin, DRS could be used to distinguish between the two, thus providing independent concentration measurements and a calculated tissue oxygen saturation [2]. One of the primary tasks of tissue optics is to measure the changes in μ_a and μ_s' from the measured diffuse reflectance spectra. Light is both absorbed and scattered by blood and other cellular structures of tissues, and thus a suitable light propagation model is necessary to deconstruct the diffuse reflectance spectrum [2].

Four models that are mostly used to numerically and analytically evaluate the absorption coefficients from diffuse reflectance spectra, such as, radiative transfer equation (RTE), Monte Carlo (MC) method, empirical methods, and Mie theory. Whereas the first three techniques consider light as a flow of photon travelling through the tissue, and the final one considers light as an electromagnetic wave.

Radiative Transfer Equation:

The Radiative Transfer Equation (RTE) is an energy balance equation that can mathematically explains the movement of light in biological tissue [3]. The RTE mainly depend on energy transfer through the biological tissue which has a consistent form of

$$\hat{s}\cdot\nabla I(\vec{r},\hat{s})+\mu_t(\vec{r})I(\vec{r},\hat{s})=\mu_s(\vec{r})\int_{4\pi}p(\hat{s},\hat{s}')I(\vec{r},\hat{s}')d\vec{w}'+S(\vec{r},\hat{s}) \qquad (1.1)$$

In the above equation $I(\vec{r},\hat{s})$ is the radiance [W/(m^2.sr)] towards the $\hat{s}$ direction per unit solid angle and per unit area at location $\vec{r}$, μ_t denotes total extinction coefficient [1/m], μ_s is scattering coefficient [1/m], p is scattering phase function [1/sr], and S is the source term which equivalents to the power generated at $\vec{r}$ in the $\hat{s}$ direction [W/(m^3.sr)]. As there is no typical solution accessible on this equation, an analytical approximation is considered to

reproduce diffuse scattering. A general analytical approximation of RTE is known as the diffusion equation.

The diffusion approximation to the RTE, is appropriate in case of large source-detector separation and where the absorption contrast is less than scattering [1]. There are some approximate analytical theories or numerical methods such as diffusion approximation, random walk method, and Kubelka-Munk theory. Diffusion approximation is an analytical hypothesis to the RTE using boundary conditions and thoughts that the source is quasi-isotropic, and that the time variation of the source is slow in compare to the mean photon collision time [4].

Diffusion Approximation*:* The diffusion model is an assumption of the radiative transfer equation is commonly used to explain photon propagation in scattering rich media. Usually biological tissues are strongly scattering and very weekly absorbing in the near-infrared light, until it is inhomogeneous and may carry comparatively high absorbing or low-scattering areas. When the mean free path of photon is small the Radiative Transfer Equations (RTE) may be approximated by a nonlinear angular diffusion equation. The diffusion theory is considered to arbitrary locally isotropic participating media. It demonstrates to be a general solution of the whole equation of radiative transfer treating for absorption, scattering and emission. The approximation can be solved for homogenously diffusing media over different geometries and boundary conditions for e.g., infinitely extended medium, semi-infinite slab, finite slab, cylinder, and sphere. GUO et. al. [5] demonstrated the conditions that, where and when the diffusion theory can be used and the situations in which the diffusion equation can give confusing results. The diffusion theory is believed for giving acceptable results to describe photon transport at big source-detector separations for strongly scattering biological tissues.

Random walk method: Random walk model of photon propagation is applied to the problem of light migration in turbid media. Photon diffusion in the scattering medium is approximated as a random movement on a simple cubic grid. Photon proceeds through the grid as steps to one of six closest adjacent grid points. By using this simple scheme, it is possible to get analytical relationships similar to that obtained using the diffusion approximation [6].

***Kubelka-Munk Theory*:** The kubelka-Munk (K-M) method explains the interaction of light with a surface utilizing two light fluxes in opposite direction. Kubelka-Munk model or two flux model can be considered as a clarified one dimensional diffusion model discounting reflections at the boundaries. In this theory the volume scattering and absorption can be resolved shortly from the reflectance and transmission measurements [7]. The medium is defined by absorption coefficient, μ_a and the reduced scattering coefficient μ_s'. Approximations of the K-M model are that the surface of the tissue is infinitely wide (no edge effects), the light scattering particles are equally dispersed, particle sizes are small compare to the tissue thickness and that the entire tissue is homogenously irrediated by a monochromatic diffuse light source [8].

In the exceptional case of diffuse reflectance, if the tissue thickness is supposed infinitely wide, the K-M model minimizes into a simpler form:

$$\frac{\mu_a}{\mu_s'} = \frac{(1-R^2)}{2R} \equiv f(R), \tag{1.2}$$

Here $f(R)$ is the K-M function [9]. Since $\mu_a = \alpha c$, the relationship between the reflectance and the chromophore concentration can be expressed as:

$$f(R) = \frac{\alpha c}{\mu_s'}, \tag{1.3}$$

representing that the K-M function is linearly proportional to the chromophore concentration of tissue.

Monte Carlo Modeling:

Monte Carlo simulation is a numerical simulation model for the RTE, which is suitable for a wider range of wavelengths and optical properties compare to the diffusion approximation, although it suffers from computational time [10]. The Monte Carlo method involves random sampling of probability density functions linked to the absorption and scattering properties of a tissue or medium. This method treats light as particles and traces three dimensional random walks of photons in a medium. The two key components in Monte Carlo simulation are the scattering angle and the mean-free path length for a photon-tissue interaction. The mean free path length is defined by the possibility that a photon is either absorbed or scattered after a given step size. This possibility is resolved by local optical properties: such as the absorption coefficient μ_a, and the scattering coefficient μ_s. Likewise, the scattering angle is defined by the anisotropy factor g. By using a random number generator, the trajectories of emitted light are chosen according to the statistical rules relevant for photon propagation through the tissue. The trajectory of any emitted photon is followed until it exits from the scattering medium or it arrives at the detector. The Monte Carlo method allows a full-dimensional description of photon propagation and the actual scattering properties of tissue can be taken into account in the simulation. When modeling multilayered tissues, multilayer models are often needed. Each layer is explained by its thickness d, refractive index n, absorption coefficient μ_a, scattering coefficient μ_s, and anisotropy factor g [11]. Internal reflection or refraction at the medium boundaries can also be simulated.

Empirical Method:

Another proposal to inverse method is to use an empirical model. Empirical model do not make explicit assumptions about the light tissue interaction. On the other hand, the idea is to use a classifier to learn the light tissue interaction from experimental data. As for example, Pfefer et al. [12] developed an empirical method for the evaluation of absorption and scattering coefficients from diffuse reflectance spectra. They developed a neural network

with phantoms and then used the network to evaluate optical properties from another set of phantoms.

Mie theory:

Mie theory is an analytical solution of Maxwell's equations which describes the scattering of light by particles [13]. It supposes a homogenous, isotropic, and optically linear material illuminated by an infinitely wide plane wave. Mie theory presumes that the scatterers are spheres of arbitrary dimension, having a homogenous refractive index. Mie theory is often aggregated with the other three theories for estimating the size of scattering particles, after getting the absorption and scattering coefficients of the tissue [14].

The selection of method depends on the tissue studied, although it is common for multiple quantitative methods to be involved to elucidate the biophysics of the light-tissue interaction. The major limitation of all these models, however, is that they either require a priori knowledge of optical parameters or they require simplifying hypothesis, such as sphericity of scattering particles, which would not be physically realistic. Despite their hypothesis, these quantitative methods give valuable understanding into the changes of optical spectra with altering tissue state.

DRS can be measured using steady-state (SS), frequency-domain (FD), or time-domain (TD) instrumentation.

***Steady-state systems*:**

Steady-state diffuse reflectance in the ultraviolet to visible wavelength region involves either a broadband or monochromatic light. The diffuse reflectance spectrum carries information regarding wavelength-dependent absorption and scattering properties of the tissue. The typical instrumentation of a diffuse reflectance spectroscopic system comprises of a broadband light source and a detector, both of which are coupled to a fiber probe and controlled with a personal computer. As the steady-state diffuse reflectance spectroscopic

system described here, were taken in the visible to near infrared wavelength region, where the magnitude of absorption and scattering is comparable, the diffusion approximation would break down and the Monte Carlo modeling was used.

***Frequency domain systems*:** Frequency domain systems, consists of a sinusoidaliy intensity modulated source and heterodyne detection capable of measuring the decrease in modulation depth, and phase shift of the propagated photon density wave, which is a progressively decaying wave of intensity [15]. The phage lag and amplitude attenuation are functions of μ_a and μ_s', which rely on the distance of source-detector separation and modulation frequency of the source [16]. The calculation can involve either different modulation frequencies at one source-detector separation or multiple source-detector separations for one modulation frequency [17].

Time domain systems:

Time domain (TD) studies employ a pulsed light source that emits short light pulses (typically on the order of picoseconds) with a repetition rate of about 1 MHz [18, 19]. Mode-locked solid state lasers, or fast laser diodes are cosidered as the light sources. Photomultiplier tubes and microchannel plates in photon counting mode, or streak cameras are usually employed as the detectors. In the time-domain, one directly measures the time-of-flight distribution of the collected photons, which travel along a set of trajectories that are collectively indicated as a light bundle (shown in fig. 1.1).

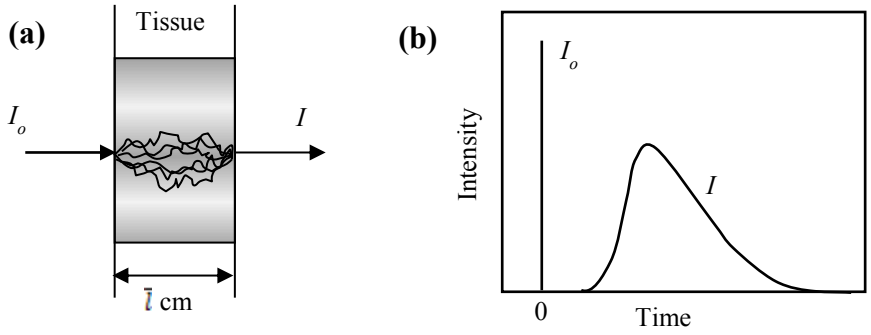

Fig.1.1. (a) Photons that are incident at one point of the tissue (intensity I_0) and that are detected at another point, in transmission in the case illustrated in the figure, (intensity I) travel along a collection of trajectories within the tissue. (b) In the time domain, I_0 is a short (ps) pulse, while I is broadened and delayed on a time scale of nanoseconds as a result of propagation over a tissue thickness $\bar{l}$ of the order of centimeters.

1.2 Motivation

Liver transplantation is the standard of care in patients with severe liver diseases and those with cancers of hepatic origin. During the last few decades, liver surgery has extended extremely, partly due to improved surgical equipment and technologies as well as modern and more efficient chemotherapy agents. As liver is highly vascularized organ, there is an intrinsic risk of bleeding during liver transplantation. One of the most common techniques adopted to overcome this threat, is to occlude the blood supply to the liver employing the Pringle's maneuver [20]. Anyway, this method has been considered to reason ischemia/reperfusion injury to the future liver remnant (FLR). In cases of severe excision where the future liver remnant is minor and in a situation when the liver suffer from chronic diseases such as cirrhosis, the ischemia-reperfusion injury could significantly raise the possibility of post-operative liver failure (POLF). Ischemic pre-conditioning and, more recently, remote ischemic preconditioning are techniques that have been involved to reduce ischemia-reperfusion injury. Blood loss can be reduced in various ways that range from

segmental portal control to total vascular occlusion of the major hepatic vessels and each is coupled with side effects [21].

Ischemia-reperfusion injury (IRI) is a vital reason of liver failure occurring throughout hepatic resection surgery and liver transplantation, which constitutes the main underlying reason of post-transplant graft dysfunction. Cellular and biochemical changes happening during hepatic ischemia-reperfusion are multiple and complex, and include the degeneration of the healthy structure of the liver cellular components [22]. IRI not only contributes to the donor organ failure, but might also the main underlying cause of early graft rejection and primary non-function. Furthermore, the cellular damage due to neighboring organ transfer and storage affects transplantation outcome as it is an important risk factor for both acute and chronic rejection. In spite of its clear clinical importance, the mechanisms which account for liver IRI are only partly understood and undergo one of the most understudied areas in clinical and experimental transplantation [22, 23].

Since hemoglobin is the primary absorber in biological tissues, the seriousness of liver ischemia-reperfusion can be reliably determined by evaluating changes in C_{HbO} and C_{HbR}. The absorption spectrum of hemoglobin varies with the changes of its concentration and oxygenation state, and has a wavelength dependence in visible to near infrared range. By using diffuse reflectance spectroscopy, a number of biochemical features, (such as hemoglobin and oxygen concentration, and tissue's metabolic status) and morphological features (such as scattering size, shape and density, as well as extracellular structures) can be used to differentiate healthy tissue from diseased tissue [24]. Optical imaging with digital RGB color camera is an advantageous mean for extending DRS to spatial mapping of chromophore concentrations of *in vivo* biological tissues. By taking the advantages of diffuse reflectance spectroscopy, the motivation of this research is to apply the diffuse reflectance

spectroscopy and spectrocolorimetry towards an intraoperative application to determine the *in vivo* ischemia-reperfusion injury in rat liver induced by hepatic portal triad occlusion.

1.3 Synopsis of the contents

This dissertation focuses on evaluation of optical properties, hemodynamics and tissue morphology in rat liver during ischemia-reperfusion based on diffuse reflectance spectroscopy (DRS) and spectrocolorimetry. The main purpose of the dissertation is to study the method for evaluating the light scattering and absorption properties as well as hemoglobin concentrations and tissue oxygen saturation (StO_2) of *in vivo* rat liver tissue during ischemia-reperfusion and post mortem. The thesis is based on three papers that have been described the optical properties of liver tissue and diagnostic applications of diffuse reflectance spectroscopy. This dissertation may also be divided into two main parts. The first part describes the fiber probe based diffuse reflectance spectroscopic analysis for evaluating absorption and scattering parameters of exposed rat liver. The second part illustrates the hemodynamics and tissue morphology based on RGB imaging. The dissertation is organized according to the specific aims of this study: In this introduction chapter, the motivation and milestones of this study are presented to give an overview of the dissertation.

Chapter 2 reviews the fundamental theories and principles treated through this dissertation. The Monte Carlo method is mentioned as the quantitative description of light propagation model in the tissue whereas the spectrocolorimetry are explained about the color measurement of an object.

Chapter 3 deals with a pilot *in vivo* study of hepatic ischemia-reperfusion using optical spectroscopy. A diffuse reflectance spectroscopic technique is investigated experimentally by which to measure absorption and scattering properties of *in vivo* liver tissue using a single-reflectance-fiber probe, focusing on evaluations of hepatic hemodynamics and tissue

morphology during pre-ischemia, ischemia-reperfusion, and postmortem. The tissue oxygen saturation of hemoglobin is expressed as the percentage of concentration of oxyhemoglobin in the concentration of total hemoglobin. The StO_2 is estimated from the regression coefficients of oxyhemoglobin and deoxyhemoglobin. Further, the measured absorption coefficient spectrum is used to estimate the redox state of heme in cytochrome c oxidase. The proportion of absorption coefficient at 605 nm to that of at 620 nm is used for evaluating the redox state of heme aa_3, that indicate the condition of mitochondrial energy state. In order to justify the use of $\mu_a(605)/\mu_a(620)$ to depict the redox contition of heme *aa*3 in CcO of liver tissue, preliminary experiment was conducted with an *in vitro* removed liver sample. The results of the experiment represent the possible implimentation of the DRS system for determining the pathophysiological situations and tissue viability of *in vivo* liver tissue.

Chapter 4 demonstrates the evaluation of oxidation of heme *aa*3 in cytochrome c oxidase of *in vivo* hepatic tissue employing a single reflectance fiber probe system with two source-collector configurations. In this chapter, a novel method is proposed to evaluate the oxidation of heme *aa*3 (OH *aa*3) using the regression coefficients of oxidized heme and reduced heme. Hence, the determination on the oxidation of heme *aa*3 is dissimilar from the ratio metric assumption presented in chapter 3 with regard to the use of the regression coefficients of oxidized heme and reduced heme deduced from the Monte Carlo simulation on the basis of multiple regression analysis.

Chapter 5 presents the hemodynamic responses and tissue morphology of *in vivo* liver tissue using a RGB color camera. In this chapter the emphasis is put on the investigation of a method for estimating the concentrations of oxyhemoglobin (C_{HbO}), deoxyhemoglobin (C_{HbR}), total hemoglobin (C_{HbT}), tissue oxygen saturation (StO_2), and scattering power (*b*) in liver tissue acquired from RGB images. This method is applied to imaging hemodynamics in liver tissue during pathophysiologic events such as hepatic inflow occlusion and subsequent

reperfusion. In the proposed technique the RGB values are turned into the tristimulus values, *XYZ* using a color transformation matrix. A Monte Carlo simulation (MCS) model of light propagation for the liver tissue is used to define the correlation among the tristimulus values and the concentrations of oxyhemoglobin, deoxyhemoglobin and scattering power *b*. Images of total hemoglobin concentration and tissue oxygen saturation are regenerated from the determinations of oxygenated hemoglobin and deoxygenated hemoglobin concentrations. *In vivo* trials for rat liver revealed the possibility of the technique to assess the hemodynamics and morphological alterations in liver tissue.

In chapter 6, the research of this thesis is summarized and the discussion of future direction is presented.

Chapter 2

Fundamental Theories and Principles

2.1. Light transport in biological media

Diffuse Reflectance Spectroscopy (DRS) is an optical method which enables the characterization of tissue by measuring the spectral response of light-matter interaction. Light in the wavelength range from visible and infrared is emitted via an optical fiber and, after its absorption and scattering in the biological tissue, the return light is collected with another optical fiber.

Several biomedical photonics research groups are currently studying DRS technology as a minimally invasive or non-invasive procedure for clinical diagnosis like, to discriminate between healthy and cancerous tissue. Another challenge is that physicians are encountering to include DRS as a medical image for percutaneous guidance, to accurately guide interventional tools to the region of interest for an effective treatment. The main aim is to provide a real time feedback on the type of tissue touched by the sensor, such as on the physiological and biological changes in it.

Diffuse reflectance spectroscopy is one of the straightforward and generally used techniques for the non-invasive identification of biological tissue. The method is simple and uncomplicated in its implementation and can be accomplished with cost effective instrumentation. The estimated spectra carry information regarding absorption and scattering characteristics of tissues under study that can be potentially used to accquire some unique features of biochemical composition, structure and morphology of biological tissues [25]. DRS is well characterized to produce two principle sources of information, such as scattering

and absorption. The scattering information is commonly obtained in the form of a wavelength- dependent reduced scattering coefficient $\mu_s'(\lambda)$, which alone is a function of the effective density of tissue scatterers (ρ_s) and effective reduced scattering cross-section, $\sigma'(\lambda, d_s)$.

DRS does not need exogenous contrast agents and can provide some unique features about biochemical composition, structure and morphology of biological tissues. However, each technique has its limitation when applied to clinical studies. For example, diffuse reflectance spectroscopy, only provides the optical properties of bulk tissue, but miss the biochemical composition details. In specific, DRS has been widely studied for differentiation of healthy tissues from diseased tissues due to its ability to give real time diagnosis in absence of the introduction of exogenous contrast agents, that cannot be obtained with conventional histopathological studies. The technique is easy manageable and straightforward in its application and can be implemented with comparatively inexpensive setup. The calculated diffuse reflectance spectra contain information concerning the absorption and scattering behaviors of tissues under experiment that can be used to achieve some unique features of biochemical composition, structure and morphology of biological tissues [25].

In order to discuss the DRS technique in more detail, it is crucial to recognize how light transports through biological tissues. When incident light travels through biological tissues, photon can be absorbed or scattered. A photon is absorbed if, after the interaction of one photon with the tissue, there is no re-emission of another photon, while scattering occurs if another photon is emitted after the connection, in an elastic or inelastic way.

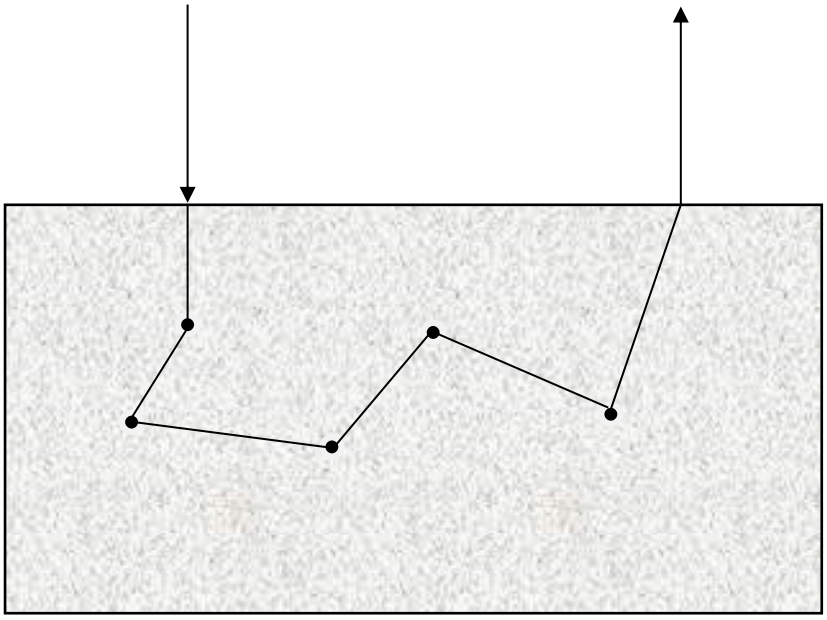

Fig.2.1. Interaction between light and tissue.

Numerous methods have been suggested to measure the optical parameters of rat liver tissue. These can be divided into two categories: direct and indirect. In the direct methods, optical properties are obtained using Lambert-Beer's law, whereas in indirect methods, a theoretical method of light scattering has to be built.

In past years, researchers have stated the values for total attenuation coefficient, the effective attenuation coefficient, the effective penetration depth, the absorption and the scattering coefficient, and the scattering anisotropy factor for different kinds of tissues at different wavelengths. Most of these results are established upon approximations to the radiative transport, like the diffusion theory [25].

2.2 Optical properties

2.2.1 Light Absorption

In DRS measurements, the reflectance signal gives information about the light absorption in the tissues. When light passes through a system of matter, the energy related with the incident field of light is most often abandoned as heat within the medium. If a chromophore or sphere of particular geometrical size obstructs incident light, it emits a shadow, which comprises absorption. Absorption is an entire transfer of energy from a photon to a molecule after which the photon ceases to survive. The absorption of spectral energy stimulates the molecules to a bigger state and remaining energy is lost over time. The depletion of energy predominantly occurs as heat dissipation, but can also produce in the discharge of a new photon, recognized as fluorescence or phosphorescence, or as photochemical responses [26].

In 1729, Bouguer [27] first found a correlation between the thickness of the medium and the absorption of light and later, in 1760, Lambert [28] extracted the mathematical statement for it, commonly studied as Lambert-Bouguer law or sometimes called the Lambert's law of absorption

$$I = I_0 e^{-\mu_a l} \tag{2.1}$$

Here I_0 is the incident light power, I is the transmitted light power through a distance l, and μ_a is the absorption coefficient which can be described as the possibility that a photon will be absorbed by the tissue per unit length.

In 1852 Beer demonstrated that the absorption coefficient of a tissue is linearly associated to its concentration, c weakened in a non-absorbing medium [29].

$$\mu_a = \alpha c \tag{2.2}$$

Where, α is the particular absorption coefficient. Substituting the value of μ_a in equation (2.2) gives the relation known as Lambert-Beer law:

$$I = I_0 e^{-\alpha c l} \tag{2.3}$$

which can be expressed as:

$$I = I_0 10^{-\varepsilon c l} \tag{2.4}$$

where, ε is the molar absorptivity of a specific compound in solution, known also as specific extinction coefficient.

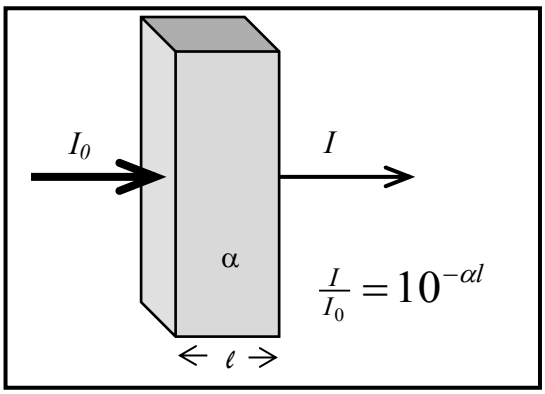

Fig.2.2. The Beer Lambert Law.

It is also possible to define absorbance, $A = \varepsilon c l$ as the absorbance associated to one particular compound, the total absorbance is the summation of the particular ones

$$A = A_1 + A_2 + \cdots + A_n = (\varepsilon_1 c_1 + \varepsilon_2 c_2 + \cdots + \varepsilon_n c_n) l \tag{2.5}$$

The Lambert-Beer law is valid only if the light which enters the medium is monochromatic and entirely collimated, and if the medium itself is pure and homogeneously absorbing.

The size of the absorption shadow is called the effective cross-section, σ_a (cm^2), that can be less or high than the geometrical size of the chromophore, A (cm^2), related by the proportionality constant known as absorption efficiency, Q_a (unitless):

$$\sigma_a(cm^2) = Q_a(-) \cdot A(cm^2) \tag{2.6}$$

The absorption coefficient, μ_a (cm^{-1}) is primarily the cross-sectional area per unit volume of medium ρ_a (cm^{-3}).

$$\mu_a(cm^{-1}) = \rho_a(cm^{-3}) \cdot \sigma_a(cm^2) \tag{2.7}$$

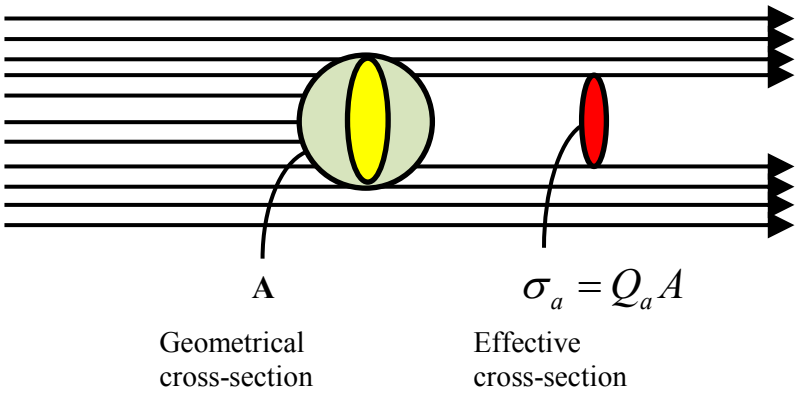

Fig.2.3. Absorption of light.

Experimentally, the units (cm^{-1}) of μ_a are inverse length, so that the product $\mu_a L$ is dimensionless, where L (cm) is the photon's path length of travel through the medium. The probability of survival or transmission, T of photon after a path length L, is

$$T = \exp(-\mu_a L) \tag{2.8}$$

2.2.2 Light scattering

Besides absorption, scattering is the other event that can occur to a photon which interacts with a sphere. Scattering is either an elastic or inelastic process where the photon experiences a change in direction. This usually happens when charged particles in a medium are set into oscillatory motion by the electric field of the incident wave and light is re-emitted (as opposed to absorbed) in a different direction of propagation in respect to the incident beam.

If a scattering particle or sphere with a particular geometrical redirects incident photons into new directions and so prevent the forward on-axis transmission of photons, thereby casting a shadow, scattering occurs.

The size of the scattering shadow is known as effective cross-section, σ_s(cm^2), and can be smaller or larger than the geometrical size of the scattering particle, A(cm^2), related by the proportionality constant called the scattering efficiency, Q_s (dimensionless):

$$\sigma_s(cm^2) = Q_s(-) \cdot A(cm^2) \tag{2.9}$$

The scattering coefficient, μ_s (cm^{-1}) describes a medium containing many scattering particles at a concentration described as volume density ρ_s (cm^3). The scattering coefficient is essentially the cross sectional-area per unit volume of medium.

$$\mu_s(cm^{-1}) = \rho_s(cm^{-3}) \cdot \sigma_s(cm^2) \tag{2.10}$$

Empirically, the units (cm^{-1}) of μ_s are inverse length, so that the result $\mu_s L$ is unitless, where L (cm) is the photon's path length of travel across the medium. The possibility of transmission, T of the photon without redirection by scattering after a path length L, is:

$$T = \exp(-\mu_s L) \tag{2.11}$$

As a consequence of scattering, the speed of light in biological tissue becomes smaller than its velocity in vacuo. In a medium where the molecular dissociation is lesser than the wavelength of the incident light, atoms and molecules will be scattered the primary beam in every directions. The total scattered field in any orientation is than a superimposition of all the scattered lights traveling in that orientation. It restricts with the incident light, altering its phase and the velocity of the wave across the medium [30]. The phase shift between the primary and the scattered light one depends on the frequency of the incident light. Scattering is relying on the size of the scatterer and the wavelength of the light; depending on this hypothesis scattering is categorized into three theoretical categories. If the geometric direction much bigger than the wavelength of the light then the direction of the scattered light can be studied by the distinctions in refractive index and Snell's law. The Mie theory

concerns to targets nearly of the same size as the wavelength which translated to tissue conditions corresponds to cellular structures and collagen fibers. Mie-direction is primarily due to the collagen fibers, but all types of scattering can be expected [31]. Mie-scattering is dependent on wavelength and strongly forward directed. The Rayleigh scattering is considered when the scatterers are much smaller than the wavelength of the light corresponding to cell membranes and cellular sub compartments. Rayleigh-scattering is mostly isotropic and it is oppositely proportional to the fourth power of the wavelength.

In analogy with the absorption coefficient, the scattering coefficient, $\mu_s(\lambda)$ [cm^{-1}], explain how long path a photon has to propagate in average before being scattered.

Explaining scattering as the number of scattering events per distance is not enough, but equitably essential in the direction of the photon after a scattering experience. The distribution of the scattering angles can be described by the scattering phase function, or the anisotropy factor, g, which explains the average of the cosine of the scattering angles, θ, illustrated as:

$$g = \langle \cos\theta \rangle \tag{2.12}$$

The anisotropy factor is usually used to explain the overall scattering in the tissue where values near to zero represents isotropic scattering, values near to 1 represents forward scattering, and a value of -1 represents backward scattering. For tissue the value of g can normally be noticed in the range of $0.74_{\lambda=476\ nm}$ to $0.995_{\lambda=665\ nm}$ [7]. These values show that tissue is primarily forward scattering in its characteristics and it can be assumed that most light remitted from the tissue has been multiply scattered.

For diffusely scattering tissue the reduced scattering coefficient, or transport scattering coefficient, $\mu_s'(\lambda)$ [cm^{-1}], is expressed as:

$$\mu_s'(\lambda) = \mu_s(\lambda) \cdot (1-g) \tag{2.13}$$

This expression has been introduced to decrease the effect of anisotropic scattering and obtain a more isotropic scattering for calculations of the photon path [1].

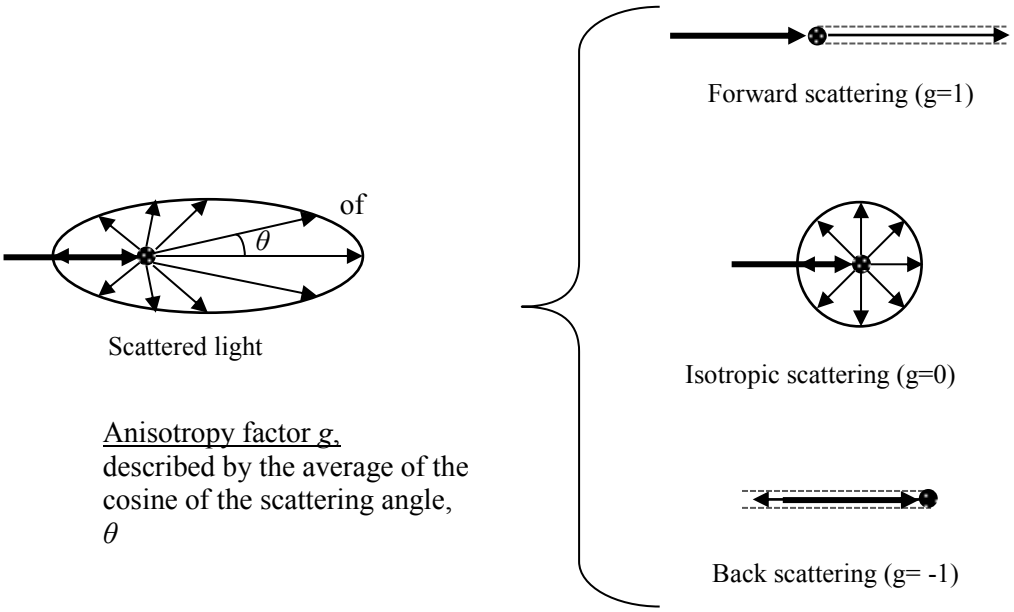

Fig. 2.4. Scattering of light by a single particle.

The refractive index, n, of homogenous matter of a substance is a dimensionless number that demonstrates how light, or any other radiation, travels through the medium. It is expressed as

$$n = \frac{c}{v} \tag{2.14}$$

in which c is the velocity of light in vacuo and v is the velocity of light in the studied medium.

Of note, the refractive index may display large variations at different wavelengths. Reflection and scattering in the biological tissue happens if there is a refractive index mismatch such as two different tissues, e.g. between blood cells and surrounding plasma or fluids. It is possible to distinguish scattering types depending on the size and the shape of the particles met by the incident wave: single and multiple scattering. Single scattering theory could be applied if the total scattered light is smaller than the incident light. This happens,

when the particles concentration in the medium is low enough to have a sufficiently large separation between the particles [30].

If the particle size is smaller than the wavelength of the incident light, Rayleigh scattering occurs (Rayleigh,1871) [32], which means that the intensity distribution of the scattered light is on average angularly isotropic (Fig. 2.5).

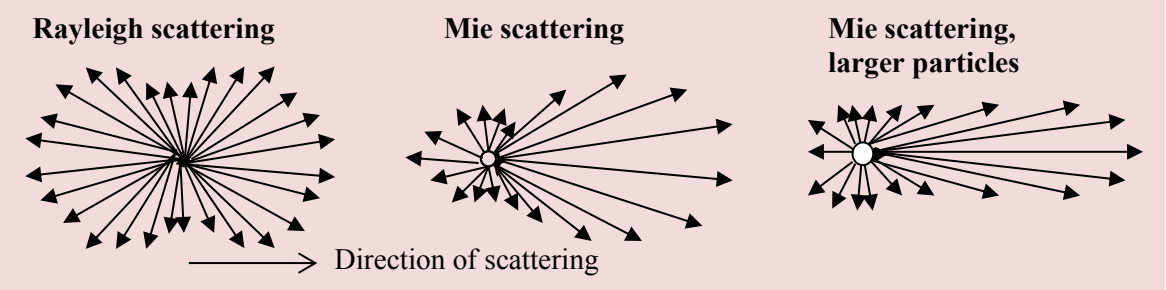

Fig.2.5. Influence of particle size on scattering.

Scattering of light by particles much smaller than the photon wavelength is called the Rayleigh limit of Mie scattering, or simply Rayleigh scattering. Besides, scattering of light by particles on the same size scale as the photon wavelength is explained by Mie theory [33].

Mie theory [33] further demonstrates both absorption and scattering by a spherical particle of arbitrary dimension and refractive index. The analysis comprises the formal solution of Maxwell's electromagnetic theory for homogenous particles applying suitable boundary conditions [30], which in case of small particles, reduces to the solution for a Rayleigh scatterer.

The exponential relationship expressed in equation (2.2) can be modified as

$$I = I_0 e^{-\mu_t l} \tag{2.15}$$

Where μ_t is the total interaction coefficient, explained by

$$\mu_t = \mu_a + \mu_s \tag{2.16}$$

and μ_s is the scattering coefficient, which expresses the possibility that a photon will be scattered per unit length. The inverse of the total scattering coefficient is known as free path.

Moreover, the new directions taken by photons after scattering do not appear with equal possibility and this anisotropic behavior can be explained by the differential scattering coefficient $d\mu_s(s,s')$, in which s and s' are respectively the directions of the incident and the scattered wave. The total scattering coefficient μ_s is calculated integrating it over all angles as follows:

$$\mu_s = \int_{4\Pi} d\mu_s(s,s')ds' \tag{2.17}$$

which depends on the angle between the incident and the scattered photons. In many media μ_s is not independent of s, but they have orientation-dependent structures for which waves with particular directions are scattered with higher probability than others, so that the scattering coefficient will therefore based on the incident direction.

Normalizing the differential coefficient, the scattering phase function is obtained

$$p(s,s') = \frac{1}{\mu_s} d\mu_s(s,s') \tag{2.18}$$

Defining that θ as the angle between s and s', it is possible to introduce the anisotropy factor g as its mean cosine

$$g = \int_{4\Pi} p(\theta)\cos(\theta)ds' \tag{2.19}$$

Linking the scattering coefficient and the anisotropy factor denotes the transport scattering coefficient

$$\mu_s' = (1-g)\mu_s \tag{2.20}$$

From which equation (2.15) can be modified as

$$\mu_t' = \mu_a + \mu_s \tag{2.21}$$

and to define $\mu_t'^{-1}$ as the transport mean free path.

In reality, for the majority of the systems in nature, it is not possible to assume that scatterers are independent of one another and multiple scattering has to be taken into consideration.The anisotropy factor, g (dimensionless), is an assumption of the amount of forward direction remained after a single scattering experience. Considering that a photon is scattered by a scatterer so that its direction is deflected by a deflection angle θ, (as depicted in figure 2.6). Then the component of the new direction which is coordinated in the forward direction is demonstrated in dashed line as cos (θ). On average, there will be an average deflection angle θ and the mean value of cos (θ) is known as the anisotropy factor.

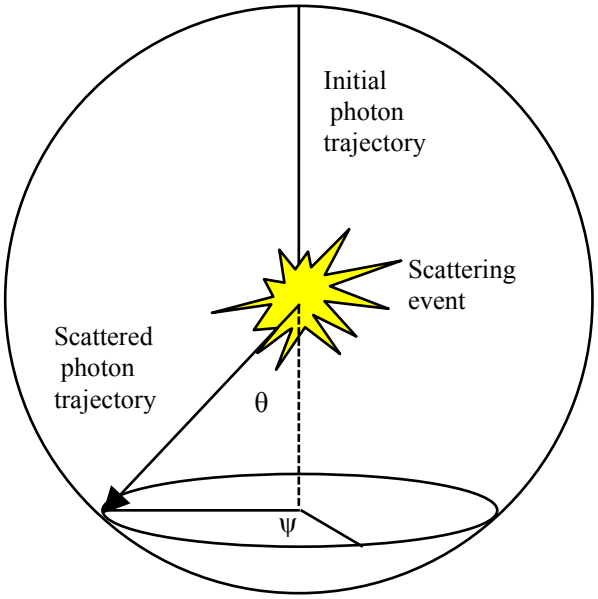

Fig. 2.6. Deflection of a photon by a scattering event. The angle of deflection, θ, and the azimuthal angle, ψ are indicated.

If a laser beam hits a target such a cylindrical cuvette having a dilute solution of scattering particles, the scattering phase function $p(\theta)$, can be determined by a detector that is moved in a circle around the target while always facing the target. Therefore, the detector receives light scattered at various deflection angle θ, in a horizontal expectation value for cos (θ):

$$g = \int_{4\pi} p\theta \cos\theta d\Omega = \int_{4\pi} p\theta \cos\theta \sin\theta d\theta d\phi < \cos\theta > \tag{2.22}$$

Where

$$d\Omega = \sin\theta d\theta d\phi \tag{2.23}$$

It is familiar to express the definition of anisotropy in a same way:

$$g = \int_{-1}^{1} p(\cos\theta)\cos\theta d(\cos\theta) \tag{2.24}$$

Where

$$\int_{-1}^{1} p(\cos\theta) d(\cos\theta) = 1 \tag{2.25}$$

2.2.3 Scattering Phase Function

The angular dependence of scattering is known as scattering phase function, $p(\theta)$ (sr^{-1}), which explains the possibility of photon scattering into a unit solid angle oriented at an angle θ, relative to the photons original trajectory. Of note, the scattering phase function depends only on the deflection angle θ, not on the azimuthal angle ψ. Such azimuthally symmetric scattering is special case, but is usually adopted when discussing scattering. However, it is also possible to consider scattering which does not exhibit azimuthal symmetry.

The simplest scattering phase function is the isotropic phase function:

$$p(\theta) = \frac{1}{4\pi} \tag{2.26}$$

The isotropic phase function would scatter light with equal efficiency into all positive directions. The Henyey-Greenstein scattering phase function [34] has proven to be advantageous in approximating the angular scattering dependence of single scattering events in biological tissues. The Henyey-Greenstein function allows the anisotropy factor g, to specify $p(\theta)$ such that calculation of the expectation value for cos (θ) returns exactly the same value of g.

The scattering phase function is given as

$$p(\theta) = \frac{1}{4\pi} \cdot \frac{1-g^2}{(1+g^2-2g\cos\theta)^{\frac{3}{2}}} \tag{2.27}$$

It is typical form to express the Henyey-Greenstein function as the function $p(\cos\theta)$;

$$p(\cos\theta) = \frac{1}{4\pi} \cdot \frac{1-g^2}{(1+g^2-2g\cos\theta)^{\frac{3}{2}}} \tag{2.28}$$

2.2.4 Light absorption in biological tissue

The main absorbers of visible/near-infrared light in biological tissues are oxy-hemoglobin, deoxy-hemoglobin, and water, with further absorption contributions, which sometimes can be of interest, from myoglobin, lipids, cytochrome oxidase, melanin, bilirubin, etc. Hemoglobin is a large group of hemoproteins responsible for the majority of the oxygen-carrying capacity in the body [35] and is thus perhaps the most important chromophore in the body. Hemoglobin and its various derivatives are the most dominant absorbers in the visible and near infrared wavelength range. Hemoglobin is carried in red blood cells, called erythrocytes, and constitutes approximately 40-45% of the whole blood. The chromophore is found in the erythrocytes and is therefore under normal circumstances bound to the lumen of the vascular network throughout the body. It is responsible for supplying oxygen from lungs to the body cells and returning waste products to the lungs to be eliminated. In the oxygenated state

hemoglobin is known as oxyhemoglobin (HbO_2), while in the de-oxygenated state it is known as de-oxyhemoglobin (Hb). The actual absorption spectra of the hemoglobin depend principally toward whether the blood is rich in oxygen or not and correspondingly remains in two main derivatives; oxyhemoglobin and deoxyhemoglobin.

The absorption spectra of oxy-hemoglobin (50 μM concentration) and deoxy-hemoglobin (50 μM concentration) in visible and near infrared wavelength range are shown in figure 2.7, which is derived from published data of absorption coefficients of hemoglobin [36]. Hemoglobin absorption coefficient reaches its maximum values at 445 nm and 560 nm. Extinction coefficient spectra of oxyhemoglobin represent the characteristic double maxima at around 576 and 542 nm as well as an absorption spike at 415 nm [37]. If no oxygen is combined to the hemoglobin molecule it is known as desaturated hemoglobin, or deoxyhemoglobin where the double maxima peaks of oxyhemoglobin is transformed into a single maxima at 555 nm, as well as there being red-shifting of the peak at 415 to 430 nm.

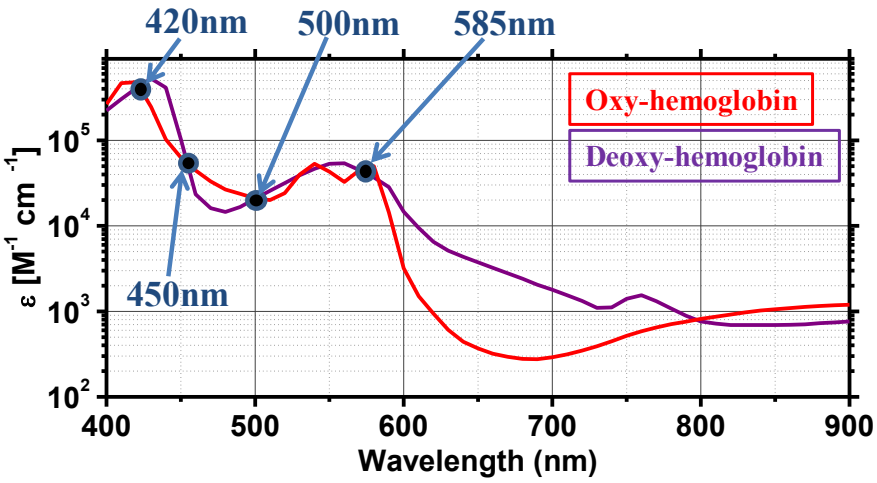

Fig.2.7. Absorption coefficient of oxyhemoglobin (HbO_2) and deoxyhemoglobin (Hb) at wavelength 400 to 900 nm.

There is also an additional absorption peak that turns apparent at 756 nm after reduction not found for oxyhemoglobin [37]. The concentration of hemoglobin for normal adults is near

about 120-180 g/L [38]. Another important parameter that has to be taken in consideration while measuring blood perfused biological tissues is the cytochrome oxidase. Cytochromes consist a wide and disparate group of hemoproteins responsible for the electron transport process. Cytochrome oxidase is the terminal enzyme in the mitochondrial respiratory electron transport chain that catalyzes the reduction of oxygen to water, directly connected with the energy production through oxidative phosphorylation [39]. Cells consume oxygen through the respiratory chain located in the inner membrane of mitochondria, which consist a sequence of interlinked, enzyme controlled reactions [40]. Of special interest is the complex of cytochrome aa_3, also termed as cytochrome c oxidase; which is responsible for the last steps of the oxygen transport chain coupled with cytochrome b and c [41]. Since cytochrome c oxidase carries four redox active metal centers (two heme and copper groups respectively) and those metal groups give rise to absorption bands in unltaviolet, visible, and near infrared regions. Near-infrared spectroscopy (NIRS) has utilized the unique absorption spectra of the oxidized and reduced state of cytochrome c oxidase with a view to resolve the physiological oxygenation status of tissue and organ *in vivo* [42]. Typically, the reduced cytochrome c oxidase has a strong and sharp absorption band whereas the oxidized heme has a broader and weaker absorption spectrum. These cytochromes are usually located in the inner mitochondrial membrane which separates the mitochondrial matrix from intermembrane space and the concentration is therefore normally time invariant, but oxidation and reduction alters the perceived absorbance [43] (shown in fig.2.8).

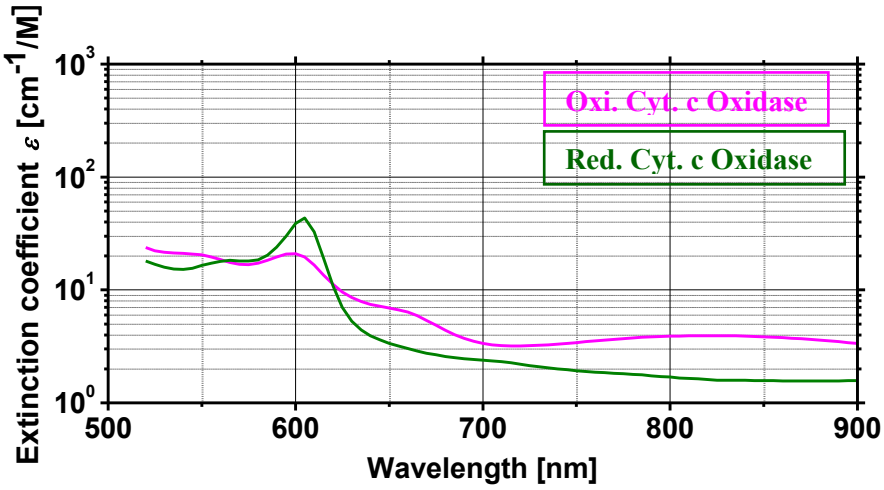

Fig.2.8. Absorption coefficient spectra of oxidized cytochrome c oxidase and reduced cytochrome c oxidase at wavelength 500 to 900 nm.

2.2.5 Light scattering in biological tissue

Biological tissues are mainly constituted by inhomogeneities which are responsible of mismatches in the relative refractive indices, causing an increase of the overall light scattering. Each microscopic particle, in a cellular or subcellular level, will generate its own phase scattering function and contribute in defining the averaged scattering properties of the tissue.

Figure 2.9 shows a generalized cell, in which the main components of cells are depicted. Cell sizes vary from 4 μm of blood platelets that reach to meter incase of nerve cell, but all of them are composed of same elements; the cell membrane, cytoplasm and the nucleus.

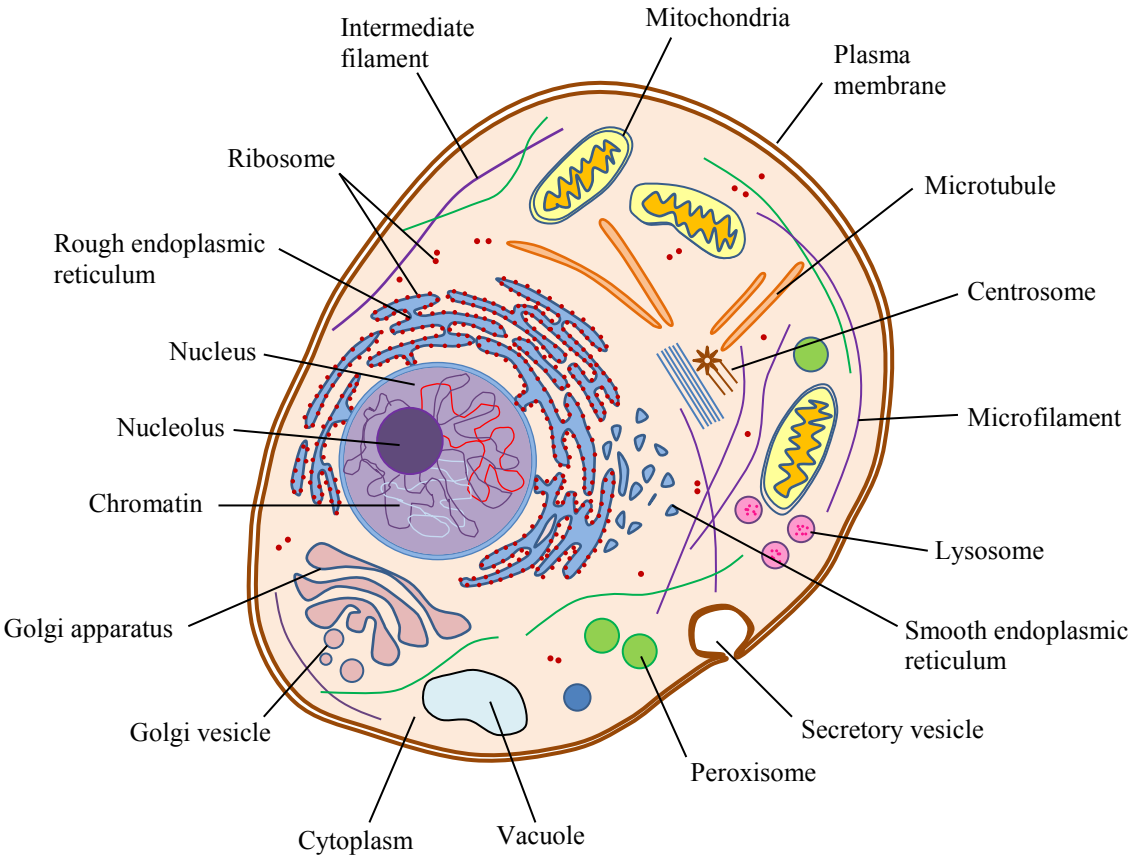

Fig.2.9. Structure of a typical cell.

The cell membrane surrounds the cell and it is made of phospholipids bilayer which is approximately 8 nm thick, with various proteins embedded in it, while the cytoplasm constitutes the intracellular matrix, the cytosol, in which the organelles are suspended. Among the organelles, mitochondria are responsible for energy supply to the cell and are approximately 0.3-0.5 μm to 1-4 μm in size and they have an outer boundary similar to the cell membrane. The largest organelle in the cytoplasm is nucleus, the control center of cell. The size varies with the cell type, with an average diameter of 5 μ, and is surrounded by a phospholipid bilayer [44]. As shown in fig. 2.10 the cell membrane is responsible of Rayleigh scattering, cytoplasm and nuclei cause Mie scattering.

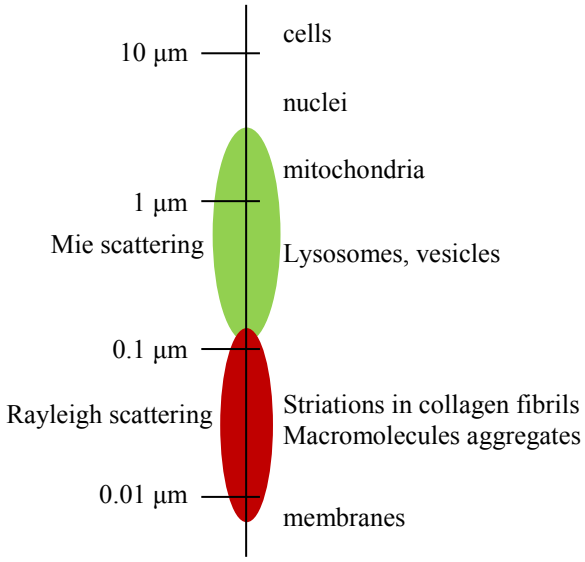

Fig.2.10. Ultrastructure of tissue.

The contribution of each type of particle to the mean scattering properties in tissue will be based on their individual properties and their relative contributions, but, studying bulk tissue, what is important are the total effects of scattering and absorption. The normal mean refractive index for tissue is in the range of 1.39-1.41, except of adipose tissue which is at 1.46 [45]. Most biological tissues have a large g value in the range of 0.7-0.97 [46], which indicate the forward-peaked scattering.

2.3 Multiple Regression Analysis

Multiple regression analysis is a powerful method used for predicting the unknown value of a variable from the known value of two or more variables-also called the predictors.

More precisely, multiple regression analysis aids us to predict the value of Y for the given values of $X_1, X_2, \ldots\ldots, X_k$.

In general, the multiple regression equation of Y on $X_1, X_2, \ldots.., X_k$ is given by:

$$Y = b_0 + b_1 X_1 + b_2 X_2 + \cdots\cdots\cdots\cdots b_k X_k \tag{2.29}$$

Here, b_0 is the intercept and $b_1, b_2, b_3, \ldots\ldots, b_k$ are the regression coefficients and are analogous to the slope in linear regression equation ($Y= a+bX$). They can be interpreted as, if $b_i = 2.5$, it would indicates that Y will increase by 2.5 units if X_i increased by one unit.

In the multiple regression analysis [47], a relationship between two variable sets y_k ($k= 1, 2, \ldots\ldots, p$) and x_{jk} ($j= 1,2, \ldots\ldots, q$) is assumed to be given by the following linear equation:

$$y_k = \alpha_0 + \sum_{j=1}^{q} \alpha_j \cdot x_{jk} + e_k \tag{2.30}$$

Where y_k represents response variable, x_{jk} denotes predictor variable, α_0 is a constant component, and e_k stands for unknown error components. In this multiple regression model, p represents the number of sample data being analyzed and q is that of predictor variables. The regression coefficients α_j ($j= 0,1,2,\ldots\ldots, q$) are unknown values that are estimated by the method of least squares in the analysis. When the estimated regression coefficients are expressed by $\hat{\alpha}_j$, then the corresponding multiple regression equation is expressed as,

$$\hat{y}_k = \hat{\alpha}_0 + \sum_{j=1}^{q} \hat{\alpha}_j \cdot x_{jk} \tag{2.31}$$

$$y_k = \hat{y}_k + r_k \tag{2.32}$$

Where, $\hat{y}_k$ is the estimated response variable using $\hat{\alpha}_j$, and r_k is the residual value. A measure for suitability of the regression equation is given by the parameter P^2, which can be defined as the square of the multiple correlation coefficient P, as

$$P^2 = \left[\frac{\sum_k (y_k - \bar{y}_k)(\hat{y}_k - \bar{\hat{y}}_k)}{\sqrt{\sum_k (y_k - \bar{y}_k)^2} \sqrt{\sum_k (\hat{y}_k - \bar{\hat{y}}_k)^2}} \right]^2 \tag{2.33}$$

Where $\bar{y}_k$ and $\bar{\hat{y}}_k$ denote the average of y_k and $\hat{y}_k$, respectively, over the p number of data. The value of P denotes the correlation coefficient between y_k and $\hat{y}_k$. The value of P^2 ranges from 0 to 1, and the linear approximation becomes better as P^2 approaches to 1.

2.4 Monte Carlo modeling of light transport

Monte Carlo simulations are a fundamental and versatile approach toward modeling of light transport in turbid tissues. This method simulates the "random walk" of photons in a medium that contains absorption and scattering properties. The two key components are, the mean free path length for a scattering or absorption event, and the scattering angle. Figure 2.5 demonstrates a scattering event. At boundaries, a photon is reflected or moves across the boundary. The rules of photon propagation are expressed as probability distributions for the incremental steps of photon movements, between sites of photon-tissue interaction, for the angle of deflection in a photon's trajectory when a scattering event occurs, and for the probability of transmittance or reflectance at boundaries. However, Monte Carlo method is essentially statistical in nature, and requires a computer to calculate the propagation of a large number of photons. The number of photons needed in a simulation depends greatly on the question being asked, the accuracy needed, and the spatial or temporal resolution desired. For example, to simply learn the total reflectance, R_t, from a tissue of specified optical properties, typically about 3,000 photons can produce a useful result. To map the spatial distribution of photons, $\phi(r,z)$, in a radially symmetric problem, at least 10,000 photons are generally needed to yields an acceptable answer. To map spatial distributions in a more complex three-dimensional situation such as a finite-diameter beam irradiating a tissue with a buried blood vessel, the required photons may exceed 100,000. The important point in this introductory remarks is that Monte Carlo simulations are rigorous, yet statistical and therefore require

significant computation time to acquire a specified precision and resolution. However, the flexibility of the method makes Monte Carlo simulation modeling a powerful tool.

The Monte Carlo simulations are based on macroscopic optical properties that are presumed to extend uniformly over small units of tissue volume. In this dissertation, the photons are treated as classical particles, polarization and wave phenomenon are neglected. Once photon which has the weight w launched in the tissue, it moved a step size s where it may be scattered, absorbed, internally reflected, or transmitted out of the medium. The photon is repeatedly propagated until it either escapes from or is absorbed completely in medium. This process is repeated until the desired number of photon has been propagated. The physical quantities such as the diffuse reflectance, total transmittance, and internal absorption are scored during the simulation. The algorithms of Monte Carlo simulation described here are mainly reported by Wang et al. [48] and Prahl et al. [49].

2.4.1 The coordinate system

The Monte Carlo simulation explained here describes with the propagation of an infinitely narrow photon beam perpendicularly incident on a simple or multi-layered tissue. The responses to the infinitely narrow photon beam are known impulse responses. Each layer is infinitely wide, and is represented by thickness t (cm), the refractive index n, the absorption coefficient μ_a (cm^{-1}), the scattering coefficient μ_s (cm^{-1}), and the anisotropy factor g. The refractive indices of the ambient medium above the tissue (e.g. air) and the ambient medium below the tissue (if existing) need to be considered as well. Although the real tissue can never be infinitely wide, it can be so considered on the condition that it is much wider than the spatial extent of the photon distribution. The tissue layers are parallel to each other. The absorption coefficient, μ_a is explained as the possibility of photon absorption per unit infinitesimal pathlength, and the scattering coefficient is explained as the possibility of photon scattering per unit infinitesimal pathlength. Whereas, the total interaction coefficient

μ_t, can be expressed as the summation of the absorption coefficient μ_a, and the scattering coefficient μ_s. Therefore, the interaction coefficient means the probability of photon interaction per unit infinitesimal pathlength. Three coordinate systems are employed in the Monte Carlo simulation at the same time. A Cartesian coordinate system [48, 49] (figure. 2.11) is applied to determine photon movements. The origin of the coordinate system is the photon incident point on the tissue surface; the z axis is the normal of the surface pointing facing the inside of the tissue; and the xy-plane is therefore on the tissue surface (fig.2.11). As the infinitely narrow photon beam is perpendicularly incident to the tissue surface of a multilayered tissue, the problem has cylindrical symmetry. Hence, a cylindrical coordinate system has been adopted to score internal photon absorption as a function of radial r and z, where r and z are the radial and z coordinates of the cylindrical coordinate system, correspondingly. The cylindrical coordinate system and Cartesian coordinate system share the origin and z-axis.

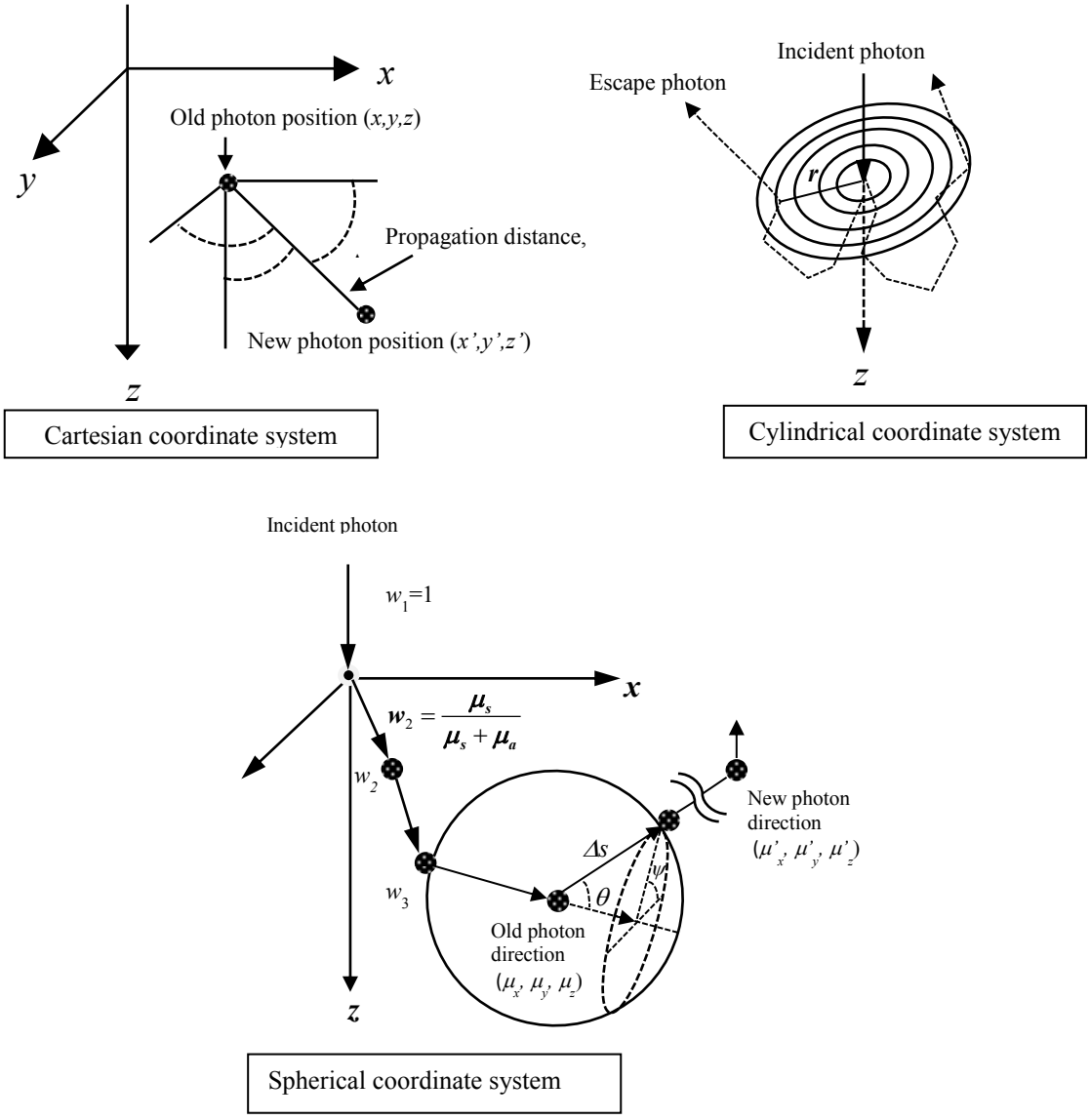

Fig.2.11. The three types of coordinate systems employed in the Monte Carlo simulation.

A moving spherical coordinate system, whose *z* axis is dynamically aligned with the photon propagation direction, is applied for sampling of the photon travel direction change of a photon packet. In this spherical coordinate system, the deflection angle,θ and the azimuthal angle, ψ due to scattering are initially sampled. Then, the photon direction is updated in terms of the directional cosines in the Cartesian coordinate system.

The *r* coordinate of the cylindrical coordinate system is also used for the diffuse reflectance and diffuse transmittance as a function of *r* and α, where α is the angle between the photon exiting direction and the normal to the tissue surface (-z axis for reflectance and z axis for transmittance).

2.4.2 Launching Photons

The Monte Carlo method starts by initiating a photon into the tissue. If a collimated beam normally incident on a slab is simulated, then the photon's initial trajectory is chosen downwards into the tissue. If a diffuse irradiance is simulated, then the photon's trajectory is chosen randomly from all possible directions in the downwards hemisphere. The coordinates of the photon are basically identical for all photons. The efficiency of a Monte Carlo program can be improved by propagating many photons (a packet) along each pathway. Usually only one photon follows each pathway, and at each step the photon may be either absorber or scattered. If a packet of photons followed each pathway then some portion of the packet would be absorbed at each step. The size of the packet is called the initial weight (*w*) of the photon. Photons initial weight is set to 1.0. The position of the photon is specified in Cartesian coordinates, (*x, y, z*), and all the propagation direction of a photon is described by the directional cosines (μ_x, μ_y, μ_z). The photon is injected orthogonally onto the tissue at the origin. The photon position (*x, y, z*) is initialized to (0, 0, 0) and directional cosines are set to (0, 0, 1).

When the photon is initiated, if there is a refractive-index inhomogeneity at boundary between the tissue and the ambient medium, then some specular reflection will result. If the refractive indices of the ambient medium and tissue are n_1 and n_2, respectively the specular reflectance, R_{sp}, is defined as,

$$R_{sp} = \frac{(n_1 - n_2)^2}{(n_1 + n_2)^2} \tag{2.34}$$

If the first layer is a transparent medium, which is on top of a layer of medium whose refractive index is n_3, multiple reflections and transmissions on the two boundaries of the transparent layer are considered. The specular reflectance is therefore determined by:

$$R_{sp} = r_1 + \frac{(1-r_1)^2 r_2}{1-r_1 r_2} \tag{2.35}$$

Where r_1 and r_2 are the Fresnel reflectances on the two boundaries of the transparent layer and expressed as:

$$r_1 = \frac{(n_1 - n_2)^2}{(n_1 + n_2)^2} \tag{2.36}$$

$$r_2 = \frac{(n_3 - n_2)^2}{(n_3 + n_2)^2} \tag{2.37}$$

The photon weight set to 1, is decreased by R_{sp} after the specular reflection, for the photon packet to enter the tissue as:

$$w = 1 - R_{sp} \tag{2.38}$$

2.4.3 Photon's stepsize

The simplest Monte Carlo method travels each photon with small and fixed incremental stepsizes. The fixed stepsize Δs must be smaller relative to the average mean free pathlength of a photon in the tissue. The mean free pathlength is the inverse of the total attenuation coefficient.

$$\Delta s << \frac{1}{\mu_t} = \frac{1}{\mu_s + \mu_a} \tag{2.39}$$

Where μ_t, μ_s and μ_a are the total attenuation, the scattering and the absorption coefficients respectively. If the photon stepsize is too small the photon will rarely interact with the tissue and the Monte Carlo method will be inefficient, besides if the stepsize is too large then the

distance travelled by a photon is a poor approximation to that of a real photon. A much more effective method takes a different stepsize for each photon step. The step size of the photon packet is determined depending on a sampling of the probability distribution for the photon's free path *s* ($0 \leq s < \infty$).

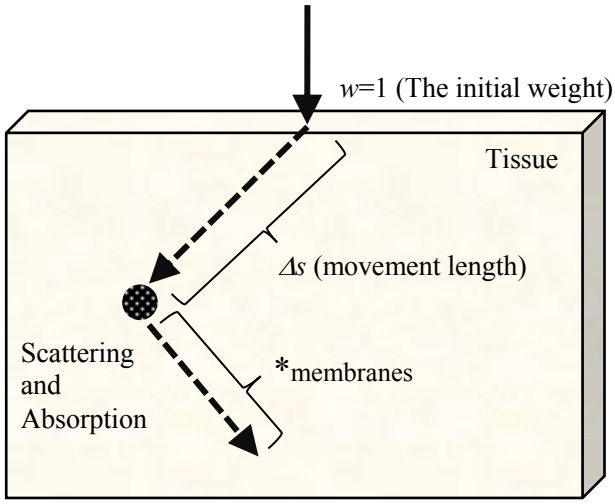

Fig.2.12. Step size of photon.

The step size Δs represents the distance between two successive interactions, or scattering in the tissue. The step size for each photon step Δs follows Beer's law, that is to say, it is more likely for a photon to travel a short distance than a long distance and the probability is proportional to $e^{-\mu_t \Delta s}$. A function of a random variable (ξ) uniformly distributed between 0 and 1, which yields a random variable with this distribution [48, 49] is:

$$\Delta s = \frac{-\ln \xi}{\mu_t} \tag{2.40}$$

The stepsize Δs found using equation (2.39) represents the distance that a photon will propagate before interacting (through absorption and scattering) with the tissue.

2.4.4 Photon moving

A photon is distinctively explained by five variables: three spatial coordinates for the position and two directional angles for the direction of travel. However it is convenient to explain the photon's spatial position with three Cartesian coordinates and the direction of travel with three directional cosines [50]. The direction cosines are described by taking the cosine of the angle that the photon's direction makes with each axis. These are specified by μ_x, μ_y and μ_z corresponding to each of the x, y and z-axes respectively. For a photon located at (x, y, z) traveling a distance Δs in the direction (μ_x, μ_y, μ_z), the new coordinates (x', y', z') are given by:

$$\begin{aligned} x' &\leftarrow x + \mu_x \Delta s \\ y' &\leftarrow y + \mu_y \Delta s \\ z' &\leftarrow z + \mu_z \Delta s \end{aligned} \tag{2.41}$$

2.4.5 Absorption of photon

After each propagation step, the photon packet is divided into two parts; a fraction is absorbed and the rest is scattered. The fraction of photon packet that is absorbed is

$$fractionabsorbed = \frac{\mu_a}{\mu_a + \mu_s} = 1 - \frac{\mu_s}{\mu_a + \mu_s} = 1 - a \tag{2.42}$$

Where a is the single particle albedo. Once the photon has arrived an interaction site, a part of the photon weight is absorbed by the interaction site and therefore the new photon weight (w') is explained by

$$w' = (\mu_a / \mu_t) w = aw \tag{2.43}$$

Which demonstrates the fraction of the packet that is scattered on this step.

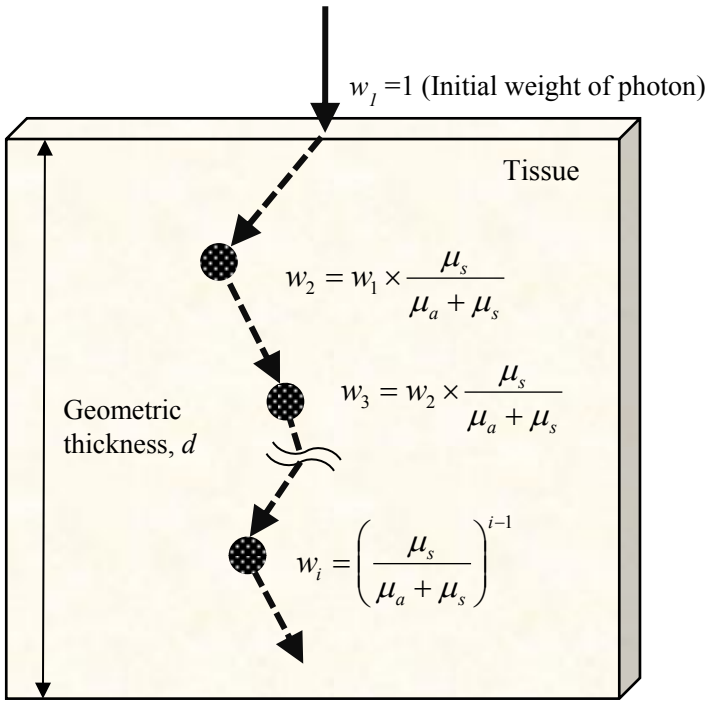

Fig.2.13. Change of photon weight.

An absorption experience requires that both the position and the amount of light absorbed be located. For example, the appropriate element of the absorption matrix is increased by (1- *a*)*w*. The number of bins in the absorption matrix is explained by the spatial resolution desired. Increasing the number of entries raises the spatial resolution, but also increases the absorption uncertainty in each element (because fewer absorption events will take place in each element and the error is reciprocal to the square root of the number of absorption events).The fluence rate is achieved by dividing the final value of each matrix element by (1) the equivalent spatial volume of the element, (2) the absorption coefficient, (3) the total number of photons traveled and (4) the initial weight of each photon.

2.4.6 Scattering of photon

A normalized phase function deals with the probability density function for the azimuthal and longitudinal angles for a photon when it is scattered. Once the photon packet reached an interaction site, and its weight decreased, the photon with new weight is ready to be scattered.

There will be a deflection angle, θ ($0 \leq \theta < \pi$), and an azimuthal angle, ψ ($0 \leq \psi < 2\pi$), to be sampled statistically.

If the phase function has no azimuthal dependence, then the azimuthal angle ψ is evenly distributed between 0 and 2π, and may be generated by multiplying a pseudo-random number ξ evenly distributed over the interval zero to one by 2π as

$$\psi = 2\pi\xi \tag{2.44}$$

The probability distribution for the cosine of the deflection angle, cos θ, is defined by the scattering phase function that Henyey and Greenstein [34] originally introduced for scattering as:

$$p(\cos\theta) = \frac{1-g^2}{2(1+g^2-2g\cos\theta)^{\frac{2}{3}}} \tag{2.45}$$

Here the anisotropy factor, g, equals <cosθ> with a value between -1 and 1.

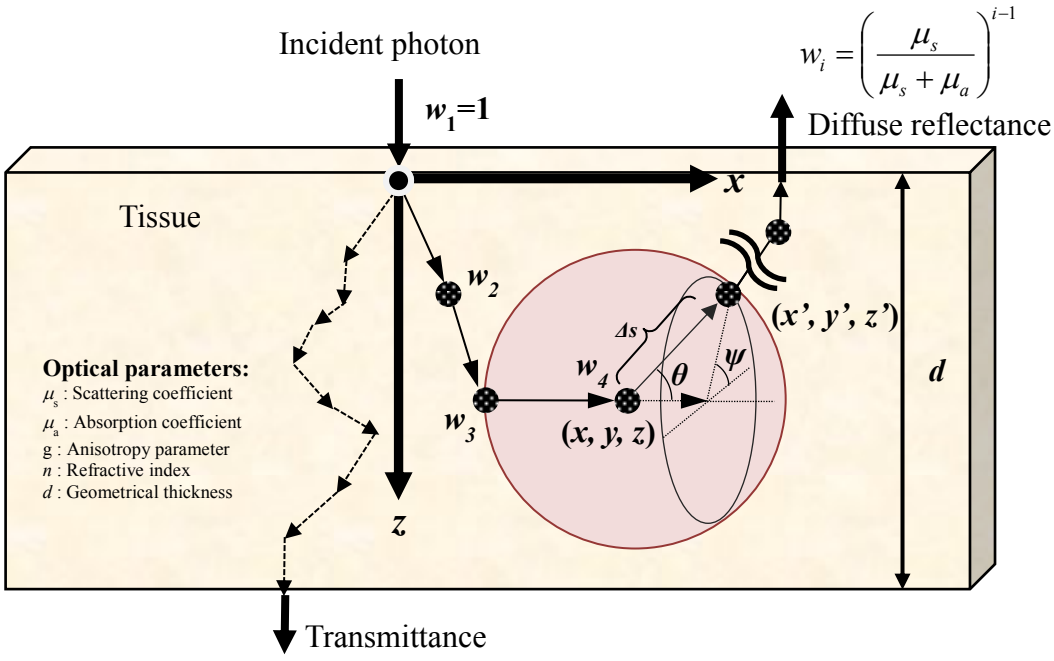

Fig. 2.14. Scattering of photon.

A value of 0 suggests isotropic scattering and a value near of 1 suggests forward-directed scattering. Value of g with a range between 0.3 and 0.98 for tissues, but most often g is ~ 0.9 in the visible spectrum.

The choice for deflection angle, cos θ can be defined as a function of the random number, ξ as:

$$p(\cos\theta) = \frac{1}{2g}\left\{1+g^2-\left[\frac{1-g^2}{1-g+2g\xi}\right]^2\right\}, \text{ if } g\neq 0 \tag{2.46}$$

The deflection angle, θ for an isotropic distribution is expressed as

$$\cos\theta = 2\xi - 1, \text{ if } g=0 \tag{2.47}$$

If a photon is scattered at an angle (θ, ψ) from the direction (μ_x, μ_y, μ_z) in which it is propagating, then the new direction (μ'_x, μ'_y, μ'_z) is described [48, 49] by

$$\begin{aligned}
\mu'_x &= \frac{\sin\theta}{\sqrt{1-\mu_z^2}}(\mu_x\,\mu_z\cos\psi - \mu_y\sin\psi) + \mu_x\cos\theta \\
\mu'_y &= \frac{\sin\theta}{\sqrt{1-\mu_z^2}}(\mu_y\,\mu_z\cos\psi - \mu_x\sin\psi) + \mu_y\cos\theta \\
\mu'_z &= -\sin\theta\cos\psi\sqrt{1-\mu_z^2} + \mu_z\cos\theta
\end{aligned} \tag{2.48}$$

If the photon propagation direction is sufficiently close to the z-axis (e.g. $|\mu_z| > 0.99999$), then the following formulas should be used:

$$\begin{aligned}
\mu'_x &= \sin\theta\cos\psi \\
\mu'_y &= \sin\theta\sin\psi \\
\mu'_z &= \frac{\mu_z}{|\mu_z|}\cos\psi
\end{aligned} \tag{2.49}$$

to obtain the new photon directions.

2.4.7 Internal reflection of photon

During a step, the photon packet may strike a boundary of the tissue, which is between the tissue and the ambient medium. The internal reflection may occur when the photon is propagated across a boundary into an area with a different index of refraction. The internal reflectance, $R(\alpha_i)$, is calculated by Fresnel's formulas, [51, 52]

$$R(\alpha_i) = \frac{1}{2}\left[\frac{\sin^2(\alpha_i - \alpha_t)}{\sin^2(\alpha_i + \alpha_t)} + \frac{\tan^2(\alpha_i - \alpha_t)}{\tan^2(\alpha_i + \alpha_t)}\right] \tag{2.50}$$

which is an average of the reflectances for the two orthogonal polarization directions.

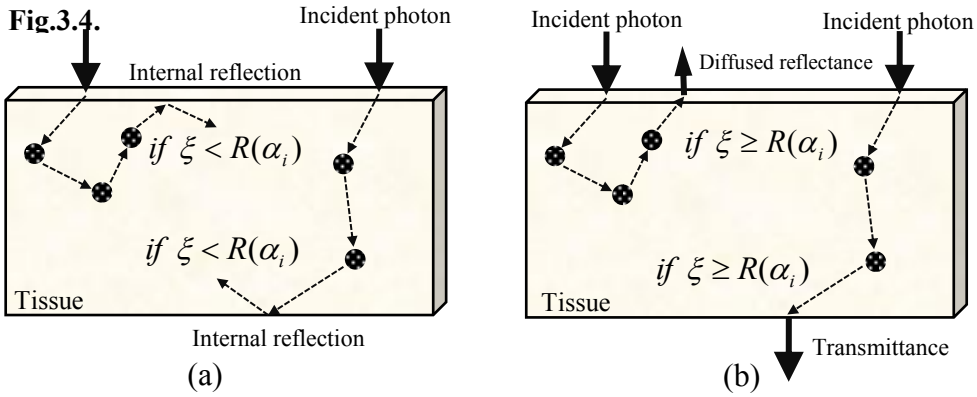

Fig.2.15(a) Internal reflection **Fig.2.15(b)** Diffuse reflectance and transmittance

The probability of a photon packet being internally reflected based on the angle of incidence, α_i, onto the boundary, where α_i =0 means orthogonal incidence. The value of α_i is calculated:

$$\alpha_i = \cos^{-1}\mu_z \tag{2.51}$$

Snell's law demonstrates the relationship between the angle of incidence, α_i, the angle of transmission, α_t, and the refractive indices of the tissue that the photon is incident from n_i, and transmitted to, n_t:

$$n_i \sin\alpha_i = n_t \sin\alpha_t \tag{2.52}$$

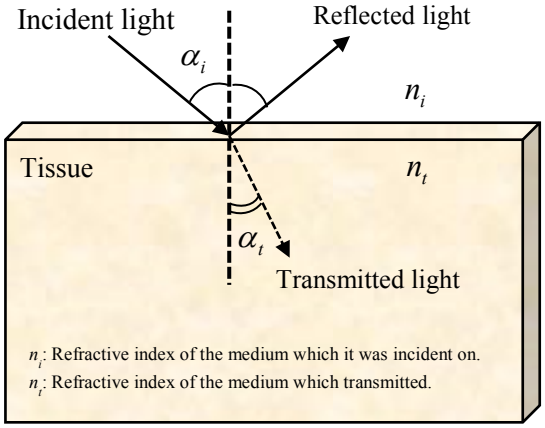

Fig.2.16. Photon incident and transmittance angle.

A random number, ξ, evenly distributed between 0 to 1 is used to explain whether the photon is internally reflected or transmitted, that is:

If $\xi \leq R(\alpha_i)$, then photon is internally reflected; (2.53)

If $\xi > R(\alpha_i)$, then photon escapes the tissue or transmits. (2.54)

If the photon is internally reflected, then the photon packet remains on the surface and its directional cosines (μ_x, μ_y, μ_z) must be updated by reversing the z component:

$$(\mu_x, \mu_y, \mu_z) \leftarrow (\mu_x, \mu_y, -\mu_z) \tag{2.55}$$

If the photon transmits through the boundary, it is determined whether the photon has entered another layer of tissue or ambient medium. If the photon transmitted another layer of tissue, it continues to propagate with an updated direction and step size. The new directional cosines are given as

$$\begin{aligned} \mu_x' &= \sin\alpha_t \mu_x / \sin\alpha_i \\ \mu_y' &= \sin\alpha_t \mu_y / \sin\alpha_i \\ \mu_z' &= \frac{\mu_z}{|\mu_z|}\cos\alpha_t \end{aligned} \tag{2.56}$$

or employing Snell's law, the above equation can be rewritten as:

$$\begin{aligned} \mu_x' &= \mu_x \cdot n_i / n_t \\ \mu_y' &= \mu_y \cdot n_i / n_t \\ \mu_z' &= \frac{\mu_z}{|\mu_z|} \cos \alpha_t \end{aligned} \tag{2.57}$$

2.4.8 Photon termination

The photon will continue to propagate as its weight becomes gradually smaller. A technique called the "Russian Roulette" is applied to terminate the photon when $W \leq W$th. A threshold value is determined, typically 10^{-4}. When the photon's weight decreases below this threshold value, the roulette procedure is applied. For a photon packet that is still propagating inside the tissue, if the photon weight, W, has been significantly decreased after many steps of interaction such that it falls below a threshold value, then further movement of the photon results little information unless the very late stage of the photon movement. However, proper termination must be executed to ensure conservation of energy (or number of photons) without skewing the distribution of photon deposition.

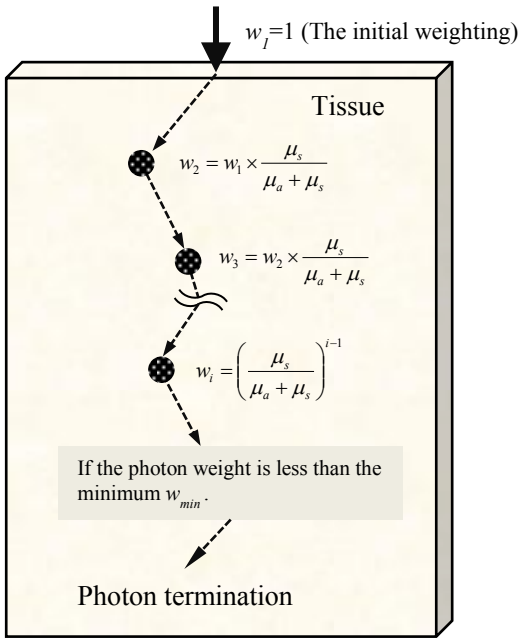

Fig.2.17. Termination of photon.

The roulette technique provides such a photon (with weight W) one chance in m (e.g., 10) of surviving with a weight of mW or else its weight is decreased to zero. If the photon packet does not survive the roulette, the photon weight is decreased to zero and the photon is terminated. Once the photon is terminated, a new photon can be launched.

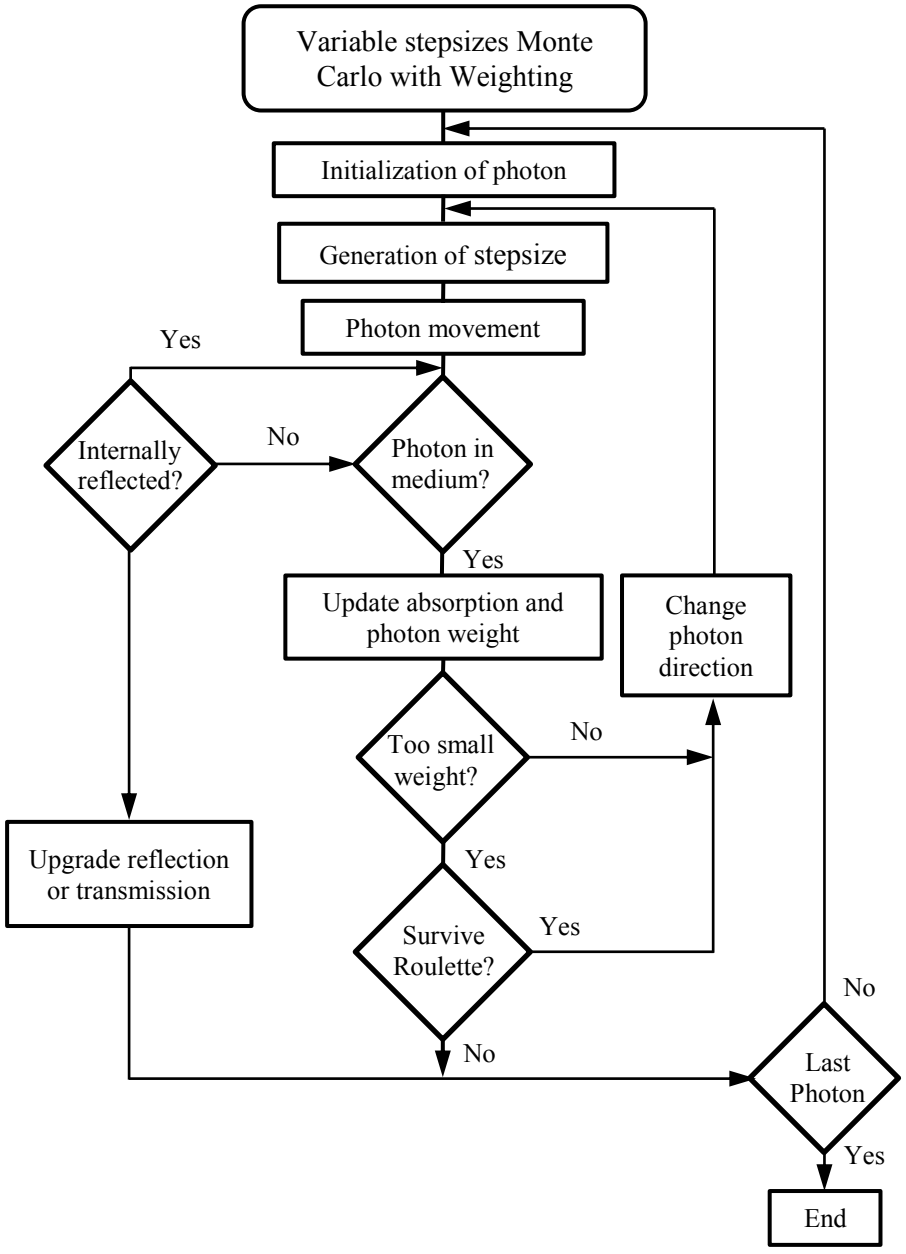

Fig.2.18. Flowchart for the variable stepsize Monte Carlo technique.

2.4.9 Calculating Physical Quantities

The process of two physical quantities; reflectance R and transmittance T are discussed in this section. If the photon leaves the tissue into the ambient medium, the photon weight is scored into diffuse reflectance or transmittance. If the photon has not been scattered, the photon weight is scored into unscattered reflectance or transmittance based on where the photon escapes. If the photon has been scattered at least one time, the diffuse reflectance, $R(r, \alpha_t)$, or diffuse transmittance, $T(r, \alpha_t)$, at particular grid element (r, α_t) is incremented by the amount of escapes photon weight, w:

$$R(r,\alpha_t) \leftarrow R(r,\alpha_t) + w \text{ , if } z=0 \tag{2.58}$$

$$T(r,\alpha_t) \leftarrow T(r,\alpha_t) + w \text{ , if } z= \text{ the bottom of the tissue} \tag{2.59}$$

Because the photon has completely escaped, the tracing of this photon terminates here. A new photon may be initiated into the tissue and propagated thereafter. After tracing multiple photons, the total diffuse reflectance R and transmittance T are calculated from the array of $R(r, \alpha_t)$ and $T(r, \alpha_t)$. They are explained by $R_{d\text{-}r\alpha}[i_r, i_\alpha]$ and $T_{t\text{-}r\alpha}[i_r, i_\alpha]$ respectively. The coordinates of the center of a grid element are calculated by:

$$r = (i_r + 0.5).\Delta r \text{ [cm]}, \tag{2.60}$$

$$\alpha = (i_\alpha + 0.5).\Delta\alpha \text{ [rad]} \tag{2.61}$$

where i_r and i_d are the indices for r and α, respectively. The raw data provide the total photon weight in each grid element in the two-dimensional grid element. To obtain the total photon weight in the grid elements in each direction of the two-dimensional grid system, the 2D arrays are summed in the other dimension:

$$R_r[i_r] = \sum_{i_\alpha=0}^{N_\alpha-1} R_{r\alpha}[i_r, i_\alpha] \tag{2.62}$$

$$R_\alpha[i_\alpha] = \sum_{i_r=0}^{N_r-1} R_{r\alpha}[i_r, i_\alpha] \tag{2.63}$$

$$T_r[i_r] = \sum_{i_\alpha=0}^{N_\alpha-1} T_{r\alpha}[i_r, i_\alpha] \tag{2.64}$$

$$T_\alpha[i_\alpha] = \sum_{i_r=0}^{N_r-1} T_{r\alpha}[i_r, i_\alpha] \tag{2.65}$$

To obtain the raw data of total diffuse reflectance and transmittance, the 1D array are summed again:

$$R = \sum_{i_r=0}^{N_r-1} R_r[i_r] \tag{2.66}$$

$$T = \sum_{i_r=0}^{N_r-1} T_r[i_r] \tag{2.67}$$

Finally the total diffuse reflectance and transmittance are obtained by dividing the raw total diffuse reflectance and transmittance by the total number of photons as

$$R \leftarrow R / N \ \text{[-]} \tag{2.68}$$

$$T \leftarrow T / N \ \text{[-]} \tag{2.69}$$

Where [-] indicates dimensionless unit.

2.7.10 Inverse Monte Carlo Method

The Monte Carlo simulation is basically used for simulation of measurable physical quantities such as reflectance, transmittance, and internal absorption applying given parameters. Besides, the inverse Monte Carlo method helps to estimate the absorption coefficient μ_a, scattering coefficient μ_s, and anisotropy factor g, from the measured reflectance, transmittance, and/or collimated transmittance. In the inverse Monte Carlo

method, to determine the unknown optical parameters from measurable macroscopic values, the Monte Carlo simulation is inverted. At first, the Monte Carlo simulation take the set of initial values for the optical parameters μ_a, μ_s and/ or g calculates the reflectance, transmittance, and/or collimated transmittance. Then, the calculated quantities are compared with the measured quantities. If there is significance deviations, the optical parameters are varied slightly, and the new forward simulation are performed. This process is repeated until the deviation between measured and calculated values is within the predetermined threshold.

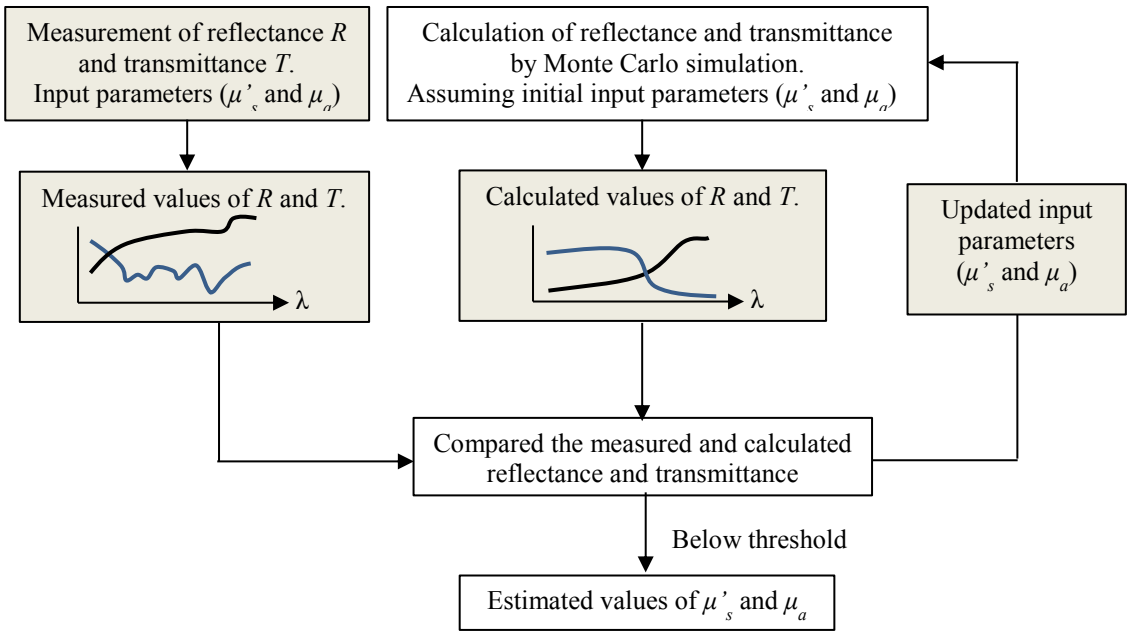

Fig.2.19. Inverse Monte Carlo simulation.

2.5 Spectrocolorimetry

The color of an object is often measured objectively with a spectrocolorimeter which measures the object and converts the color to tristimulus values as a numerical representation of human vision. The actual tristimulus values, usually measured by using three separate filters, are provided by CIE standard observer. Spectrocolorimetry [53, 54] is a method used

for calculating the colorimetric value from the measured spectral power, reflectance, or transmittance. The most popular color system is the CIEXYZ color system [53, 54], recommended by Commission Internationale de l'Eclairage (International Commission on Illumination), CIE founded in 1913. CIE considered the tristimulus values, X, Y, and Z for called R (red), G (green), and B (blue), to create a standardized color model. CIE X, Y, Z tristimulus values are calculated as follows:

$$X = k\sum E(\lambda)\cdot\bar{x}(\lambda)\cdot O(\lambda) \tag{2.70}$$

$$Y = k\sum E(\lambda)\cdot\bar{y}(\lambda)\cdot O(\lambda) \tag{2.71}$$

$$Z = k\sum E(\lambda)\cdot\bar{z}(\lambda)\cdot O(\lambda) \tag{2.72}$$

Where E(λ) and O(λ) denote the spectral distribution of illuminant, and the diffuse reflectance spectrum of object, correspondingly and $\bar{x}(\lambda)$, $\bar{y}(\lambda)$, and $\bar{z}(\lambda)$ are the color matching functions in the CIEXYZ color system. The value of constant k which results in Y being equal to 100 for the perfect diffuser is given by

$$k = 100/\sum E(\lambda)\cdot\bar{y}(\lambda) \tag{2.73}$$

In Eqs. (1.1)-(1.4), the summation can be carried out using data at 20 nm intervals, from 400 to 700 nm. For the most applications, it is needed to take values at every 10 nm or 5 nm, with a wavelength range from 380 to 780 nm.

The color sensitivity of human eye changes according to the angle of view (object size). The CIE originally proposed the standard observer in 1931 using a 2º field of view, therefore the name 2º Standard Observer. If the size of field of view is reduced, the ability to discriminate one color from another becomes less marked. Therefore, 2º matches tend to break down. In 1964, the CIE proposed an additional standard observer, based upon a 10º field of view; which is known as the 10º Supplementary Standard Observer. The 2º Standard Observer is

applied for viewing angles of 1º to 4º; the 10º Supplementary Standard Observer is applied for viewing angles of more than 4º.

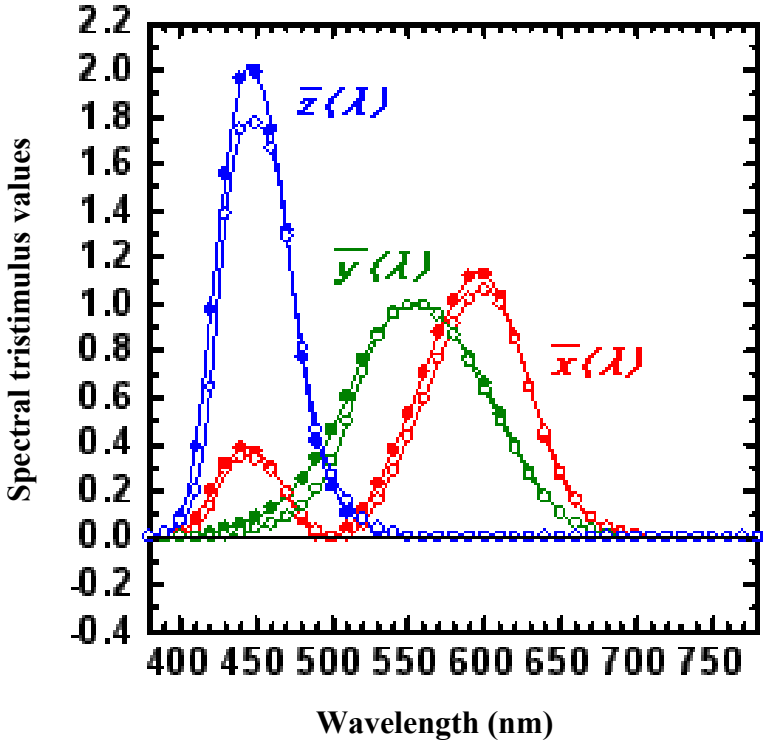

Fig.2.20. CIE Color matching.

The chromaticity coordinates are used in together with a chromaticity diagram: the most familiar one being CIE's 1931 *xyY* chromaticity diagram:

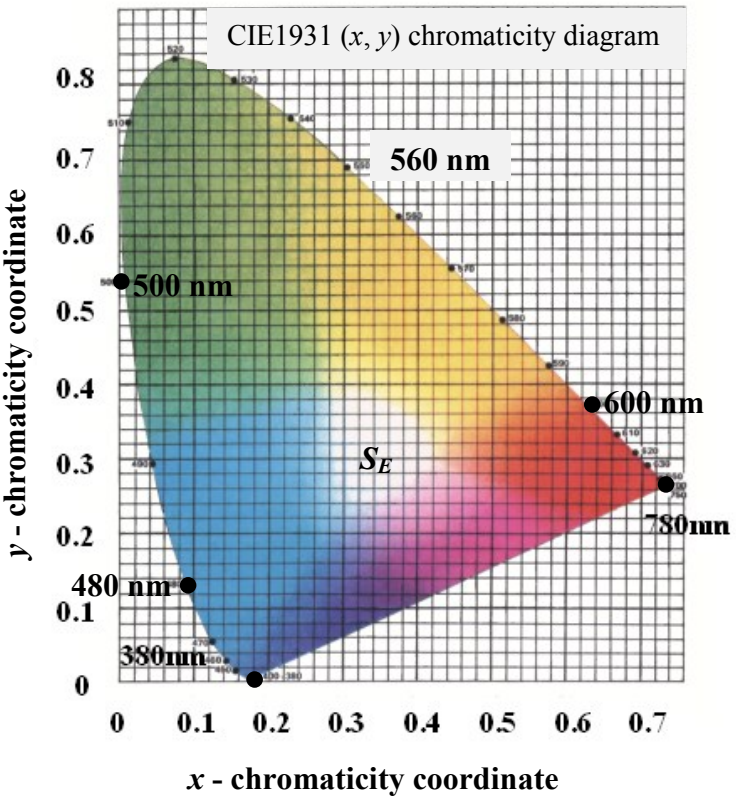

Fig.2.21. CIE1931 (*x*, *y*) chromaticity diagram. Monochromatic colors are located on the perimeter and white light is located in the center of the diagram.

The horseshoe-shaped color space is set in a grid adopting the chromaticity coordinates *x* and *y* as a locator for any value of hue and chroma. These correspond to the color itself (e.g., reddish-orange) and the fullness of the color or saturation. The coordinate *z* is not applied, but can be inferred from the other two as the sum of the coordinates x+*y*+*z* is always 1. The white spot in the following figure (Fig.2.22) represents the location of the illuminant. The third dimension is represented by the tristimulus value *Y*.

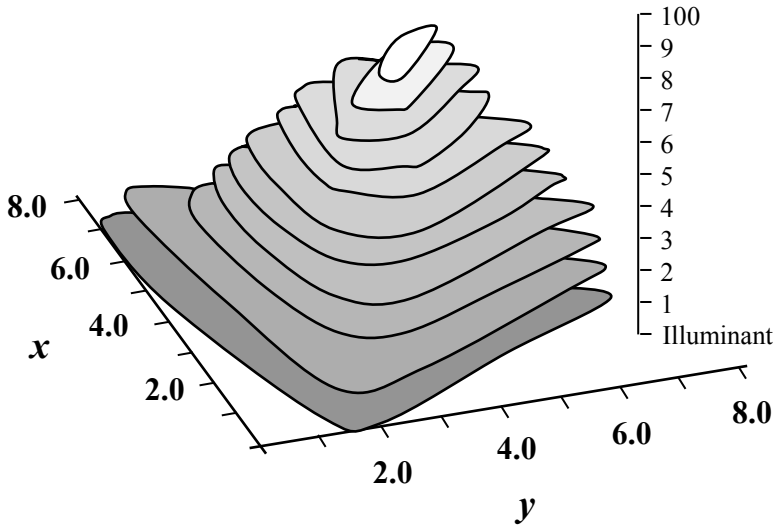

Fig.2.22. CIE *xyY* chromaticity diagram.

This value represents the lightness or luminance of the color. The scale for *Y* enlarges from the white spot in a line perpendicular to the plane formed by x and y applying a scale that runs from 0 to 100. The fullest range of color exists at 0 where the white point is equivalent to CIE Illuminant C. The values then range from 100 for white, or transparent objects, that absorb no light, to zero for objects that absorb all the light. As the *Y* value rises and the color becomes lighter, the range of color, or gamut, decreases so that the color space at 100 is just a sliver of the original area.

It is often useful to use the ratio Y/Y_n, where Y_n is the value of *Y* for a appropriate chosen reference white or reference transparent specimen. If the reference object absorbs some light, as is usually the case, Y/Y_n will be slightly more than 1 for the perfect diffuser. The important color attributes are correlated with the relative magnitudes of the tristimulus values. Therefore, it is useful to calculate a type of relative tristimulus values known as chromaticity coordinates, as follows:

$$x = X/(X+Y+Z) \tag{2.74}$$

$$y = Y/(X+Y+Z) \tag{2.75}$$

$$z = Z/(X+Y+Z) \tag{2.76}$$

The chromaticity coordinates represent the relative amounts of the tristimulus values. It is clear from the way in which, x, y, and z are calculated that $x + y + z = 1$, and thus, if x and y are known, z can be calculated from 1- x - y. With only two variables, such as x and y, it becomes possible to reconstruct two-dimensional diagram, so called the x-y chromaticity diagram, which is shown in fig. 2.21. This diagram gives a sort color map, on which the chromaticities of all colors can be plotted.

The equi-energy stimulus, S_E, has tristimulus values that are equivalent to one another, and its chromaticity coordinate are $x = 1/3$, $y = 1/3$, and $z = 1/3$. It is plotted at this position in Fig. 2.21. The curve line in the diagram displays where the colors of the spectrum lie and is known as the spectral locus. The wavelengths are explained in nanometers along the curve. If two color stimuli are additively mixed together, then the point demonstrating the mixture is located in the diagram by a point that always lies on the line joining the two points demonstrating the two original colors. This means that if the two ends of the the spectrum are linked by a straight line, which line represents mixture of light from the two ends of the spectrum.

As these colors are mixture of red and blue, the resulting line is known as purple boundary. The area enclosed by spectral locus comprises of a continuously convex boundary so that all mixtures of wavelengths must lie inside it.

If the points are considered between the point representing S_E and light of particular wavelength considered. If the mixture comprises mainly the spectral color, then the corresponding point will lie near the spectral locus and will tend to demonstrate a saturated color of that particular hue. On the other hand, if the mixture comprises mainly of S_E, then the

corresponding point will lie near S_E and will tend to indicate a pale color of that hue. Therefore, the chromaticity diagram represents a continuous gradation of stimuli from those like S_E to those like spectral colors, in the space between S_E and the spectral locus.

It is crucial to remember that chromaticity diagram only shows the ratios of the tristimulus values. Therefore, bright or dim lights, or brighter or dimly lit surface colors, or light and dark surface colors, having the same ratios to another, all plot at the same time. That is why, the point S_E, for instance, demonstrates all levels of the equi-energy stimulus. If this stimulus is considered as an illuminant, the same point also demonstrates whites, grays, and blacks irradiated by it any level. It is also essential to note that the chromaticity diagram is a map of relationship between the color stimuli, not between the color perceptions, will rely on the viewing situations and on the adaptation and other characteristics of the observer.

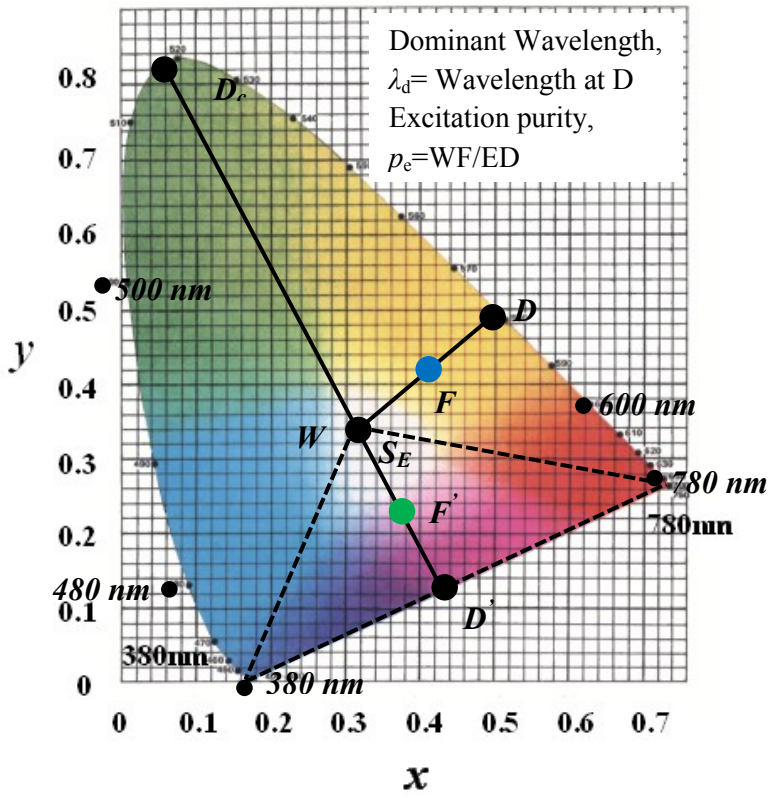

Fig.2.23. The derivation of *x-y* diagram of dominant wavelength, λ_d, complementary wavelength, λ_c, and excitation purity, p_e, equal to WF/WD or *WF'/WD'*.

The chromaticity diagram can be applied to give calculations that correlate approximately with the perceptual color attributes, hue and saturation. In fig.2.23 the point *F* demonstrates a color being considered. The point *W* demonstrates a suitably chosen reference white (or gray), the achromatic stimulus, which is almost always different from the equi-energy stimulus S_E. For the reflecting surface colors, it is common practice to take in account the perfect diffuser, irradiated by the light source in use, to be reference white. Then, a line is drawn from *W* through *F*, to meet the spectral locus at a point *D*. The wavelength on the spectral locus corresponding to *D*, is known as the dominant wavelength λ_d, of the color *F*, compare to the white point *W*. It is clear from the diagram that the color *F* can be considered of as a color that can be matched by an additive mixture of the color *D* and the white *W*. In this sense, the predominant wavelength is very descriptive name for this measure. For a color *F*', if the point *D* is on the purple boundary, *WF*' is extended in the opposite direction to meet the spectral locus at a point D', which explains the complementary wavelength λ_c. The dominant (complementary) wavelength may be considered to be approximately associated with the hue of colors. The ratio of the length of the lines WF and WD (or WF' and WD') gives a calculation known as excitation purity p_e as

$$p_e = \text{WF/WD or WF'/WD'} \tag{2.81}$$

If p_e is nearly unity, the point is near the spectral locus or purple boundary, and will tend to demonstrate a color that is greatly saturated. On the other hand, if p_e is close to zero, the point is close to the reference white, and will tend to demonstrate a color that is very pale. Excitation purity may be treated to be approximately associated with the saturation of colors. Although the *x-y* chromaticity diagram has been extensively used, it suffers from a disadvantage: such as the distribution of the colors on it is very non-uniform. The CIE has recommended the use of the uniform chromaticity diagram, which is known as the CIE 1976 uniform chromaticity scale diagram [53, 54], to lessen the effect of non-uniformity.

Chapter 3

Evaluation of light scattering and absorption properties of *in vivo* rat liver using a single-reflectance-fiber probe during pre-ischemia, ischemia-reperfusion, and postmortem

3.1 Introduction

Hepatic ischemia-reperfusion includes a complex series of phenomena that may results in hepatocellular injury. Hepatic ischemia-reperfusion is a common sequel of liver surgery, especially after liver resection and liver transplantation, complicated by microcirculatory hepatic failure, accompanied with necrosis and cell death [55]. Occlusion of hepatic circulation (Pringle maneuver) by hepatic portal vein occluding was primarily devised to lessen intraoperative blood loss during emergency liver transplantation [20]. The serious side effect of partial liver resection is the ischemia in the remnant liver following transient vascular occlusion [56]. The liver carries multiple number of chromophores (oxygenated hemoglobin (HbO), deoxygenated hemoglobin (HbR), cytochrome c oxidase (CcO), bilirubin, lipid, water, etc.) compare to organs. As hepatic function depends primarily upon the tissue oxygen supply, it is clinically essential to record the oxygenation state of the liver in patients after liver transplantation surgery. In this chapter, we demonstrate the evaluation of the light scattering and absorption properties in *in vivo* rat liver tissue on the basis of diffuse reflectance spectroscopy (DRS). Diffuse reflectance spectroscopy is a promising method of identifying the macroscopic characteristic of tissue samples, such as the scattering property, the total hemoglobin concentration, and the tissue oxygen saturation of hemoglobin (StO_2)

[57, 58]. Near-infrared (NIR) spectroscopy has been said to be useful in recognizing the oxygenation state of the graft liver after transplantation, and that the StO_2 parameter can be an indicator of the patient's prognosis [59, 60]. The recent development of DRS has made it feasible to demonstrate the absorption coefficient μ_a and the reduced scattering coefficient μ_s' of a tissue seperately. The absorption coefficient μ_a is explained as the possiblility of photon absorption per unit infinitesimal path length, and the reduced scattering coefficient μ_s' is explained as the possibility of photon scattering per unit infinitesimal path length [48]. Diffuse reflectance spectroscopy is an optical evaluation technique that records fluctuations in the spectral distribution of light after its connection with the tissue. Alterations in the diffuse reflectance spectra are principally a outcome of the combination of absorption and scattering of light for each wavelength of light generated by a broadband light source. Light absorption is fundamentally related to chromophore contents of tissue, on the other hand light scattering is affected predominantly by cellular and sub cellular components of tissue. The entire light absorption is the aggregation of the absorption originating from endogenous chromophores [61]. Oxyhemoglobin and deoxyhemoglobin are the principle absorbers in biological tissues in the visible wavelength range [62], whereas the predominant absorbers in the NIR wavelength range of light are lipids, water, and collagen [63]. The intensity of liver ischemia reperfusion injury can be reliably measured by measuring the alterations in HbO, HbR, and the redox state of heme *aa*3 in cytochrome c oxidase [61]. By irradiating tissue with a defined spectral band of light and following analysis of the characteristic scattering and absorption behaviors, it is possible to determine an optical characteristic of the biological tissue. Such an optical characteristic denotes specific perceptible biochemical and morphological documentation from the examined tissue and might depend on the metabolic rate, vascularity, intravascular oxygenation, and changes in tissue morphology [64]. Diffuse reflectance spectroscopy has been widely used for tissue surface examination during

endoscopical approaches and evaluation of tissue malfunctions in solid organs [65]. Light scattering and absorption characteristics of *in vivo* tissues can be examined by various non-invasive techniques, such as time-resolved measurements [18], a frequency-domain method [66], optical coherence tomography [67], a pulsed photothermal radiometry method [68], and spatially resolved measurements [1, 69-71]. Diffuse reflectance spectroscopy established from the spatially resolved instrumentations with continuous-wave light can be simply obtained by means of a white light source, relatively cost effective optical components, and a spectrometer. The principle remarkable changes within a light spectrum following its interaction with biological tissue are a consequence of either the absorption or scattering of light. Using numerous mathematical algorithms, the spectral characteristics of the absorption coefficient $\mu_a(\lambda)$ and the reduced scattering coefficient $\mu_s'(\lambda)$ can be determined from the calculated reflectance spectrum [72]. Diffuse reflectance spectroscopy employing a fiber optic probe is a rising technique for examining tissue oxygenation, representing favorable outcomes in the differentiation of malignant tissues from healthy tissue [73-76], and evaluation of tissue viability [77]. Moreover, DRS has been explained to recognize irreparable cell degeneration through radiofrequency ablation [78], severe steatosis, and hepatitis, resulting impeding overly substantial surgical removal in these high-risk patients [79-82]. Moreover, DRS could unlikely be used intraoperatively for the evaluation of intestinal viability in real time [83]. Neumerous source-collector geometries have been employed to evaluate the reduced scattering coefficient μ_s' and the absorption coefficients μ_a in DRS using a fiber optic probe [18, 76, 83-86]. Furthermore, a single-reflectance-fiber probe would be easy to implement for experimental uses, especially in clinical conditions. Nonetheless, to our recognition, information related to evaluation of ischemia reperfusion injury by means of a DRS system is very narrow.

In this chapter, we demonstrated about the use of a simple DRS system already established by Nishidate *et al.* [87] to approximate the reduced scattering coefficient spectrum $\mu_s'(\lambda)$ and the absorption coefficient spectrum $\mu_a(\lambda)$ in *in vivo* living tissue. With a aim to prove the authenticity of the method for estimating changes in the optical properties of *in vivo* hepatic tissue, we conducted *in vivo* experiments using exposed rat liver before and during ischemia-reperfusion evoked by the occlusion of the hepatic artery, portal vein, and bile duct and are explained in section 3.3. Section 3.5 discussed about the effect of ischemia-reperfusion on light scattering and absorption properties of rat liver as well as the usefulness of the proposed method.

3.2 Principle

3.2.1 Reflectance-fiber-probe systen

Figure 3.1 demonstrates a illustrative layout of the single-reflectance-fiber-probe setup with the two source-collection configurations employed in the current chapter. The setup comprises of a reflectance-fiber probe, bifurcated fiber, a light source, and two spectrometers under the command of a personal computer. The bifurcated fiber has two optical fibers of the identical diameter of 400 μm positioned simultaneously in the joint end. The reflectance-fiber probe has one 600-μm-diameter fiber in the center enclosed by six 600-μm-diameter fibers. One portion of the center fiber of the reflectance probe is joined to the common end of the bifurcated fiber by means of a fiber connector. A halogen lamp light (HL-2000, Ocean Optics Inc., Dunedin, FL, USA), that traverses the visible to NIR wavelength region, is employed to irradiate the tissue by means of one lead of the bifurcated fiber and the central fiber of the reflectance probe. Diffusely reflected light from the tissue is obtained by both the central fiber and the six surrounding fibers. The center-to-center intervals between the surrounding collections and the central fiber are 700 μm. The light collected by the central fiber is

transported to a multichannel spectrometer (USB4000, Ocean Optics Inc.) by another lead of the bifurcated fiber, besides that collected by the six surrounding fibers is transported to a different multichannel spectrometer (USB4000, Ocean Optics Inc.).

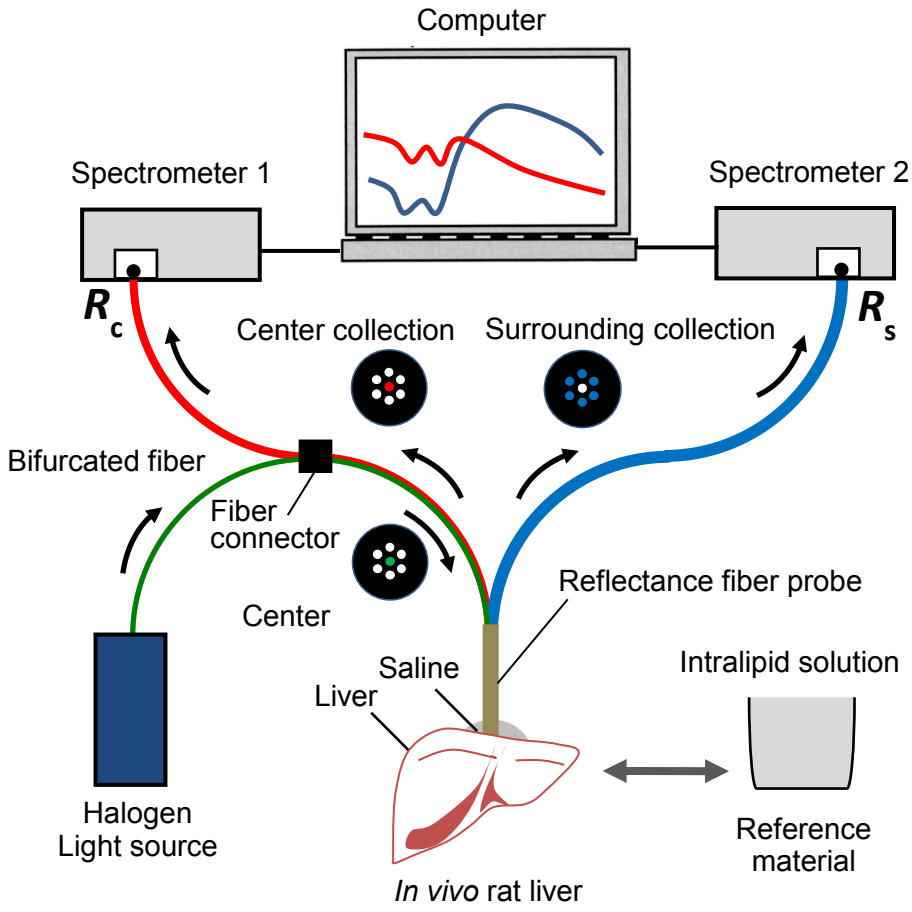

Fig.3.1. A single fiber probe system for estimating the diffuse reflectance spectra with two source-collection geometries setup.

A solution of Intralipid 10% [88] was prepared with a view to adjust the spectral responses of both spectrometers as a reference solution. Diffuse reflectance spectra $R_c(\lambda)$ and $R_s(\lambda)$ in a range from 500 to 800 nm were estimated from the spectral intensities of light recorded by the central fiber and the six surrounding fibers, respectively, on the basis of the reflected intensity spectra obtained from the reference solution.

3.2.2 Determination of empirical formulas for estimating μ_s' and μ_a

With a view to estimate μ_s' and μ_a from the estimations of R_c and R_s, we suppose the following empirical formula on account of the results of the Monte Carlo simulation:

$$\begin{bmatrix} \mu_s' \\ \mu_a \end{bmatrix} = \begin{bmatrix} \alpha_c & \alpha_s \\ \beta_c & \beta_s \end{bmatrix} \begin{bmatrix} A_c \\ A_s \end{bmatrix}, \tag{3.1}$$

where A_c = -log$_{10}R_c$ and A_s = -log$_{10}R_s$ are the apparent absorbances for the recording by the center fiber and the surrounding fibers, correspondingly. In order to develop the accuracy of Eq. (3.1), we applied the higher-order terms of A_c and A_s in Eq. (1) as bellows:

$$\begin{bmatrix} \mu_s' \\ \mu_a \end{bmatrix} = \begin{bmatrix} \alpha_0 & \alpha_1 & \alpha_2 & \alpha_3 & \alpha_4 & \alpha_5 \\ \beta_0 & \beta_1 & \beta_2 & \beta_3 & \beta_4 & \beta_5 \end{bmatrix} \begin{bmatrix} 1 & A_c^2 & A_s^2 & A_c A_s & A_c & A_s \end{bmatrix}^t, \tag{3.2}$$

where coefficients α_i and β_i (i = 0, 1, 2, 3, 4, 5) in Eq. (3.2) can be determined analytically by multiple regression analysis of the results of the Monte Carlo simulations, and [ ]^t denotes the transposition of a vector. The features of the Monte Carlo simulation model were reported previously [87]. In the Monte Carlo simulations, R_c and R_s were measured for the ranges of μ_a=0.1 to 80 cm^{-1} and μ_s'=5.0 to 80 cm^{-1}.

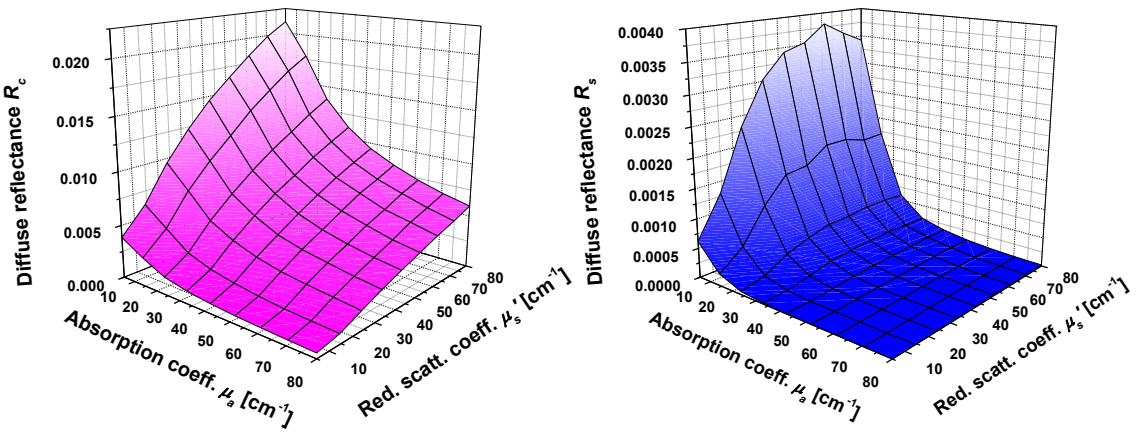

Fig.3.2. Results obtained from the Monte Carlo simulations for (a) R_c collected by the center fiber and (b) R_s collected by the surrounding six fibers.

The values of $\mu_s'(\lambda)$ and $\mu_a(\lambda)$ can be calculated by applying Eq. (3.2) to every wavelength point of $A_c(\lambda)$ and $A_s(\lambda)$. Figures 3.2(a) and 3.2(b) displays the results acquired from the Monte Carlo simulations for R_c and R_s, correspondingly. The estimation of R_c elevated monotonically as μ_s' rises, whereas R_s reaches a plateau for higher values of μ_s'. Both R_c and R_s lessen characteristically as μ_a raises, but the consequence is more prominent for R_s. Figure 3.3 displays the estimated and given values of the reduced scattering coefficient μ_s' [Fig. 3.3(a)] and the absorption coefficient μ_a found from the preliminary numerical investigations [Fig. 3.3(b)]. In both Figs 3.3(a) and 3.3(b), the estimated values well correlate with the given values for given ranges of μ_s' and μ_a. The coefficient of estimation r^2 for μ_a and μ_s' were 0.996 and 0.994, respectively, which represent a good regression.

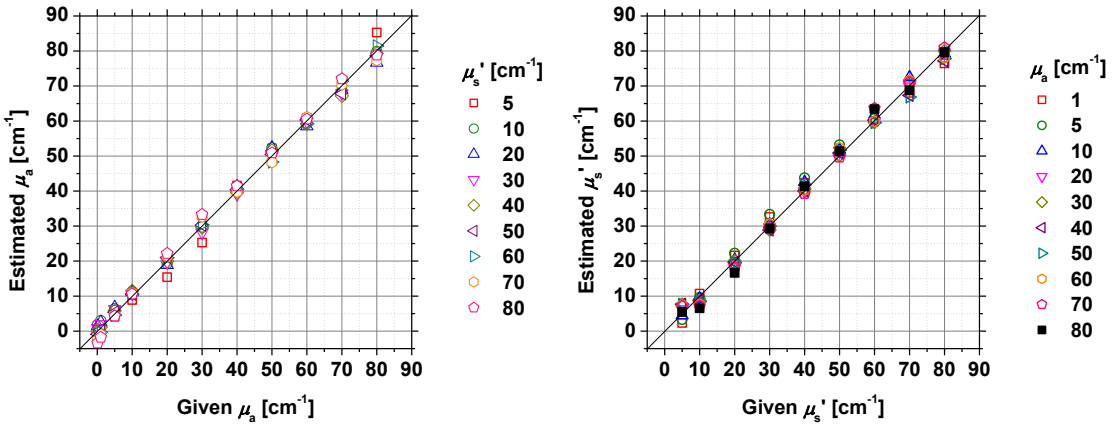

Fig.3.3. Estimated and given values obtained from the numerical investigations for (a) the reduced scattering coefficient μ_s' and (b) the absorption coefficient μ_a.

3.2.3 Evaluation of tissue oxygen saturation and redox state of heme aa3 in cytochrome c oxidase from $\mu_a(\lambda)$

The absorption coefficient spectrum is represented by the sum of absorption originated from oxygenated and deoxygenated hemoglobin. Applying the absorption coefficient spectrum

$\mu_a(\lambda)$ as a dependent variable and the extinction coefficient spectra of $\varepsilon_{HbO}(\lambda)$ and $\varepsilon_{Hb}(\lambda)$ [37] as independent variables, the multiple regression model can be demonstraed as follows:

$$\mu_a(\lambda_k) = a_{HbO} \times \varepsilon_{HbO}(\lambda_k) + a_{Hb} \times \varepsilon_{Hb}(\lambda_k) + a_0 + e(\lambda_k), \tag{3.3}$$

where a_{HbO}, a_{Hb}, and a_0 are the regression coefficients, $e(\lambda_k)$ is an error component, and λ_k reveals discrete values in the wavelength region examined in the analysis. By performing the multiple regression analysis for one sample of the absorption coefficient spectrum comprising of p distinct wavelengths, one set of the three regression coefficients is acquired. In this situation, the regression coefficient a_0 is a constant component or an intercept and demonstrated as follows:

$$a_0 = \bar{\mu}_a - \bar{\varepsilon}_{HbO} \cdot a_{HbO} - \bar{\varepsilon}_{HbR} \cdot a_{HbR}\ , \tag{3.4}$$

where $\bar{\mu}_a$, $\bar{\varepsilon}_{HbO}$, and $\bar{\varepsilon}_{HbR}$ are the means of $\mu_a(\lambda_k)$, $\varepsilon_{HbO}(\lambda_k)$, and $\varepsilon_{HbR}(\lambda_k)$ through the wavelength region, or k = 1 to p. For this chapter, we considered the spectral data in the region of from 500 to 600 nm at distances of 10 nm for the multiple regression analysis since the spectral characteristics of oxygenated and deoxygenated hemoglobin particularly show in this wavelength region. The regression coefficients a_{HbO} and a_{Hb} explains the magnitude of contributions of $\varepsilon_{HbO}(\lambda)$ and $\varepsilon_{Hb}(\lambda)$, respectively, to the absorption coefficient spectrum $\mu_a(\lambda)$ and, accordingly, are intimately analogous to the concentrations C_{HbO} and C_{Hb}, respectively. The oxygen saturation of hemoglobin, StO_2, is illustrated as the proportion of concentration of oxygenated hemoglobin in the concentration of total hemoglobin. In the current chapter, the oxygen saturation is approximated from the regression coefficients a_{HbO} and a_{Hb} as follows:

$$StO_2[\%] = \frac{a_{HbO}}{a_{HbO} + a_{Hb}} \times 100\ . \tag{3.5}$$

We also adopted the measured absorption coefficient spectrum $\mu_a(\lambda)$ to determine the redox state of heme *aa*3 in CcO. There is an isosbestic point of heme *aa*3 around 620 nm, where the absorption of light due to reduced heme *aa*3 and oxidized heme *aa*3 part the equal value, while the absorption spectrum of the reduced heme *aa*3 is maximized at 605 nm [89]. The proportion of absorption at 605 nm and that at 620 nm can be applied to estimate the redox state of heme *aa*3, which represents the state of mitochondrial energy metabolism. Accordingly, we estimated the redox state of heme *aa*3 depending on the ratio of the estimated absorption coefficient at 605 nm and that at 620 nm as $\mu_a(605)/\mu_a(620)$.

With regard to confirm the use of $\mu_a(605)/\mu_a(620)$ to represent the redox state of heme *aa*3 in CcO of liver tissue, we executed the prior experiments with *in vitro* excised liver sample. A normal saline was instilled into the excised liver through the portal vein to discharge blood from the liver tissue. The oxidation of heme *aa*3 in CcO was convinced by repeated infusion of a saline saturated with 95% O_2-5% CO_2 into the liver through the portal vein and consecutive immersion of the liver sample into the saline saturated with 95% O_2-5% CO_2. The reduction of heme *aa*3 in CcO was caused by submersing the liver tissue into the mixture of normal saline and a sodium dithionite ($Na_2S_2O_4$). Figure 3.4 exhibits the estimated absorption coefficient spectra $\mu_a(\lambda)$ normalized at 620 nm found from the excised liver tissue immersed into the saline saturated with 95% O_2-5% CO_2 and the mixture of saline and $Na_2S_2O_4$. The normalized absorption at 605 nm under the hyperoxic situation is larger than that managed with $Na_2S_2O_4$, which resembles to the absorption change because of the reduction of heme *aa*3 in CcO previously published in literature [89].

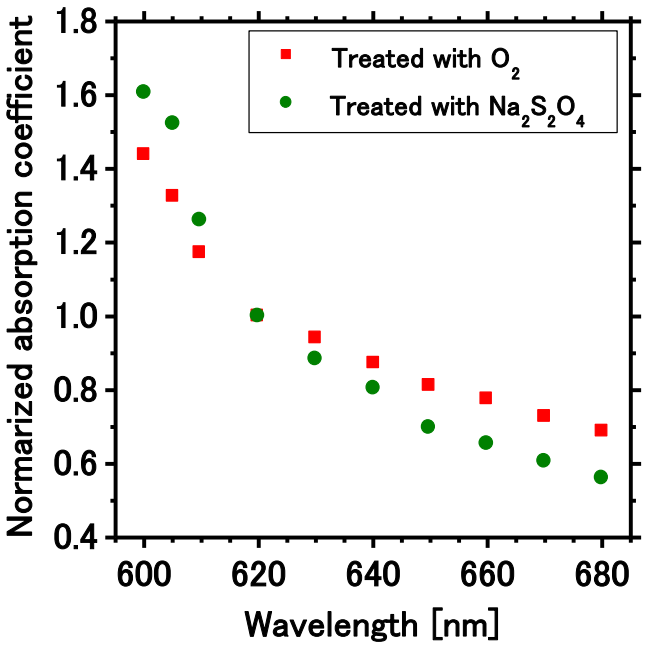

Fig.3.4. Measured absorption coefficient spectra normalized at 620 nm found from the excised rat liver sample submerged into the saline saturated with 95% O_2-5% CO_2 and the mixture of saline and sodium dithionite.

3.3 Experiments

3.3.1 Validation of the Method Using Optical Phantoms

Before the *in vivo* experiments, the experiments with optical phantoms were carried out to validate the empirical model. The phantoms were prepared using Intralipid stock solution (Fresenius Kabi AB, Sweden) as scattering materials. We prepared the scattering solutions by diluting Intralipid stock solution with saline. Hemoglobin solution obtained from red blood cells of horse blood was used as an absorber for smaller values of μ_a, whereas an India ink (R591217, Rotring, Germany) was used for larger values of μ_a. The absorption coefficients of hemoglobin and India ink were experimentally resolved depending on the transmittance measurements of the hemoglobin solution and India ink solution, correspondingly, by means

of a cuvette and a spectrometer. The reduced scattering coefficients of Intralipid solutions were calculated based on the reported values [88]. We prepared 22 phantoms with ranges of μ_a = 0.2 to 93.6 cm^{-1} and μ_s' = 10.3 to 80.4 cm^{-1} in the wavelength range of from 500 to 900 nm to correlate the estimated and given optical properties.

3.3.2 Animal Experiments

Male Wister rats (n=6) with a weight range from 150 to 300 g were maintained at 27°C with a 12/12-hour dark/light cycle and supplimented food and water ad libitum. Experiments conducted in this chapter were authorized by the Animal Research Committee of Tokyo University of Agriculture and Technology. Rats were anaesthetized by intraperitoneal injection of a mixture of α-chloralose (50 mg/kg) and urethane (600 mg/kg). A rat model with 90% ischemia reperfusion to the liver (Fig. 3.5) was accounted [90]. After laparotomy was performed by a longitudinal incision, the ligamentous attachment around the liver lobes were dissected with regard to mobilize the left lobe. In the meanwhile, the hepato-duodenal ligament was taped in construction for further clamping. Prior to onset of ischemia, the diffuse reflectance spectra of liver tissue were documented as baseline values. Hepatic ischemia was initiated by occluding the hepatic portal (the hepatic artery, the portal vein, and the bile duct) for 30 min, with a subsequent declamping. After 60 min of reperfusion, rats were allowed for nitrogen breathing. The caudate lobe of the liver was left as a passage for the portal blood. The reflectance fiber probe was positioned on the dorsal surface of the liver lobe. Assessments of $R_c(\lambda)$ and $R_s(\lambda)$ were performed simultaneously in the wavelength region of from 500 to 800 nm at 30 s intervals for a total of 160 min: oxygen breathing period for 5 min, normal air breathing period for 5 min, ischemic period for 30 min, reperfusion period for 60 min, and finally nitrogen breathing state for another 60 min. With regard to find the respiration arrest or euthanasia, the respiration of the rat was confirmed by monitoring the periodic movement of the lateral region of the abdomen during the experiments.

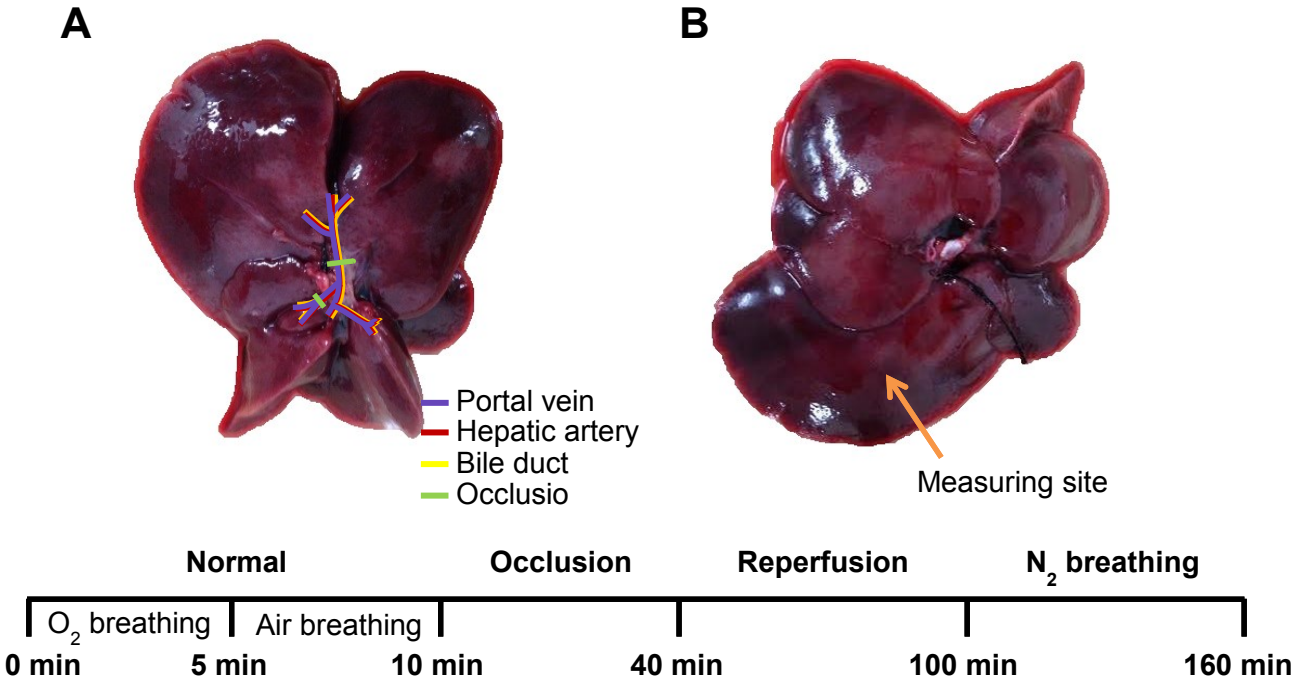

Fig.3.5. Schematic representation of the surgical process on the exposed rat liver and the procedure in the study. (A) Schematic sketching demonstrating the ischemic model of the rat liver by hepatic inflow occlusion on the shafts of the left lobe, median lobe, and right lobe, with no occlusion of the caudate lobe, which is left as a passage of the portal blood. (B) The dorsal surface of the liver lobe is displayed for measurements point for the diffuse reflectance spectra.

Estimation of $\mu_s'(\lambda)$ and $\mu_a(\lambda)$ was executed depending on the procedure described above. Data are expressed as mean ± SD. An unpaired *t*-test was carried out to correlate the mean values over the samples between the normal state (Air breathing) and the other states such as oxygen breathing, ischemia, reperfusion, and nitrogen breathing, and $P < 0.05$ was treated significant.

3.4 Results

3.4.1 Validation of the Method Using Optical Phantoms

Figure 3.6 displays the estimated and given values for (a) the reduced scattering coefficient μ_s' and (b) the absorption coefficient μ_a, achieved from the phantom experimental results. Reasonable results were recorded for both μ_s' and μ_a. Correlation coefficients between the estimated and given values are R = 0.97 (P < 0.0001) and R = 0.98 (P < 0.0001) for μ_s' and μ_a, respectively. The average root mean square error (RMSE) for reduced scattering coefficient, μ_s' is 9.2±8.0%, and that for absorption coefficient. μ_a is 34.9±45.6%.

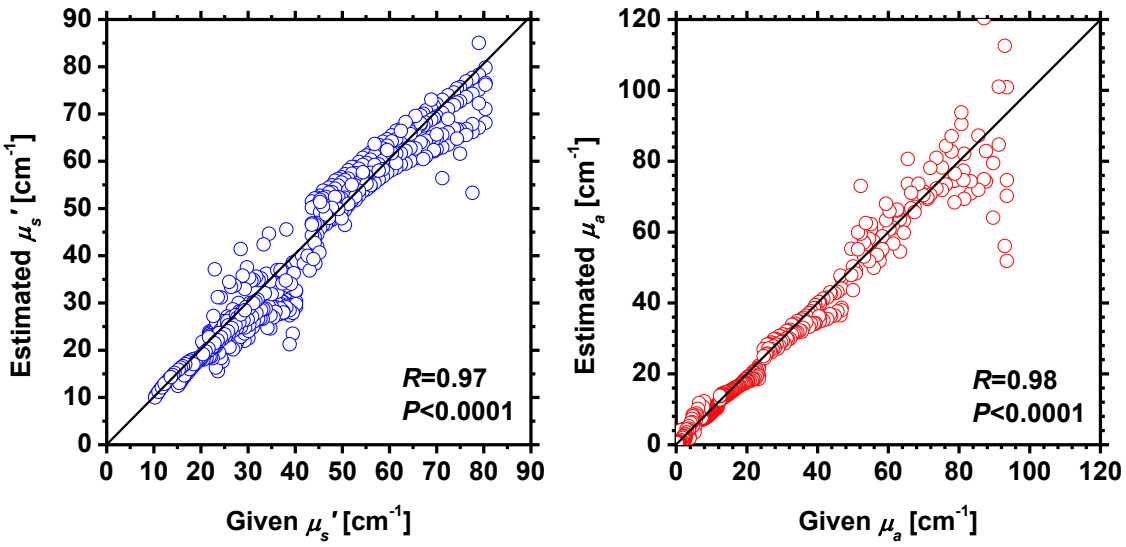

Fig.3.6. Estimated and given values determined from the phantom experimental results for (a) the reduced scattering coefficient μ_s' and (b) the absorption coefficient μ_a.

The empirical model produces, in principle, good results for both μ_s' and μ_a, as demonstrated in Figs. 3.3(a) and 3.3(b). In Fig. 3.6(b), nonetheless, the estimated error for μ_a rises as the given value increases, which could be associated to the fact that the present simulation model does not precisely represent the definite experimental situations, e.g., the distance between the central and surrounding fibers is not taken into examination properly.

3.4.2 Animal Experiments

Figure 3.7 reveals the time series of μ_a averaged over the six samples at specific wavelengths

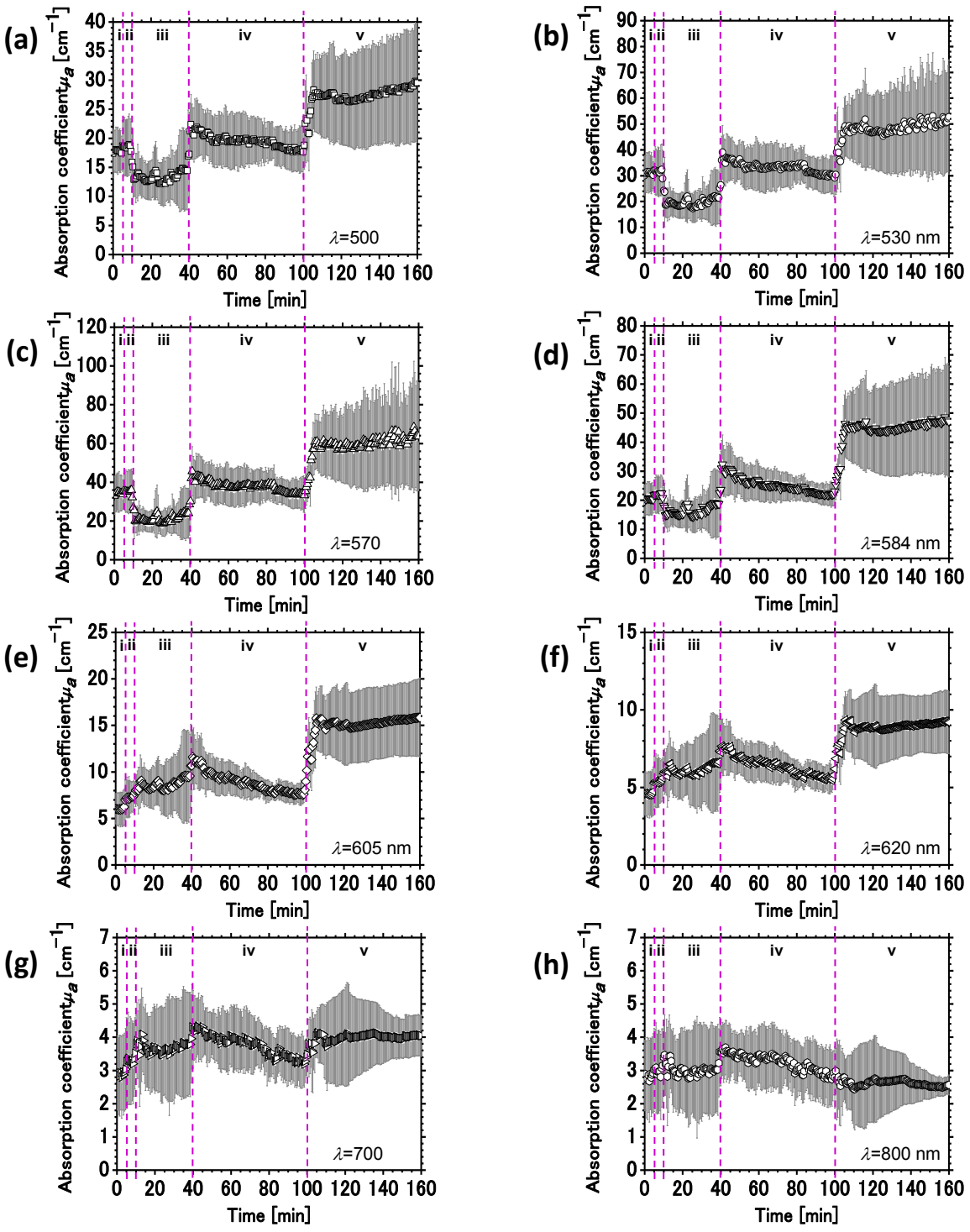

Fig.3.7. Time series of the absorption coefficient μ_a averaged all through the six samples during the periods of ischemia-reperfusion at (a) 500nm, (b) 530nm, (c) 570nm, (d) 584nm, (e) 605nm, (f) 620nm, (g) 700nm and (h) 800 nm wavelengths. Error bars indicate the standard deviation over six rats. The symbols i, ii, iii, iv, and v in each figure represent O_2-breathing, air-breathing, ischemia under air-breathing, reperfusion under air-breathing, and N_2-breathing state, respectively.

throughout the period of pre-ischemia (oxygen breathing and air breathing), ischemia, reperfusion, and nitrogen breathing. The error bars in Fig.3.7 indicate the standard deviation al through the six samples.

The mean values of μ_a over the six samples at every wavelength points are averaged over each period and are demonstrated in Table 3.1 The baseline absorption coefficient at 530 and 570 nm is remarkably higher than at the other wavelengths, which corresponds with the absorption spectrum of oxyhemoglobin [36]. Decreases in μ_a with the initiation of ischemia and increases in μ_a after the reestablishment of blood circulation can be noticed at 500, 530, 570, and 584 nm. These differences in μ_a are representative of a decrease in total hemoglobin concentration since these wavelengths coincide to the isosbestic wavelengths of hemoglobin in the visible wavelength region.

Table 3.1 Table showing the absorption coefficient, μ_a in *in vivo* rat liver tissue at specific wavelengths averaged over the state of oxygen breathing, air breathing, ischemia, reperfusion, and nitrogen breathing. Values are represented as mean ± SD for each state. An unpaired t-test displayed the significant differences between air breathing and the other conditions. *$P <$ 0.05.

$\mu_a(\lambda)$ [cm^{-1}]	O_2 breathing	Air breathing	Ischemia	Reperfusion	N_2 breathing
500 nm	17.77±0.20 *	18.48±0.32	13.48±0.95 *	19.51±1.03 *	27.08±2.04 *
530 nm	30.89±0.48	31.41±0.99	19.81±1.71 *	33.15±1.98 *	47.85±4.17 *
570 nm	34.31±0.61	35.07±1.07	21.55±2.20 *	37.85±2.63 *	59.18±5.75 *
584 nm	20.40±0.26 *	21.93±0.49	16.47±1.67 *	25.21±2.47 *	44.32±4.42 *
605 nm	6.03±0.08 *	7.23±0.13	8.66±0.56 *	8.88±1.05 *	14.99±1.09 *
620 nm	4.60±0.07 *	5.40±0.10	6.14±0.31 *	6.36±0.60 *	8.86±0.48 *
700 nm	2.90±0.07 *	3.31±0.09	3.70±0.16 *	3.77±0.31 *	3.98±0.11 *
800 nm	2.82±0.08 *	3.00±0.10	3.02±0.17	3.24±0.24 *	2.62±0.09 *

The stoppage of total blood inflow to the liver (except for the caudate lobe) yielded in a decrease in μ_a from the baseline ($P < 0.05$) for 500, 530, 570, and 584 nm, and μ_a-values were gradually recovered 60 min after the onset of reperfusion. *In vivo* liver tissues treated in the current chapter demonstrated an absorption coefficient that was greatly correlated to the hemoglobin absorption spectra. The highest baseline of μ_a was 36.02±10.77 cm^{-1} at 570 nm and was 3.15±1.10 cm^{-1} at 800 nm. We observed the significant changes in μ_a between the normal and ischemic liver tissues ($P < 0.05$) in a wavelength range of from 500 to 700 nm, between the normal and reperfused liver tissues ($P < 0.05$) in a wavelength range of from 500 to 800 nm, and between the normal and anoxic liver tissues ($P < 0.05$) for a wavelength range of from 500 to 800 nm, as demonstrated in Table 3.1. In the near infrared wavelength region, the changes in μ_a exist, but the μ_a-value rises during the ischemic period, in compare to the baseline value. Drop in μ_a during ischemia and gradual increases in μ_a with subsequent reperfusion in the visible wavelength range demonstrate that μ_a at the isosbestic wavelengths could be applied as a parameter to estimate the change in total hemoglobin concentration under the hepatic ischemia-reperfusion injury. The period between the initiation of nitrogen breathing and respiratory arrest averaged over all six samples was 87±77 s.

Figure 3.8 demonstrates the time courses of μ_s' averaged over the six samples at specific wavelengths during the time course of pre-ischemia (oxygen breathing and air breathing), ischemia, reperfusion, and nitrogen breathing. The error bars in Fig.8 exhibit the standard deviation over the six samples.

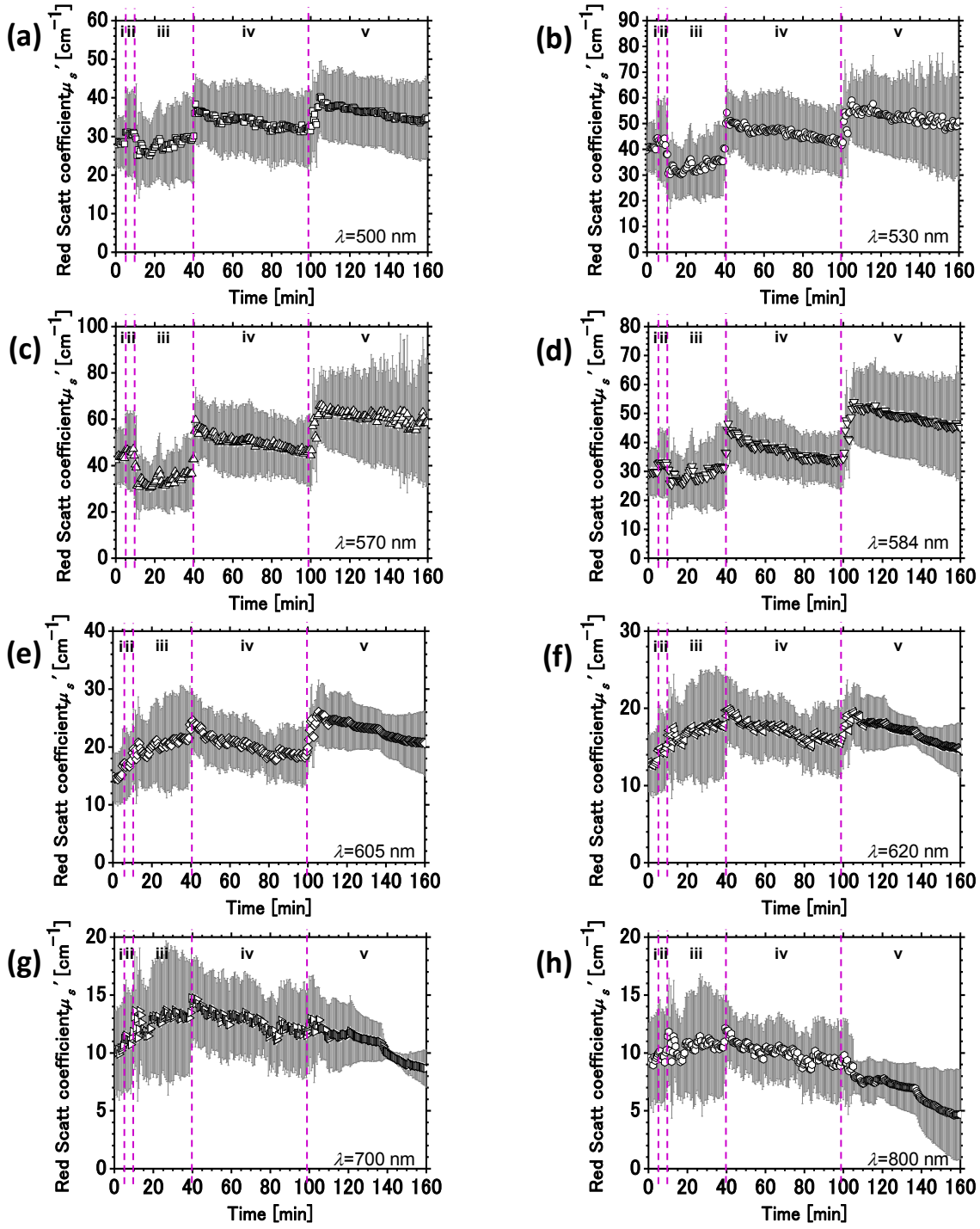

Fig.3.8. Time series of the reduced scattering coefficient μ_s' averaged over the six samples during ischemia-reperfusion experiments at (a) 500nm, (b) 530nm, (c) 570nm, (d) 584nm, (e) 605nm, (f) 620nm, (g) 700nm and (h) 800 nm. Error bars indicate the standard deviation (n=6). The symbols i, ii, iii, iv, and v in each figure represent O_2-breathing, air-breathing, ischemia under air-breathing, reperfusion under air-breathing, and N_2-breathing, respectively.

The mean values of μ_s' over the six samples at each wavelength are averaged over each period and are summarized in Table 3.2. Time courses of μ_s' are well agreed with those of μ_a in the wavelength range of from 500 to 584 nm, which is possibly due to scattering by red blood cells. The mean values of μ_s' at 700 and 800 nm over the ischemia period were significantly ($P < 0.05$) higher than that over the air breathing state. Besides, the average values of μ_s' at 500, 530, 570, and 585 nm over the ischemia period reduced significantly ($P < 0.05$), in compare to the average values of μ_s' over the air breathing state, although the highest value was obtained after the initiation of nitrogen breathing.

Figure 3.9 displays the time courses of StO_2 averaged over six samples during the period of pre-ischemia (oxygen breathing and air breathing), ischemia, reperfusion, and nitrogen breathing. The mean values of StO_2 over each period are summarized in Table 3.3. A strong decrease in StO_2 following onset of ischemia is distinctly noticed. Sixty minutes after the induction of reperfusion, the value of StO_2 recovered gradually but remained lower than the baseline StO_2. The tissue oxygen saturation was recorded to be 59.56±1.58% during oxygen breathing, 45.14±3.86% during normal air breathing before ischemia, 3.60±3.53% after 30 min of ischemia, 33.35±7.27% 60 min after recirculation of blood to the liver, and 4.91±3.40% 60 min after death. The downslope was continuous over the whole 30 min period of ischemia. Therefore, after 30 min of ischemia, the value of StO_2 reduced significantly from the initial value and increased gradually ($P < 0.05$) after 60 min of reperfusion in compare to the ischemic value. Figure 3.10 reveals the time courses of μ_a (605)/μ_a (620) averaged over six samples during the period of pre-ischemia (oxygen breathing and air breathing), ischemia, reperfusion, and nitrogen breathing. The average values of μ_a (605)/μ_a (620) over each period are compiled in Table 3.4. The value of $\mu_a(605)/\mu_a(620)$ increased significantly after the induction of ischemia and returned to the pre-ischemic level after 30 min of onset of

reperfusion. The value of $\mu_a(605)/\mu_a(620)$ increased remarkably under hypoxia and reached to the highest level 10 min after the induction of nitrogen breathing.

3.5 Discussion

The results of this chapter demonstrated that μ_a decreased greatly after the induction of ischemia at the isosbestic wavelengths of hemoglobin in the visible wavelength region that represents the decrease in hemoglobin concentration in hepatic tissue due the occlusion of the hepatic portal.

The value of μ_a for *in vivo* liver tissue is principally altered by the absorption properties of hemoglobin and CcO [91]. Since the hemoglobin absorbs light strongly in the wavelength region of from 500 to 600 nm, the decrease in μ_a at 500, 530, 570, and 585 nm (Figs. 3.7(a), 3.7(b), 3.7(c), and 3.7(d)) after the induction of ischemia are mainly represented by the lower blood level of ischemic liver, as compared to healthy normal liver.

Table 3.2. Table representing the absorption coefficient μ_s' of *in vivo* rat liver tissue at specific wavelengths averaged over the period of oxygen breathing, air breathing, ischemia, reperfusion, and nitrogen breathing. Values are represented as mean ± SD for each period. An unpaired t-test indicated the significant differences between air breathing and the other conditions. *$P < 0.05$.

$\mu_s'(\lambda)$ [cm^{-1}]	O_2 breathing	Air breathing	Ischemia	Reperfusion	N_2 breathing
500 nm	28.32±0.31 *	30.76±0.31	27.87±1.60 *	33.68±1.53 *	38.27±1.63 *
530 nm	40.53±0.41 *	43.13±0.90	33.46±2.21 *	46.42±2.33 *	52.21±2.67 *
570 nm	43.64±0.55 *	46.13±0.81	34.14±2.61 *	50.07±2.94 *	60.72±3.26 *
584 nm	29.64±0.28 *	32.62±0.36	28.89±2.13 *	37.30±3.07 *	48.44±3.00 *
605 nm	14.75±0.22 *	16.96±0.35	20.30±1.12 *	20.23±1.65 *	22.93±1.53 *
620 nm	12.90±0.23 *	14.60±0.35	17.06±0.90 *	17.07±1.16 *	16.90±1.34 *
700 nm	10.25±0.23 *	11.23±0.33	12.92±0.65 *	12.75±0.81 *	10.73±1.22
800 nm	9.38±0.25 *	9.83±0.33	10.60±0.58 *	9.98±0.72	6.77±1.29 *

The significant increases in μ_a at 500, 530, 570, and 585 nm are possibly because of the increase in blood volume in the liver after anoxia, which is consistent with the results of increases liver weight in postmortem animals without immediate bleeding [92-94].

Table 3.3. Tissue oxygen saturation StO_2 of *in vivo* rat liver tissue at specific wavelengths averaged over the period of oxygen breathing, air breathing, ischemia, reperfusion, and nitrogen breathing. Values are displayed as mean ± SD for each period. An unpaired t-test indicated the significant differences between air breathing and the other conditions. *$P < 0.05$.

Parameter	O_2 breathing	Air breathing	Ischemia	Reperfusion	N_2 breathing
StO_2 [%]	59.56±1.58 *	45.14±3.86	3.60±3.53 *	33.35±7.27 *	4.91±3.40 *

The alteration in StO_2 during ischemia and reperfusion were also reasonable, as shown in Fig. 3.9.

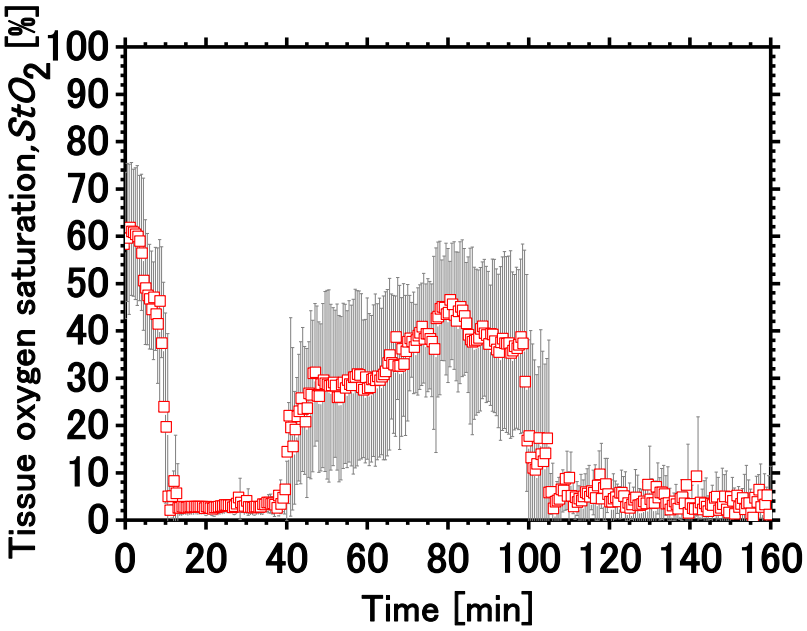

Fig.3.9. Time course of the tissue oxygen saturation StO_2 averaged over the six samples during ischemia-reperfusion experiments. Error bars represent the standard deviation (n=6). The symbols i, ii, iii, iv, and v in each figure represent O_2-breathing, air-breathing, ischemia under air-breathing, reperfusion under air-breathing, and N_2-breathing, respectively.

The value of StO_2 reduced sharply to 1.83±1.39% after the induction of ischemia, besides in the case of reperfusion, the value of StO_2 returned up to 46.24±12.29%, which is as high as that before onset of ischemia (46.05±11.72%) under the normal condition with air breathing.

The results demonstrated in chapter 3 indicated that the present DRS system could efficiently record the changes in StO_2 resulting from the occlusion of blood inflow to the liver, which represents the dysfunction of microcirculation in the liver evoked by ischemia [95]. Liver ischemia-reperfusion damage reduces total hepatic blood flow and causes serious microcirculatory alterations, which consequences in venous stagnation, adversely affecting hepatic tissue oxygenation [96]. The decrease in HbO instantly after occlusion of the hepatic portal vein resulted in a decrease in the StO_2 level.

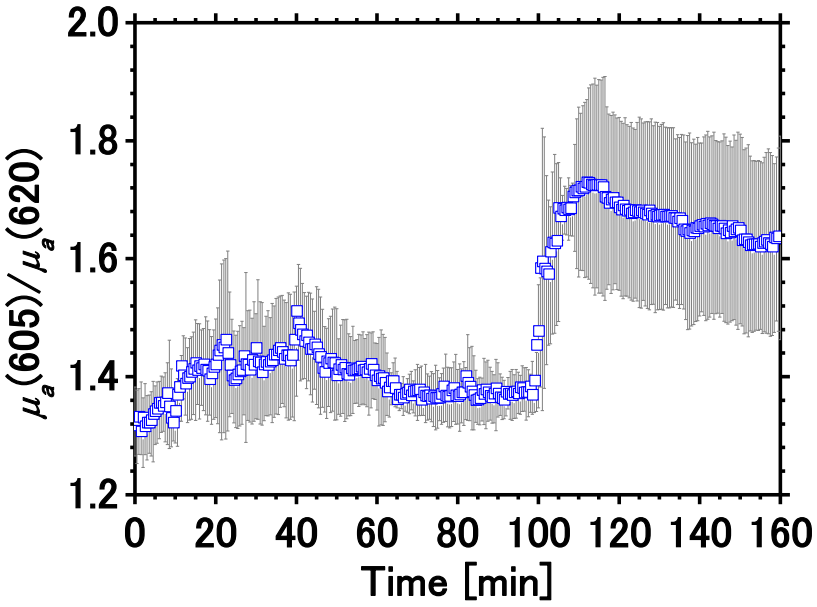

Fig.3.10. Time course of the ratio of μ_a (605) and μ_a (620), averaged over the six samples, during ischemia-reperfusion experiments. Error bars represent the standard deviation (n=6). The symbols i, ii, iii, iv, and v in each figure represent O_2-breathing, air-breathing, ischemia under air-breathing, reperfusion under air-breathing, and N_2-breathing, respectively.

At the end of the reperfusion period, HbO levels gradually recovered, which aids to increase StO_2 following reperfusion [96]. We also noticed significant increases in $\mu_a(605)/\mu_a(620)$ during ischemia and after the initiation of nitrogen breathing (Fig. 3.10), demonstrating a reduction in heme *aa*3, which is a menifestation of mitochondrial energy failure.

Table 3.4. Proportion of $\mu_a(605)/\mu_a(620)$ of *in vivo* rat liver tissue at specific wavelengths averaged over the period of oxygen breathing, air breathing, ischemia, reperfusion, and nitrogen breathing. Values are represented as mean ± SD for each period. An unpaired t-test indicated the significant differences between air breathing and the other conditions. *$P < 0.05$.

Parameter	O_2 breathing	Air breathing	Ischemia	Reperfusion	N_2breathing
$\mu_a(605)/\mu_a(620)$	1.32±0.01 *	1.35±0.01	1.42±0.02 *	1.39±0.03 *	1.66±0.04 *

This is strengthened by the change in absorption spectrum of *in vitro* blood-free liver evoked by the application of $Na_2S_2O_4$ displayed in Fig.3.4. Besides, it has been stated that noninvasive optical evaluation of CcO redox state *in vivo* can suffer from optical cross talk from hemoglobin absorption signals [97, 98]. Therefore, the estimations of heme aa_3 in CcO depending on the value of $\mu_a(605)/\mu_a(620)$ could be differentiated with the changes in the concentrations of oxygenated and deoxygenated hemoglobin. Nonetheless, the probability of relative measurements of redox state of heme aa_3 in CcO of *in vivo* rat liver could still demonstrate valuable. Studies on the multiple regression analysis for the estimated $\mu_a(\lambda)$ with the extinction coefficient spectra of oxygenated hemoglobin, deoxygenated hemoglobin, oxidized heme aa_3, and reduced heme aa_3 would support the method in the future. We will investigate the multiple regression analysis for $\mu_a(\lambda)$ considering those four chromophores further in future work.

It has been stated that ischemia reperfusion may result in post-ischemic microvascular reperfusion injury [99], which is characterized by a decrease in sinusoidal red blood cell velocity [100], ultimately affecting μ_a and μ_s'. The value of μ_s' for *in vivo* liver tissue is altered by light scattering by cellular structures in tissues and red blood cells in microcirculation. The changes in light scattering at 500, 530, 570, and 584 nm (Figs. 3.8(a), 3.8(b), 3.8(c), and 3.8(d)) demonstrate that scattering is highly influenced by red blood cells and is correlated well with the absorption changes of corresponding wavelengths (Figs. 3.7(a), 3.7(b), 3.7(c), and 3.7(d)). On the other hand, the light scattering in the NIR wavelength region (Figs. 3.8(g) and 3.8(h)) is principally affected by changes in tissue morphology. The changes in μ_s' in the near infrared region during the experiments were completely different from those at the isosbestic wavelengths of hemoglobin in the visible wavelength range. The spectrum of the reduced scattering coefficient $\mu_s'(\lambda)$ of biological tissues can be considered as a combination of $\mu_s'(\lambda)$ for cellular and subcellular structures of different sizes [101]. Basically, the sizes of the cellular and subcellular structures in biological tissues are distributed as follows: membranes, < 0.01 μm [102]; ribosomes, < 0.01 μm [103]; vesicles, 0.1 to 0.5 μm [102]; lysosomes, 0.1 to 0.5 μm [104]; mitochondria, 1 to 2 μm [101]; nuclei, 5 to 10 μm [101]; and cells, 5 to 75 μm [101]. Figure 3.11 exhibits the spectra of the reduced scattering coefficient $\mu_s'(\lambda)$ calculated by the Mie theory for spheres of various sizes. In the Mie-theory-based calculation, the refractive indices of a sphere and the surrounding medium were set to be 1.46 and 1.35, respectively, at a volume concentration of 2%. The slope of $\mu_s'(\lambda)$ reduces as the diameter of the sphere d increases. The entire spectrum of $\mu_s'(\lambda)$ increases as the diameter of the sphere d increases in the range of d = 0.01 to 0.2 μm, but decreases as the diameter of the sphere d increases in the range of d = 0.6 to 10.0 μm.

Anoxia has been shown to cause postmortem hepatocyte vacuolation and liver weight increase [92, 93]. Pronounced hepatocyte vacuolation can happen as soon as 30 s after the interruption of organ perfusion *in vitro*, or up to 3 to 4 min after death under an anoxic condition [92, 93]. The hepatocyte vacuoles could be single or multiple and round or oval, and are often well demarcated, with variable displacement of hepatocyte nuclei. Some vacuoles are clear, but most have pale or eosinophilic contents with a homogeneous, granular, and/or fibrillary appearance. A mixed clear/eosinophilic stained appearance has been often noticed within a single vacuole or vacuoles in the same hepatocyte. Intracytoplasmic vacuoles increased in size and number, and hepatocyte vacuolation and sinusoidal congestion enlarged from more centrilobular to periportal areas as the postmortem interval increased [94]. Many reports indicated that hepatocyte vacuoles for rats were 2 to 15 μm in diameter within 15 min after death [92, 93] or up to 25 μm in diameter 25 min after death [94]. As demonstrated in Fig. 3.11, the volume increases in structures larger than 0.6 μm contribute to the decrease in μ_s' in the NIR wavelength region. Hence, the decreases in $\mu_s'(\lambda)$ in the NIR wavelength region after the induction of nitrogen breathing or pulmonary arrest found by the proposed method represent hepatocyte vacuolation. This implies that the irreversible morphological alterations due to the loss of hepatic tissue viability can be assessed using the reduced scattering coefficients estimated by the current DRS system. The reasons of the temporary increase of μ_s' in the NIR region during ischemia remain obscure. One possible interpretation for such a reversible scattering change is the volume changes in structures smaller than 0.2 μm (membranes, ribosomes, small vesicles, and mitochondrial matrix granules), as presented in Fig. 3.11. The severity of hepatocyte damage has been stated to depend on the length of warm ischemia [22, 105]. Short periods of ischemia consequence reversible cell injury, where liver oxygen consumption returns to normal levels when oxygen is resupplied during reperfusion. Reperfusion after more extended periods of ischemia (2 to 3

hours) results in irreversible cell injury. The time limit for hepatocytes survival was approximated to be 1.5 hours of warm ischemia [22, 105]. It has also described that as an ischemia-reperfusion injury, necrosis and apoptosis occur 3 to 6 hours after ischemia-reperfusion [106].

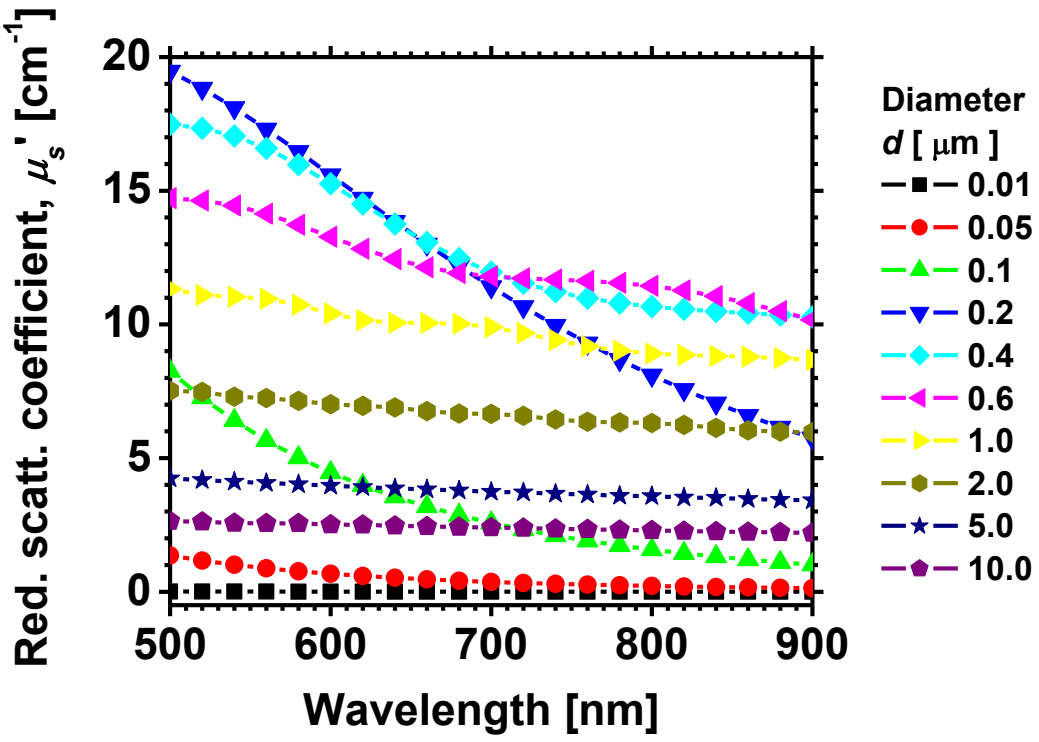

Fig.3.11. Reduced scattering coefficient $\mu_s'(\lambda)$ estimated by the Mie theory for particles of different sizes.

The scattering changes in the NIR wavelength region during reperfusion for at least 6 hours or after more extended periods of ischemia should be investigated in the future. Liver transplantation would be one advantageous clinical application of this technology because an adequate blood supply and tissue oxygenation of the graft is important to its initial function [107, 108]. The results for $\mu_a(\lambda)$, $\mu_s'(\lambda)$, StO_2, and $\mu_a(605)/\mu_a(620)$ demonstrate that the

method applied in this chapter is reliable and has potential clinical application in the intraoperative assessment of graft tissue viability.

3.6 Conclusions

In this chapter, a method for estimating the reduced scattering coefficient, the absorption coefficient, the tissue oxygen saturation, and the reduction of heme *aa*3 of *in vivo* liver tissue using a single-reflectance-fiber probe with two source-collector geometries was investigated. The time courses of μ_a at 500, 530, 570, and 584 nm described in section 3.4 indicated the hemodynamic response in the liver tissue as well as StO_2. Significant changes in $\mu_a(605)/\mu_a(620)$ during ischemia and after death induced by nitrogen inhalation were noticed, representing a reduction in heme *aa*3, which is a menifestation of mitochondrial energy failure. The time courses of μ_s' at 500, 530, 570, and 584 nm were well agreed with those of μ_a, which also indicates the scattering by red blood cells. In contrast, at 700 and 800 nm, a transient rise in μ_s' and an irreversible decrease in μ_s' were observed during ischemia-reperfusion and after death induced by nitrogen breathing, respectively. The change in μ_s' in the NIR wavelength region during ischemia is indicative of the morphological changes in the cellular and subcellular structures induced by ischemia, whereas that after euthanasia implies hepatocyte vacuolation. The results represent the potential application of the current DRS setup in evaluating the pathophysiological conditions of *in vivo* liver tissue. The advantages of the current method demonstrated in chapter 3 are its simplicity and portability, because the only devices required are a white light source, fiber optics, and two spectrometers. As the proposed method can be used to simultaneously evaluate changes in hemodynamics, mitochondrial energy level, and tissue morphology, this method would be useful for studying hepatic tissue viability of *in vivo* liver tissue. The proposed method would be further

extended with a view to investigate pathophysiological conditions of liver tissue, such as those consequences from liver transplantation.

Chapter 4

Quantitative estimation of redox state of heme aa_3 in cytochrome c oxidase of *in vivo* rat liver during ischemia and reperfusion

4.1 Introduction

In the previous chapter, absorption coefficient spectrum $\mu_a(\lambda)$ was measured to assess the redox state of heme *aa*3 in CcO. The proportion of absorption at 605 nm and 620 nm was used to survey the redox state of heme *aa*3. However, the value of μ_a (605)/μ_a (620) could be suffered from optical cross talk of absorption signals of oxygenated hemoglobin and deoxygenated hemoglobin. Therefore, in current chapter, a new method is proposed to assess the oxidation of heme aa_3 using the regression coefficients of oxidized heme and reduced heme evolved from the multiple regression analysis to achieve more accurate estimation of redox state of heme *aa*3.

Liver ischemia-reperfusion could incitehepatocellular injury such as apoptosis; cell death and necrosis, which commonly arise as a sequel of sectional hepatic surgery, liver transplantation and hemorrhagic shock with fluid resuscitation [109]. Post-transplant complexities like hepatic artery occlusion, portal vein thrombosis, primary non-function, and acute graft rejection account deterioration of liver graft microcirculation and tissue hypoxia with eventual loss of the graft without early intercession [110]. Clamping of hepatic portal in the time of partial liver incision directs to ischemia in the remnant liver, while in the time of reperfusion, further liver injury is added to damage that already sustained in course of reperfusion. As liver function depends on tissue oxygen supply, measurement of hepatic

tissue oxygenation has been shown to correlate significantly with the microcirculatory liver failure and liver dysfunction induced by ischemia-reperfusion injury [61]. In hepatocytes, about 90% of the oxygen taken up is consumed by heme aa_3 in CcO in mitochondria [111]. Thus, measurement of the redox state of heme aa_3 in cytochrome c oxidase (CcO) could be used as a potential indicator of cellular energy level [112] and the severity of hepatic ischemia-reperfusion injury [61].

In general, optical assessments, including in vivo spectroscopy, have been widely used for investigation of tissue hemodynamics in liver [113]. Diffuse reflectance spectroscopy provides a good information about tissue components, which is minimally invasive or non-invasive to the *in vivo* biological tissue, and can be fine-tuned for the specific clinical application by the alteration of source-detector-separation, the fiber geometry, and/or the wavelength range [72]. The spectral shape and magnitude is reflective of the absorption and scattering properties of the tissue. Therefore, the wavelength dependent absorption and reduced scattering coefficients of the tissue (μ_a and μ_s' respectively) can be extracted applying diverse theoretical and numerical models. Subsequently, the collected spectral information is further translated into morphologic and physiologic information.

In the previous chapter a method was investigated with a single-reflectance optical fiber probe to assess the reduced scattering coefficient spectrum $\mu_s'(\lambda)$, the absorption coefficient spectrum $\mu_a(\lambda)$, the tissue oxygen saturation StO_2, and the reduction of heme aa_3 in CcO of *in vivo* liver tissue [114]. The technique measured the StO_2 based on the regression coefficients achieved from the multiple regression analysis using the estimated absorption coefficient spectrum $\mu_a(\lambda)$ as a response variable and the elimination of coefficient spectra of oxygenated hemoglobin and deoxygenated hemoglobin as predictor variables. On the contrary, the proportion of μ_a at 605 nm and at 620 nm was used to assess the oxidation of heme aa_3 in CcO. Primarily, optical evaluation of a chromophore *in vivo* can suffer from

optical cross talk from absorption signals by the other chromophores. Therefore, the measurements of StO_2 achieved from technique could be varied with the alterations in the concentrations of oxidized heme aa_3 and reduced heme aa_3. Accordingly, the value of μ_a (605)/μ_a (620) could be fluctuated by the alterations in the concentrations of oxygenated hemoglobin and deoxygenated hemoglobin. For more authentic assessment of the tissue oxygen saturation and the redox state of heme aa_3, the above four chromophores should be taken into account in the analysis of the estimated μ_a (λ).

In this study, we stated a novel technique of the multiple regression analysis for the estimated μ_a (λ) with the extinction coefficient spectra of oxygenated hemoglobin, deoxygenated hemoglobin, oxidized heme aa_3, and reduced heme aa_3. In order to ascertain the efficacy of the technique for assessing the tissue oxygen saturation and the oxidation of heme aa_3 in CcO of liver tissue, we conducted *in vivo* analysis using exposed rat liver before and at the time of ischemia-reperfusion produced by the occlusion of the hepatic portal.

4.2 Principle

4.2.1 Reflectance-fiber-probe system

The reflectance-fiber-probe system with the two source-detection geometries introduced by Nishidate et al., [87] was used in the current study. The system composed of a light source, bifurcated fiber, a reflectance-fiber probe, and two spectrometers under the guidance of a personal computer. The bifurcated fiber has two optical fibers of the same diameter of 400 μm arranged side by side in the common end. The reflectance-fiber probe has a 600-μm-diameter fiber in the center enclosed by six 600-μm-diameter fibers. One end of the center fiber of the reflectance fiber probe is attached to the common end of the bifurcated fiber through a fiber connector. A halogen lamp light source (HL-2000, Ocean Optics Inc., Dunedin, FL, USA), which covers the visible to NIR wavelength range, is used to illuminate

the liver tissue via one lead of the bifurcated fiber and the central fiber of the reflectance fiber probe. Diffusely reflected light from the sample is recognized by both the central fiber and the six surrounding fibers. The center-to-center width among the central fiber and the surrounding fibers are 700 μm. The light recognized by the central fiber is passed to a multichannel spectrometer (USB4000, Ocean Optics Inc.) via another lead of the bifurcated fiber, whereas that detected by the six surrounding fibers is delivered to the other multichannel spectrometer (USB4000, Ocean Optics Inc.). A solution of Intralipid 10% [88] was used to calibrate the spectral responses of both spectrometers as a reference material. Diffuse reflectance spectra $R_c(\lambda)$ and $R_s(\lambda)$ ranging from 500 to 800 nm were determined from the spectral intensities of light detected by the central fiber and the six neighboring fibers, respectively, based on the spectra of reflected light strength from the reference material.

4.2.2 Determination of empirical formulas for estimating μ_s' and μ_a

Figure 4.1 (a) demonstrates the flow diagram of the protocol for evaluating μ_s' and μ_a from the analysis of R_c and R_s. We looked at the following experimental equation based on the conclusions of the Monte Carlo simulation:

$$\begin{bmatrix} \mu_s' \\ \mu_a \end{bmatrix} = \begin{bmatrix} \alpha_c & \alpha_s \\ \beta_c & \beta_s \end{bmatrix} \begin{bmatrix} A_c \\ A_s \end{bmatrix}, \tag{4.1}$$

where $A_c = -\log_{10}R_c$ and $A_s = -\log_{10}R_s$ are the supposed absorbances for the documentation by the center fiber and the neighboring fibers, respectively. In order to advance the truthfulness of Eq. (4.1), we applied the higher-order terms of A_c and A_s in Eq. (4.1) as follows:

$$\begin{bmatrix} \mu_s' \\ \mu_a \end{bmatrix} = \begin{bmatrix} \alpha_0 & \alpha_1 & \alpha_2 & \alpha_3 & \alpha_4 & \alpha_5 \\ \beta_0 & \beta_1 & \beta_2 & \beta_3 & \beta_4 & \beta_5 \end{bmatrix} \begin{bmatrix} 1 & A_c^2 & A_s^2 & A_c A_s & A_c & A_s \end{bmatrix}^t, \tag{4.2}$$

where [ ]^t show the transposition of a vector. Coefficients α_i and β_i (i = 0, 1, 2, 3, 4, 5) in Eq. (4.2) can be resolved statistically by multiple regression analysis of the conclusions of the Monte Carlo simulations as shown in Fig.4.1 (b). The particular of the Monte Carlo simulation model were reported earlier [114, 87].

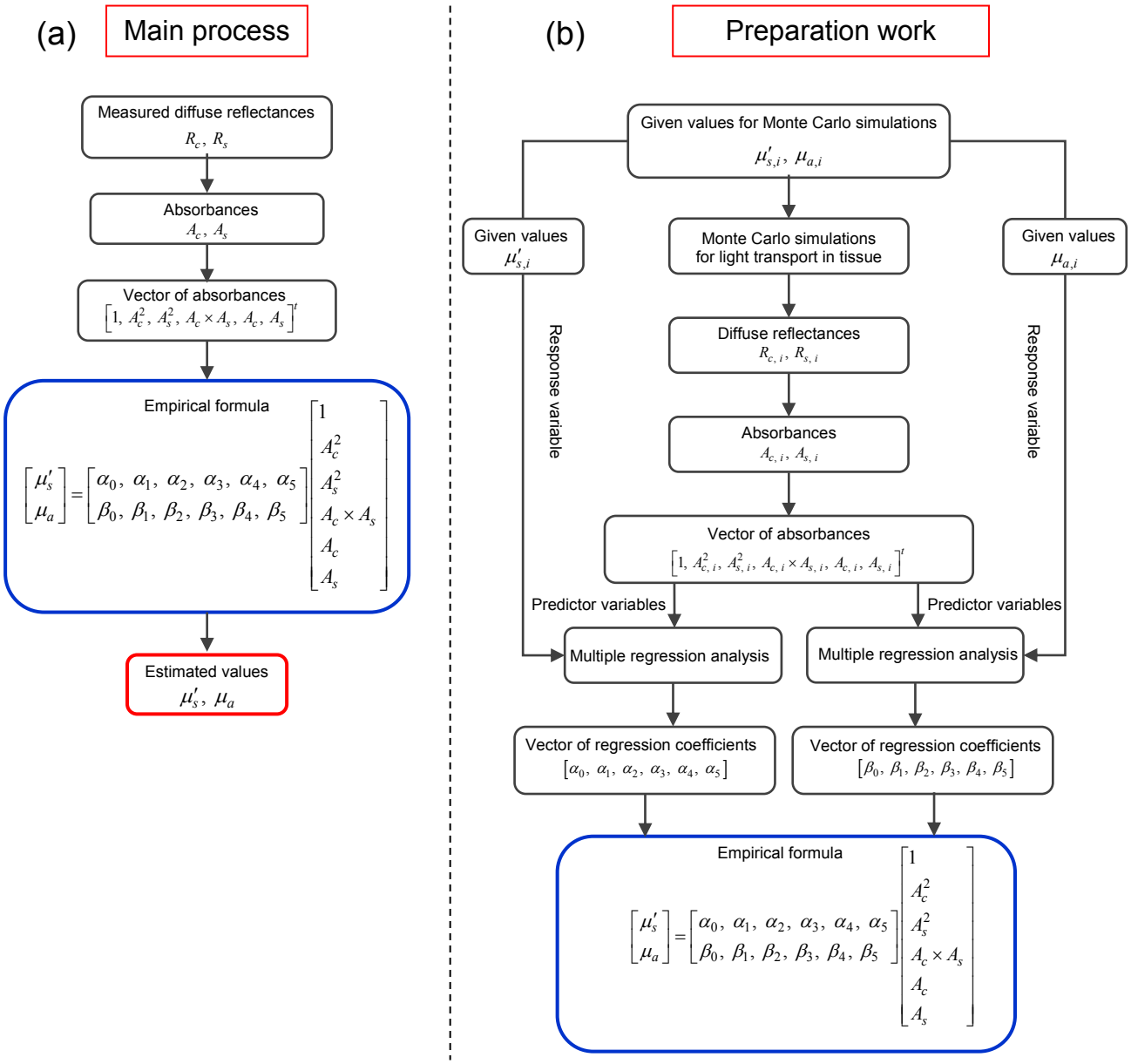

Fig.4.1. Flow diagram of the protocol for evaluating μ_s' and μ_a from the determined diffuse reflectance R_c and R_s. (a) Principal protocol toestimate μ_s' and μ_a and (b) Formation of experiment for measuring experimental equation

In the Monte Carlo simulations, R_c and R_s were computed for the ranges of μ_a=0.1 to 80 cm^{-1} and μ_s'=5.0 to 80 cm^{-1}. The values of $\mu_s'(\lambda)$ and $\mu_a(\lambda)$ can be measured by using Eq. (4.2) to each wavelength point of $A_c(\lambda)$ and $A_s(\lambda)$.

4.2.3 Evaluation of tissue oxygen saturation and redox state of heme aa_3 in cytochrome c oxidase from $\mu_a(\lambda)$

The absorption coefficient spectrum is accustomed by the total of absorption due to oxygenated hemoglobin, deoxygenated hemoglobin, oxidized heme aa_3, and reduced heme aa_3. Applying the absorption coefficient spectrum $\mu_a(\lambda)$ as a dependent variable and the extinction coefficient spectra of $\varepsilon_{HbO}(\lambda)$ [36], $\varepsilon_{HbR}(\lambda)$ [36], $\varepsilon_{HmO}(\lambda)$ [115] and $\varepsilon_{HmR}(\lambda)$ [115] as independent variables, the multiple regression model can be pointed as follows:

$$\mu_a(\lambda_k) = a_{HbO} \times \varepsilon_{HbO}(\lambda_k) + a_{HbR} \times \varepsilon_{HbR}(\lambda_k) + a_{HmO} \times \varepsilon_{HmO}(\lambda_k) + a_{HmR} \times \varepsilon_{HmR}(\lambda_k) + a_0 + e(\lambda_k), \quad (4.3)$$

where a_{HbO}, a_{HbR}, a_{HmO}, a_{HmR}, and a_0 are the regression coefficients, $e(\lambda_k)$ is an error component, and λ_k indicates discrete values in the wavelength range treated in the analysis. Subscripts *HbO*, *HbR*, *HmO*, and *HmR* denote oxygenated hemoglobin, deoxygenated hemoglobin, oxidized heme aa_3, and reduced heme aa_3, respectively. By applying the multiple regression analysis for one sample of the absorption coefficient spectrum composed of p discrete wavelengths, one set of the three regression coefficients is achieved. In this case, the regression coefficient a_0 is a constant term or an intercept and pointed as follows:

$$a_0 = \bar{\mu}_a - \bar{\varepsilon}_{HbO} a_{HbO} - \bar{\varepsilon}_{HbR} a_{HbR} - \bar{\varepsilon}_{HmO} a_{HmO} - \bar{\varepsilon}_{HmR} a_{HmR}, \quad (4.4)$$

where $\bar{\mu}_a$, $\bar{\varepsilon}_{HbO}$, $\bar{\varepsilon}_{HbR}$, $\bar{\varepsilon}_{HmO}$, and $\bar{\varepsilon}_{HmR}$ are the averages of $\mu_a(\lambda_k)$, $\varepsilon_{HbO}(\lambda_k)$, $\varepsilon_{HbR}(\lambda_k)$, $\varepsilon_{HmO}(\lambda_k)$, and $\varepsilon_{HmR}(\lambda_k)$ over the wavelength range, or k = 1 to p. In the current study, we valued the spectral data in the range of from 520 to 600 nm at distance of 10 nm for the multiple regression investigation because the spectral features of oxyhemoglobin, deoxyhemoglobin,

oxidized heme aa_3, and reduced heme aa_3 notably show in this wavelength range. The regression coefficients a_{HbO}, a_{HbR}, a_{HmO}, and a_{HmR} describe the degree of contributions of $\varepsilon_{HbO}(\lambda)$, $\varepsilon_{HbR}(\lambda)$, $\varepsilon_{HmO}(\lambda)$ and $\varepsilon_{HmR}(\lambda)$, respectively, to the absorption coefficient spectrum $\mu_a(\lambda)$ and, consequently, are nearly relevant to the concentrations of oxyhemoglobin, deoxyhemoglobin, oxidized heme aa_3, and reduced heme aa_3, respectively. The oxygen saturation of hemoglobin, StO_2, is defined as the proportion of the oxyhemoglobin concentration in the total hemoglobin concentration. In this study, the oxygen saturation is measured from the regression coefficients a_{HbO} and a_{HbR} as follows:

$$StO_2 = \frac{a_{HbO}}{a_{HbO} + a_{HbR}}. \tag{4.5}$$

Accordingly, we also valued the measured absorption coefficient spectrum $\mu_a(\lambda)$ to assess the oxidation of heme aa_3 in CcO. In this study, we stated a novel technique to assess the oxidation of heme aa_3 ($OHaa_3$) applying the regression coefficients a_{HmO} and a_{HmR} as follows:

$$OHaa_3 = \frac{a_{HmO}}{a_{HmO} + a_{HmR}}. \tag{4.6}$$

Therefore, the present assessment on the oxidation of heme aa_3 is distinct from the ratio metric measurement stated proposed in the earlier chapter in particular of the application of the regression coefficients a_{HmO} and a_{HmR}. The present assessment applies the regression coefficients a_{HmO} and a_{HmR} obtained from the multiple regression assessment to measure the redox state of heme aa_3 in CcO whereas the earlier assessment [114] relies on the proportion of μ_a (605) and μ_a (620). On the contrary, there are two coincidences among the present assessment and earlier one [114]. One is the technique for measuring μ_s' and μ_a from the diffuse reflectance R_c and R_s computed by the reflectance fiber probe system established by

Nishidate *et al.*[114, 87]. The other is the use of wavelength-dependences of absorption by both reduced heme aa_3 and oxidized heme aa_3 to measure the redox state of heme aa_3 in CcO.

4.3 Experiments

Six male Wister rats weighing from 132 to 458 g were reared at 27°C with a 12/12-hour dark/light cycle and supplemented with food and water ad libitum. Experiments conducted in the current study were favored by the Animal Research Committee of Tokyo University of Agriculture and Technology. Rats were anaesthetized by intraperitoneal injection of a mixture of α-chloralose (50 mg/kg) and urethane (600 mg/kg). After conducting laparotomy by a transversal incision, the ligaments around the liver lobes were dissected in order to mobilize the left lobe. At the same time, the hepato-duodenal ligament was taped in preparation for further clamping. Hepatic ischemia was caused by clamping the hepatic portal (the hepatic artery, the portal vein, and the bile duct) for 30 min, followed by declamping. Anoxic condition was induced by nitrogen breathing at 60 min after the onset of reperfusion to sacrifice the rats. The caudate lobe of the liver was kept as a passage for the portal blood. The reflectance fiber probe was fixed on the surface of the liver lobe. Measurements of $R_c(\lambda)$ and $R_s(\lambda)$ were achieved concurrently in the wavelength range from 500 to 800 nm at 30 s intervals for 100 min: oxygen breathing for 5 min, normal air breathing for 5 min, ischemia for 30 min, and reperfusion for 60 min. Estimation of $\mu_s'(\lambda)$ and $\mu_a(\lambda)$ was conducted based on the protocol explained above. Data are showed as mean ± SD. An unpaired *t*-test was conducted in order to correlate the mean values over the samples among the normal (Air breathing) and the other periods (oxygen breathing, ischemia, and reperfusion) and $P < 0.05$ was considered significant.

4.4 Results and Discussion

Figure 4.2 (a) reveals the actual time courses of *OHaa$_3$* during pre-ischemia (oxygen breathing and air breathing), ischemia, and reperfusion.

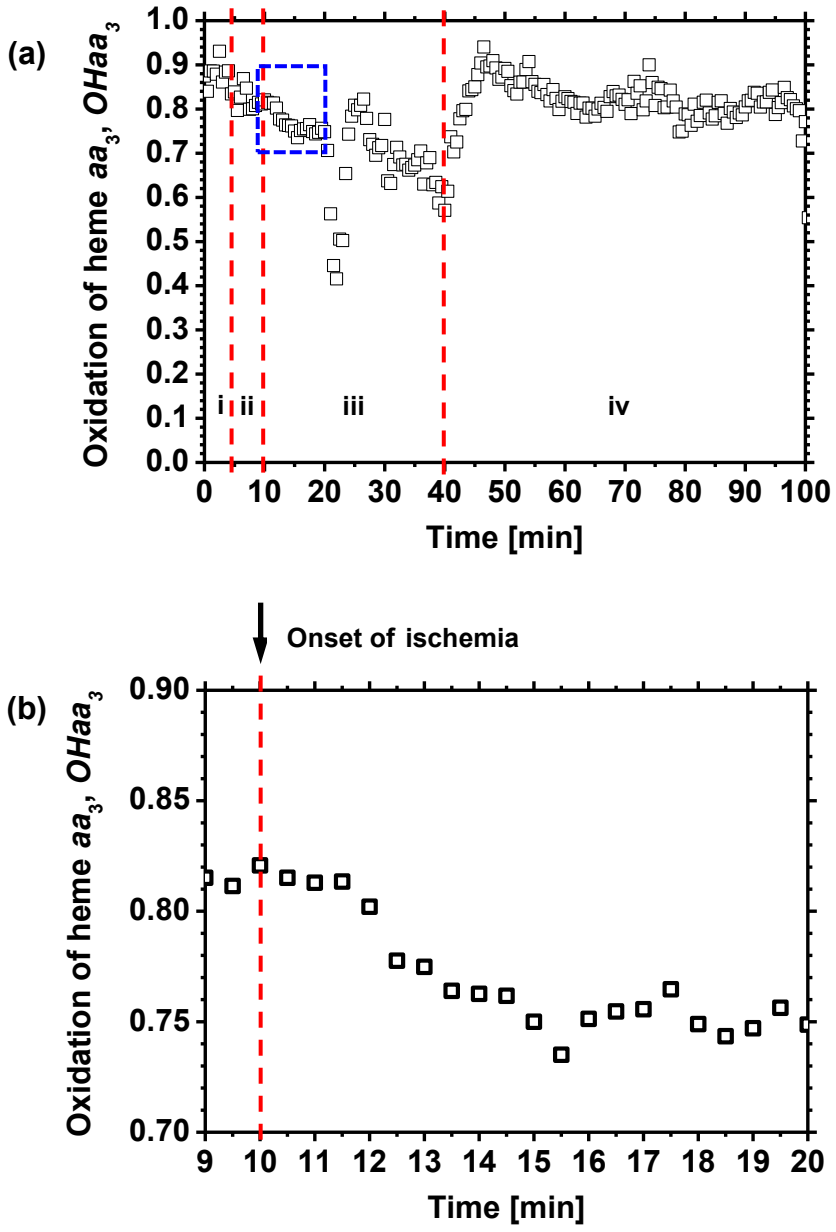

Fig.4.2 (a). Time course of the oxidation of heme in cytochrome c oxidase OHaa$_3$ at the time of ischemia-reperfusion experiments. Roman numerals, i, ii, iii, and iv show oxygen breathing, air breathing, ischemia under air breathing, and reperfusion under air breathing, respectively.(b) Magnified aspect of the part confined by a dashed blue square in figure (a).

Magnified aspect of the part confined by a dashed blue square in Fig.4.2 (a) is also shown in Fig.4.2 (b). The mean values of $OHaa_3$ averaged over six samples are averaged over each period and are compiled in Fig. 4.3. In the earlier study [114], the tissue oxygen saturation StO_2 was promptly dropped immediately after the onset of ischemia and was decreased to around 0% at 1 min after the onset of ischemia. In contrast, $OHaa_3$ achieved from the stated technique was not changed immediately after the onset of ischemia as shown in Fig.4.2 (b).

The value of $OHaa_3$ was significantly declined at 2 min after the onset of ischemia, describing a reduction in heme aa_3, which is a symptom of mitochondrial energy failure. After 40 min of reperfusion, the value of $OHaa_3$ reverted to the pre-ischemic level. It should be esteemed that $OHaa_3$ started constantly declining at 2 min after the onset of ischemia and was not synchronized with the tissue oxygen saturation. This may be due to the difference in oxygen affinity among the heme *aa*3 in CcO and hemoglobin and corresponds to the relationship between the relative oxidation state of cytochrome c oxidase with respect to the relative oxygenation state of hemoglobin [116]. Hoshi et al., [116] repoted that the redox state of cytochrome c oxidase was resided stable and independent of the oxygen state of hemoglobin until the relative alteration in oxygen state of hemoglobin decreased to approximately 40%. In the range of lower than this level of the relative alteration in oxygenation state of hemoglobin, the cytochrome c oxidase was decreased about linearly with the decrease in the oxygen state of hemoglobin. In our earlier report [114], immediately after the onset of ischemia, the index of reduction of heme aa_3 explained by the proportion of $\mu_a(605)/\mu_a(620)$ that was rapidly increased and was synchronized with the tissue oxygen saturation StO_2. Distinction in the time course among $OHaa_3$ during ischemia shown in Fig.4.2 and $\mu_a(605)/\mu_a(620)$ stated in the earlier study [114] that the stated technique with

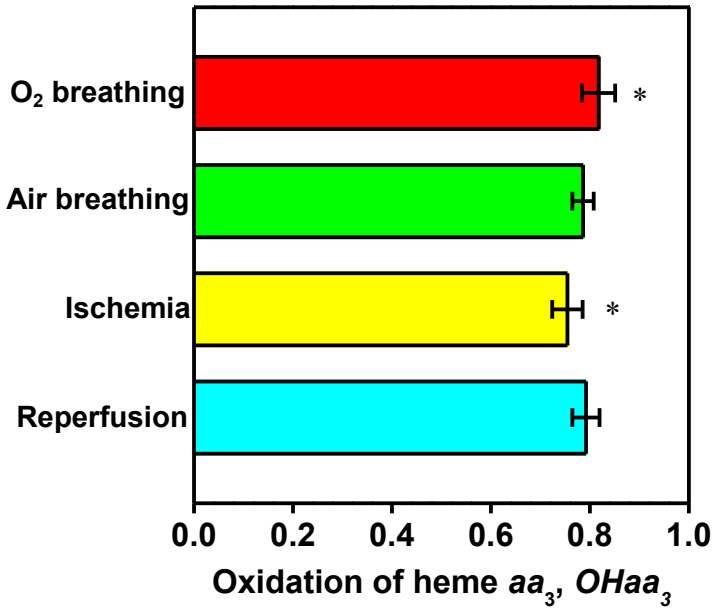

Fig.4.3. Mean values of the oxidation of heme aa_3 in cytochrome *c* oxidase $OHaa_3$ over the six samples averaged over each period. Unpaired *t*-test showed the significant differences among the air breathing phase with the ischemic phase. $*P < 0.05$.

$OHaa_3$ is efficient in reduction of optical cross talk among hemoglobin and heme aa_3. The average value of $OHaa_3$ was 0.82±0.03 in the time course of oxygen breathing, 0.79±0.02 at normal air breathing before ischemia, 0.75±0.03 at ischemia, and 0.79±0.03 at reperfusion. The outcomes demonstrated that the current DRS system could efficiently monitor the reduction of heme *aa*3 in CcO arising from the hepatic occlusion, which reflects the ischemia-induced microcirculatory dysfunction in the liver [95, 100]. Liver transplantation would be one effective clinical application of this technology because an adequate blood supply and tissue oxygenation of the graft is fundamental to its basic activity [107, 108]. The results for $\mu_a(\lambda)$, $\mu_s'(\lambda)$, StO_2, and $OHaa_3$ point out that the technique tested in the current study is dependable and has probable application in the intraoperative assessment of graft tissue viability.

4.5 Conclusions

In the current chapter, a new method was proposed for measuring the reduced scattering coefficient, the absorption coefficient, the tissue oxygen saturation, and the oxidation of heme aa_3 in cytochrome c oxidase of *in vivo* liver tissue appying a single-reflectance-fiber probe system. Distinction in the time course between $OHaa_3$ and the conventional ratio metric analysis with $\mu_a(605)/\mu_a(620)$ showed that the stated technique could definitely reduce optical cross talk between hemoglobin and heme aa_3. The results showed in section 4.4 imply the possible application of the current DRS system in measuring the oxygen levels and pathophysiological conditions of *in vivo* liver tissue. Since the stated technique can be used concurrently measure the alterations in hemodynamics, mitochondrial energy level, and tissue morphology, this technique will be efficient for examining pathophysiological conditions of *in vivo* liver.

Chapter 5

In vivo imaging of hemodynamics and tissue morphology during hepatic ischemia-reperfusion in rats based on spectrocolorimetry

5.1. Introduction

In chapter 5, a method is proposed to visualize the concentration of oxyhemoglobin, deoxyhemoglobin, total hemoglobin, tissue oxygen saturation and scattering power of *in vivo* liver tissue during ischemia-reperfusion based on RGB imaging. This method first determines the concentration of oxyhemoglobin, deoxyhemoglobin, and scattering power. Total hemoglobin concentration and tissue oxygen saturation is then evolved from the assessment of oxyhemoglobin and deoxyhemoglobin.

Ischemia and subsequent reperfusion of the liver tissue can appear in a number of clinical settings like those accomplished with low-flow states, or temporary occlusion of the supplying blood vessels at the time of liver transplantation, and to a large extent in liver resection surgery. Hepatic ischemia-reperfusion is characterized by circulatory derangement, along with decreases in sinusoidal diameters and blood flow, increases in the heterogeneity of the hepatic microvascular perfusion, and even total cessation of blood flow within individual sinusoids [117]. Therefore, ischemia-reperfusion impairment to donor liver tissue is speculated to be one vital cause that may show a role in the downturn of posttransplant graft function and ultimately rejection. In liver transplantation, normothermic ischemia-reperfusion causes up to 10% of early graft rejections [109]. Hepatocellular damage caused by ischemia-reperfusion correlates with the extent of microcirculatory reperfusion failure after portal-triad

cross-clamping [118]. For liver transplantation, the hepatic pedicle is temporarily clamped (Pringle maneuver) [20] to restrict the blood inflow and to reduce intraoperative blood loss, which results in deprivation of tissue oxygen level, depletion of energy production converting cellular metabolism into anaerobic pathways. The resulting hepatic ischemia, along with subsequent reperfusion causes ischemia-reperfusion injury and structural changes in hepatic tissue of varying extents, which also alters the scattering properties of light. The spectrum of reduced scattering coefficient $\mu_s'(\lambda)$ of liver tissue follows a power low function [104, 119], that can be approximated in the following form;

$$\mu_s'(\lambda) = a\lambda^{-b} \tag{5.1}$$

Where *a* is the scattering amplitude and *b* is the scattering power that has been associated to the geometrical properties such as scatterer density [120] and size [121], respectively. Reduced scattering coefficient spectrum $\mu_s'(\lambda)$ of biological tissues is considered as the combination of $\mu_s'(\lambda)$ for cellular and subcellular structures of different sizes [101]. The changes in scattering during ischemia are thought to be originated from the changes in those cellular and subcellular structures induced by ischemia, though that after anoxia signifies the hepatocyte vacuolation [92,93,114]. Thus, it is important to measure the scattering power, *b* to evaluate the morphological changes in liver tissue resulting from ischemia, reperfusion and anoxia. The estimated scattering power, *b* could be used for calculating the scatterer size and scattering particle distribution of liver tissue.

Hepatic ischemia-reperfusion results in a cascade of events leading to a number of cellular changes that evolve over time and space. Monitoring the spatio-temporal characteristics of changes in hemoglobin concentrations and tissue oxygen saturation is crucial for studying the pathophysiologic condition of liver tissue. Moreover, evaluation of hepatic tissue oxygenation has been demonstrated to correspond significantly with the microcirculatory

derangement and hepatic malfunction induced by ischemia-reperfusion. Rectification of blood flow to the liver tissue shows a vital requirement for improvement of cellular and organ function, which typically provoke the ischemia-induced tissue impairment. Moreover, during reperfusion an additional impairment is supplemented to the impairment already sustained at the time of ischemia [56].

Several studies have been proposed that postischemic reperfusion is correlated with incomplete energy supply, and subsequent reduction of hepatic tissue oxygen saturation [118], impairment of mitochondrial adenosine triphosphate (ATP) regeneration [122], along with incomplete recovery of hepatocellular excretory function [123]. Hypoxic or ischemic impairment of hepatic sinusoidal endothelium is usually treated to be the first pathological alteration in the cascade of events resulting in ischemia-reperfusion injury in the expression of graft malfunction [124]. Ischemia-reperfusion injury is closely related to an increase incidence of rapid decrease in tissue oxygen saturation StO_2, reduction of heme aa_3 in cytochrome c oxidase indicating mitochondrial dysfunction, hepatocellular injury as for example apoptosis, necrosis, and cell death [55]. On reentray of blood into the organ during reperfusion, there is excess production of toxic oxygen radicals followed by endothelial cell damage, causing disorders in the microcirculation of the liver tissue leading to alterations in hepatic tissue oxygenation [118].

However, minimizing the detrimental effects of ischemia-reperfusion injury could raise the number of successful patients that may undergo transplantation. Maintenance of adequate hepatic blood flow and sufficient hepatic oxygenation is one of the most vital components in hepatic surgical success. As liver function depends greatly on hemodynamics and viability of liver tissue, measurements of concentrations of oxygenated hemoglobin C_{HbO}, deoxygenated hemoglobin C_{HbR}, total hemoglobin C_{HbT}, and tissue oxygen saturation StO_2 in hepatic tissue have been demonstrated to associate significantly with microcirculatory liver failure induced

by ischemia-reperfusion injury [61]. In chapter 3 and 4, we evaluated the optical properties such as reduced scattering coefficient μ_s', absorption coefficient μ_a, tissue oxygen saturation StO_2, and the oxidation of heme aa_3 in CcO of *in vivo* liver tissue during ischemia and reperfusion provoked by portal triad occlusion using reflectance fiber probe based diffuse reflectance spectroscopy (DRS) [114,125]. Reflectance fiber probe based spectroscopic technique provides average information of optical properties of biological tissues obtained from the point measurement. Optical imaging with digital RGB color camera is a advantageous device for approaching DRS to spatial mapping of chromophore concentrations as well as StO_2 of *in vivo* biological tissues. Diffuse reflectance spectrum of *in vivo* liver reveals the optical absorption spectra of chromophores like oxyhemoglobin, deoxyhemoglobin and cytochrome c oxidase, which depends on the chromophore concentrations in hepatic tissue. Since hemoglobin is the predominant absorber of liver tissue, the severity of liver ischemia-reperfusion can be truly estimated by evaluating the alterations in C_{HbO}, C_{HbR}, C_{HbT}, and StO_2. Accordingly, it is hypothesized that ischemia-reperfusion driven changes in chromophore concentrations and tissue oxygen saturation are associated with spatial inhomogeneity in perfusion of liver lobule which ultimately alters the hemodynamics in liver tissue. Experiment in this chapter was performed to assess this hypothesis through spatial mapping in C_{HbO}, C_{HbR}, C_{HbT}, StO_2, and b using RGB imaging system. The ability of RGB color imaging to assess the hemodynamic responses and tissue morphology following hepatic ischemia-reperfusion would provide important diagnostic information to the extent of ischemia-reperfusion injury resulting from liver transplantation or resection surgery. The technique of diffuse reflectance imaging introduced by Nishidate et al. [126, 127, 128] would provide an insight for studying the rat liver hemodynamics and tissue morphology as a result of hepatic ischemia-reperfusion. Imaging with digital RGB camera is one of the extensively adopted methodfor the non-invasive characterization of

biological tissues where the contrast is achieved from the absorption of light by the hemoglobin in blood. This can be achieved by an RGB CCD camera and a white light source, which is very simple to implement [126, 127]. Moreover, this technique is straightforward in its specific clinical applications and can be implemented with relatively inexpensive instrumentation. Therefore, a simple method that provides sequential spatially resolved images of C_{HbO}, C_{HbR}, C_{HbT}, StO_2, and b would aid in experimental studies of hepatic hemodynamics and tissue morphology resulted from ischemia-reperfusion. Chapter 5 evaluates the reliability of this method of measuring C_{HbO}, C_{HbR}, C_{HbT}, StO_2, and b in rat liver under conditions of ischemia, reperfusion, and post-mortem. The RGB imaging technique has been used to image optical properties of *in vivo* rat brain tissue [127] and human skin [126]. In this chapter, this method is applied to imaging hemodynamics of liver tissue during pathophysiologic events such as hepatic inflow occlusion and subsequent reperfusion. Therefore, a method is proposed to visualize the concentration of oxyhemoglobin, deoxyhemoglobin, total hemoglobin, tissue oxygen saturation and scattering power in the liver tissue applying a digital RGB image. In the proposed technique the RGB values are transformed into the tristimulus values in the Commission Internationale de l' Eclairage XYZ (CIEXYZ) color space, which is consisted with the common RGB working space of the National Television Standard Committee (NTSC), the standard RGB (sRGB) etc. A Monte Carlo simulation (MCS) model of light transport for the liver tissue is adopted to specify the relationship among the tristimulus values and the concentrations of oxyhemoglobin, deoxyhemoglobin and scattering power b described in section 5.2. Images of total hemoglobin concentration and tissue oxygen saturation are reconstructed from the results of oxyhemoglobin and deoxyhemoglobin concentrations. The results of hemodynamic parameters and scattering power are demonstrated in section 5.4. Hemodynamic responses of liver tissue following ischemia-reperfusion are discussed in section 5.5.

5.2. Principle

5.2.1 Relationship between RBG values and diffuse reflectance spectrum

RGB values of a pixel of liver tissue image acquired by a digital camera can be expressed as

$$\begin{bmatrix} \mathrm{R} \\ \mathrm{G} \\ \mathrm{B} \end{bmatrix}^T = \mathrm{N}_1 \begin{bmatrix} X \\ Y \\ Z \end{bmatrix}^T, \tag{5.2}$$

Where N_1 is a transposition matrix to convert *XYZ* values to corresponding RGB values and $[\cdots]^T$ represents transposition of a vector. We approximated the matrix N_1 on the basis of measurements of a standard color chart (colorChecker, X-Rite Incorporated, Michigan) that has 24 color chips and is given with data providing the CIEXYZ values for each chip under specific illuminations and the corresponding reflectance spectra.

X, *Y*, and *Z* in the above equation are the tristimulus values in the CIEXYZ color system and are expressed as

$$X = k\sum E(\lambda)\bar{x}(\lambda)O(\lambda), \tag{5.3}$$

$$Y = k\sum E(\lambda)\bar{y}(\lambda)O(\lambda), \tag{5.4}$$

$$\text{and } Z = k\sum E(\lambda)\bar{z}(\lambda)O(\lambda). \tag{5.5}$$

Furthermore, λ, $E(\lambda)$, and $O(\lambda)$ are the wavelengths, the spectral distribution of the illuminant, and the diffuse reflectance spectrum of liver tissue, correspondingly, whereas $\bar{x}(\lambda)$, $\bar{y}(\lambda)$, and $\bar{z}(\lambda)$ are the color matching functions in the CIEXYZ color system.

The values of constant *k* that results in *Y* being equal to 100 for the perfect diffuser is defined by

$$k = 100/\sum E(\lambda)\bar{y}(\lambda). \tag{5.6}$$

In equation (5.3)-(5.5) the summation can be conducted applying data at 10 nm intervals, from 400 to 700 nm. Considering a single layered liver tissue containing oxyhemoglobin and deoxyhemoglobin, the diffuse reflectance of liver tissue O could be defined as

$$O = I / I_0 = \int_0^{\infty} P(\mu_s', l) \exp[-(\mu_{a,HbO} + \mu_{a,HbR})l] dl. \tag{5.7}$$

Where I and I_0 are the detected and incident light intensities respectively, $P(\mu_s', l)$ is the path length probability function which relies on the scattering characteristics as well as on the geometry of the measurements, μ_s', μ_a, and l are the scattering coefficient, absorption coefficient, and the photon path length, respectively.

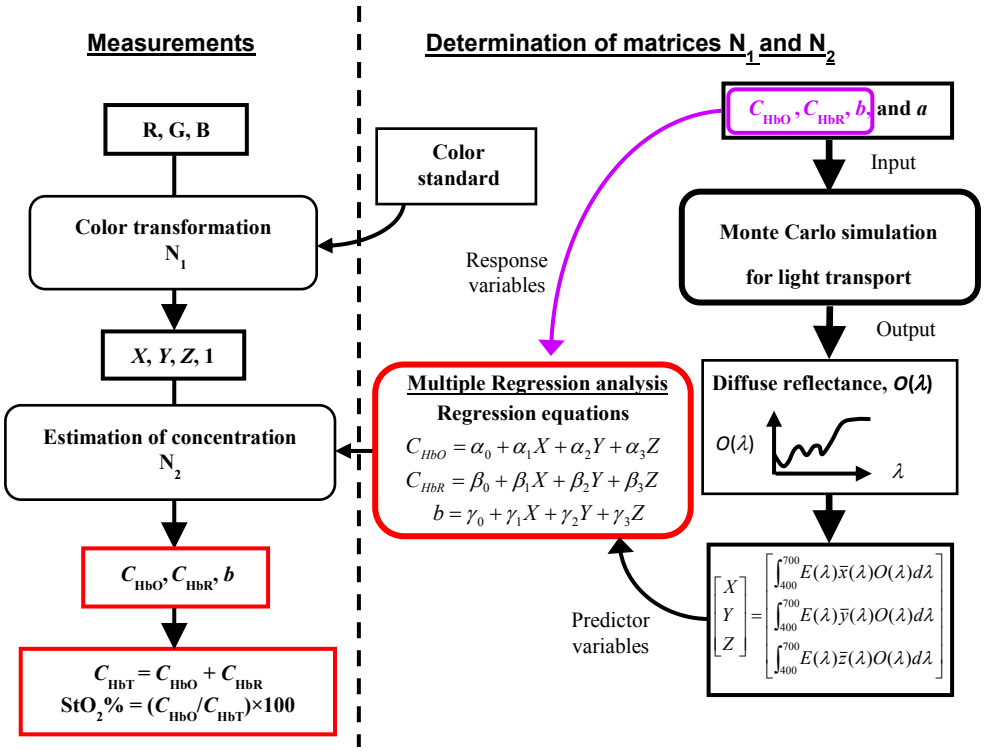

Fig. 5.1. Flow of the estimation process for the concentration of oxyhemoglobin C_{HbO}, deoxyhemoglobin C_{HbR}, total hemoglobin C_{HbT}, tissue oxygen saturation, StO_2, and scattering power, b from the measured RGB values.

In addition, the subscripts *HbO* and *HbR* denote the oxygenated hemoglobin and deoxygenated hemoglobin, respectively. The absorption coefficient, μ_a of each chromophore

can be defined as the output of its concentration C and the extinction coefficient ε, and can be expressed as, $\mu_a = C \times \varepsilon$. Whereas the reduced scattering coefficient, μ_s' can be approximated as power law function in the form of $\mu_s' = a\lambda^{-b}$. Where a is scattering amplitude and b is scattering power. Scattering power b in this case is associated with morphological changes in liver tissue.

Therefore, the RGB values can be approximated as a function of concentration of oxyhemoglobin, C_{HbO}, deoxyhemoglobin C_{HbR}, and scattering power b. Figure 5.1 displays the flow of estimation process applying the proposed method.

At first, the RGB values are converted into X, Y, and Z values by using matrix N_1 with the aid of equation (5.2), then the values of X, Y, and Z are converted into C_{HbO}, C_{HbR} and b by a matrix N_2. However, it is troublesome to estimate the matrix N_2 depending on N_1 and Eqs. (5.3) - (5.6) because $P(\mu_s', l)$ and l for liver tissue are basically unknown. We executed 300 diffuse reflectance spectra in a wavelength range from 400 to 700 nm at intervals of 10 nm by the Monte Carlo simulation (MCS) for light propagation [48], in tissue under various values of C_{HbO}, C_{HbR}, a and b, and then, obtained the corresponding X, Y, and Z values. In this MCS, the combination of absorption coefficient of oxygenated hemoglobin for C_{HbO} and that of deoxygenated hemoglobn for C_{HbR} were input to liver tissue for absorption as $\mu_{a,\,HbO} + \mu_{a,\,HbR}$ [36]. The XYZ-values were then calculated based on the simulated diffuse reflectance spectra. Above calculations were executed for various combination of C_{HbO}, C_{HbR}, a, and b to obtain the data sets of chromophore concentrations and XYZ-values. The multiple regression analysis with 450 data sets established the three regression equations for C_{HbO}, C_{HbR}, and b as

$$C_{HbO} = \alpha_0 + \alpha_1 X + \alpha_2 Y + \alpha_3 Z \tag{5.8}$$

$$C_{HbR} = \beta_0 + \beta_1 X + \beta_2 Y + \beta_3 Z \tag{5.9}$$

$$b = \gamma_0 + \gamma_1 X + \gamma_2 Y + \gamma_3 Z \tag{5.10}$$

The regression coefficients α_i, β_i, and γ_i (i=0, 1, 2, 3) demonstrate the contributions of *XYZ*-values to C_{HbO}, C_{HbR}, and b respectively, and were used as the elements of a 4-by-3 matrix, N_2 as

$$N_2 = \begin{bmatrix} \alpha_0 & \alpha_1 & \alpha_2 & \alpha_3 \\ \beta_0 & \beta_1 & \beta_2 & \beta_3 \\ \gamma_0 & \gamma_1 & \gamma_2 & \gamma_3 \end{bmatrix}. \tag{5.11}$$

Transformation with N_2 from the tristimulus values to the chromophore concentrations and scattering power is thus given by

$$\begin{bmatrix} C_{HbO} \\ C_{HbR} \\ b \end{bmatrix}^T = N_2 \begin{bmatrix} 1 \\ X \\ Y \\ Z \end{bmatrix}^T. \tag{5.12}$$

Once we approximate the matrices N_1 and N_2, images of C_{HbO}, C_{HbR} and b are generated without the MCS. Total hemoglobin concentration image is easily calculated as C_{HbT} = oxyhemoglobin concentration, C_{HbO} + deoxyhemoglobin concentration, C_{HbR} and tissue oxygen saturation of hemoglobin as StO_2% = (oxyhemoglobin concentration, C_{HbO}/total hemoglobin concentration, C_{HbT}) × 100.

5.3. Materials and Methods

5.3.1 Measurement apparatus

The instrument developed for the RGB imaging system is illustrated in fig. 5.2. A white-light emitting diode (LED) (LA-HDF158A, Hayashi Watch Works Co., Ltd., Tokyo, Japan) irradiated the surface of the exposed rat liver tissue by means of a light guide and a ring-shaped illuminator with a polarizer. The light source covered a range from 400 nm to 780 nm. Diffusely reflected light, which contains information of liver tissue optical properties, was recorded by a 24-bit RGB CCD camera (DFK-31BF03.H Imaging source LLC, Charlotte,

NC, USA) without an infrared (IR) cut filter through an analyzer and a camera lens to obtain an RGB image of 640×480 pixels. The ring shaped polarizer and analyzer were positioned in a crossed Nicols alignment with a view to reduce specular reflection of light from the liver surface. A standard white diffuser with 99% reflectance (SRS-99-020, Labsphere Incorporated, New Hampshire) was applied to regulate the white balance of the camera, to correct instrument to instrument differences in output of the camera, and to correct the spatial nonuniformity of illumination. The field of view of the imaging system was 4.22 mm × 3.17 mm. The lateral resolution of the images was calculated to be 0.0066 mm. The RGB images were then applied to estimate the images of C_{HbO}, C_{HbR}, C_{HbT}, StO_2, and b according to the procedure described above.

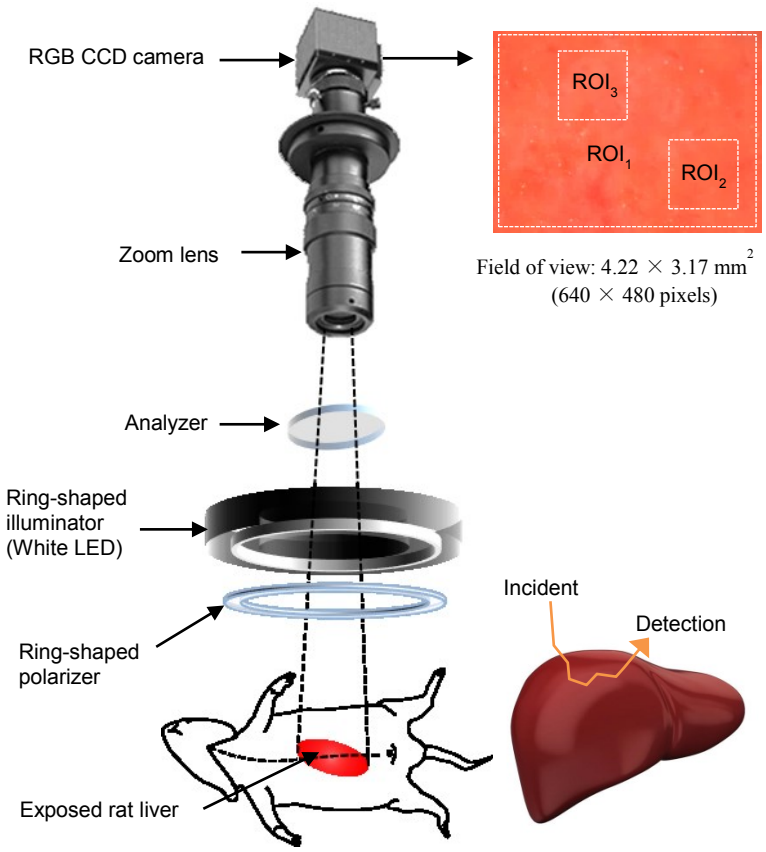

Fig. 5.2. Schematic representation of setup for RGB imaging of hepatic hemodynamics. White LED is employed to illuminate a 4.22 mm × 3.17 mm area of exposed rat liver, which is imaged onto RGB CCD camera. The computer achieves the raw RGB images.

The computation time for analyzing the liver tissue image was 5 s. The regression model represented in the present chapter is based on the results of Monte Carlo simulation. A Monte Carlo method was employed to derive the theoretical diffuse reflectance spectra, and to define the relationship between the measured reflectance and the optical properties of the rat liver. A set of theoretical tristimulus values in the CIEXYZ color system, *X*, *Y*, and *Z*, were executed based on the diffuse reflectance spectrum, the spectral distribution of the illuminant, and color matching functions depending on Eqs. (5.3)-(5.5). Where, the color matching functions correspond to the output of transmittance spectra of RGB color filters and the spectral sensitivity of the CCD. RGB values are calculated from the theoretical XYZ values using the color transformation matrix N_1 in Eq. (5.2).

5.3.2 Experiments

Male Wister rats (*n*=5) weighing from 300 to 474 g were used for the experiment. All experimental procedures were conducted according to the protocols approved by the Animal Care Committee of Tokyo University of Agriculture and Technology. Anesthesia of rats was performed with α-chloralose (50 mg/kg) and urethane (600 mg/kg) by intraperitoneal injection. A rat liver ischemic model was depicted in Fig. 5.3. On laparotomy, the ligamentous attachments from the liver to the diaphragm and abdominal wall were dissected in order to mobilize the liver lobes. Hepatic ischemia was evoked by clamping the portal triad (the hepatic artery, the portal vein, and the bile duct) supplying the median lobes and left lateral lobe without occluding the caudate lobe. The ischemic period of 10 minutes was followed by reperfusion for a period of 120 minutes. After 120 minutes of reperfusion, anoxic condition was induced by nitrogen breathing. The liver surface was moistened with saline and covered with cover glass to prevent evaporation and the influence of the ambient air, and to reduce the surface reflection. Imaging was started before induction of ischemia to record the baseline values and continued during ischemia, reperfusion and post mortem. Measurements

of RGB color images were performed for a total of 160 min at every 5 sec: oxygen breathing for 5 min, normal air breathing for 5 min, ischemia for 10 min, reperfusion for 120 min, and nitrogen breathing for 20 min.

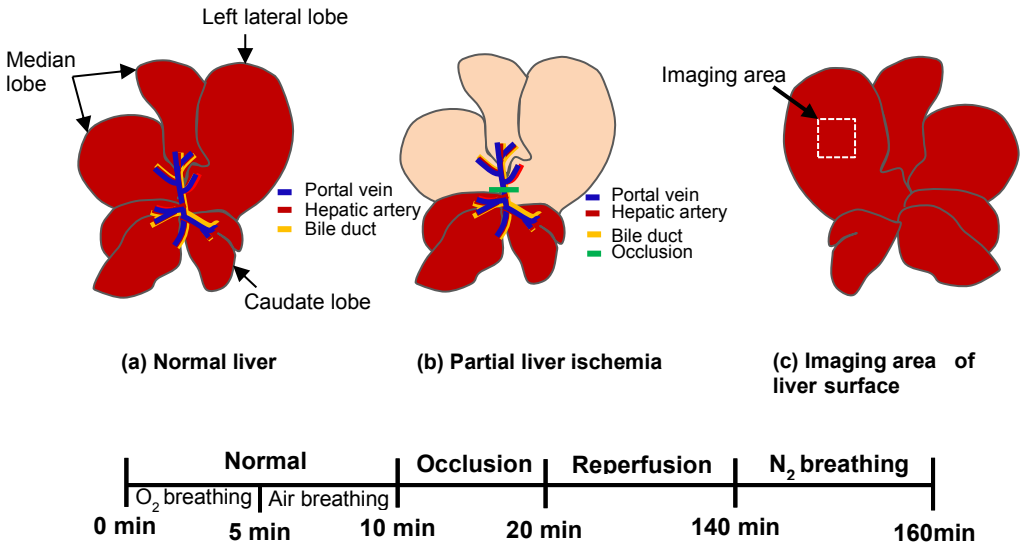

Fig. 5.3. Drawing illustrating the (a) ventral surface of normal rat liver where the left lateral and median lobes have been reflected back to visualize the portal vein (blue), hepatic artery (red), and common bile duct (yellow), (b) Occlusion of portal triad (green) initiates ischemia to the left lateral and median lobes of the liver, and (c) The dorsal surface of the liver lobe is depicted for imaging area.

Estimation of concentrations of oxygenated hemoglobin C_{HbO}, deoxygenated hemoglobin C_{HbR}, total hemoglobin C_{HbT}, tissue oxygen saturation StO_2, and scattering power b in hepatic tissue was carried out depending on the process described above. A region of interest (ROI_1) of 640×480 pixels (entire image), ROI_2 of 150×150 pixels (relatively homogeneous region of perfusion), and ROI_3 of 150×150 pixels (relatively heterogeneous region of perfusion) were set in each image for the analysis of time courses in C_{HbO}, C_{HbR}, C_{HbT}, StO_2, and b. Data are expressed as mean ± SD. An unpaired t-test was carried out in order to compare the average values of C_{HbO}, C_{HbR}, C_{HbT}, StO_2, and b in five rats between the air breathing phase with the

other phases (oxygen breathing, ischemia, reperfusion, and post-mortem), and a $P<0.05$ was considered to be statistically significant.

5.4. Results

Figure 5.4 represents the actual *in vivo* consequences obtained from the liver tissue for RGB image, C_{HbO}, C_{HbR}, C_{HbT}, StO_2, and scattering power b images before ischemia (oxygen breathing, air breathing), during ischemia, reperfusion, and post-mortem respectively. C_{HbO}, C_{HbR}, C_{HbT}, and StO_2 of the normal liver tissue (oxygen breathing and air breathing state) revealed high level of oxyhemoglobin concentration and tissue oxygen saturation. The large increase in C_{HbR}, and decrease in C_{HbO} and StO_2 typically observed in ischemia, which is consistent with the changes in time courses in StO_2 of our previous reports [114,125]. Successive images recorded at 5-min of post-reperfusion demonstrate the spatial alterations in C_{HbO} and StO_2 designated by white arrow on the less perfused portion of the imaged area which is accompanied with scattered hepatic lobular perfusion. Immediately after reperfusion, a slight increase in C_{HbO}, and StO_2 in the imaged area possibly indicating the gradual compensation of hepatic blood flow. In addition, changes in C_{HbO}, C_{HbR}, C_{HbT}, and StO_2 at 2-min and 5-min after onset of nitrogen breathing was also observed and found a rapid increase in C_{HbR} and C_{HbT} of post-mortem liver tissue. The image of scattering power b, acquired at 2-min after onset of nitrogen breathing demonstrated a lower value compare to the reperfusion phase followed by a subsequent increase at 5-min after onset of nitrogen breathing (shown in fig. 5.4) are indicative of changes in average size of scatterers induced by anoxia. The tendency of changes in C_{HbO}, C_{HbR}, C_{HbT}, StO_2, and b following ischemia, reperfusion and post-mortem shown in fig. 5.4 were evident in all five rats.

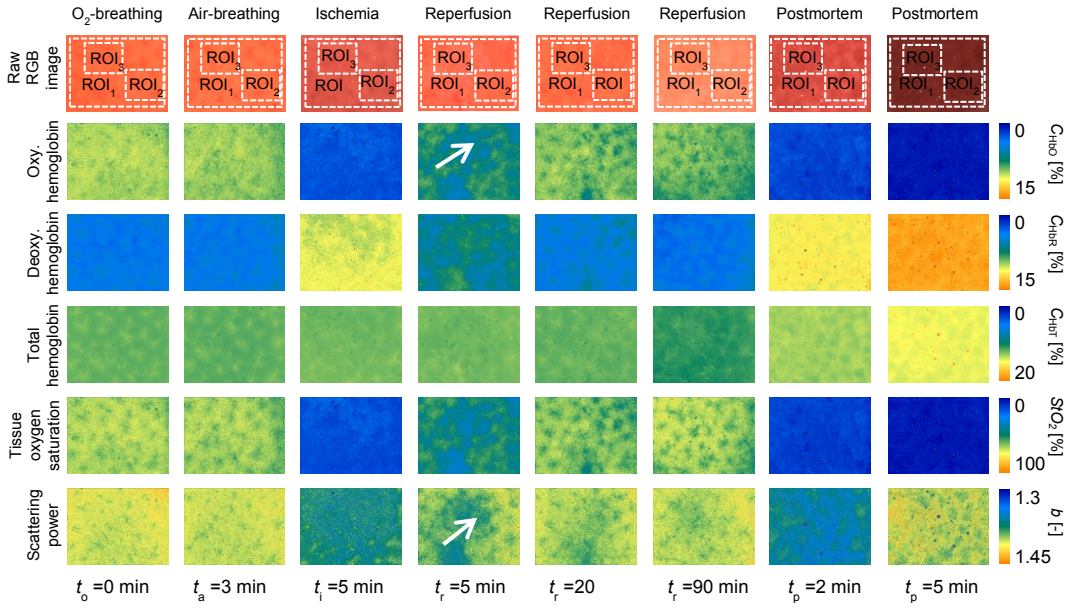

Fig. 5.4. Typical images of *in vivo* liver tissue at different time points of measurements (left to right: The first column shows typical images under oxygen breathing, second shows images under air breathing, third one shows images under ischemic condition, fourth reveals images at 5-min of post-reperfusion, fifth column for images at 20-min of post reperfusion, sixth recorded at 90-min of post-reperfusion, seventh is at 2-min after onset of nitrogen breathing, and finally eighth is at 5-min after initiation of anoxia) (top to bottom: Raw RGB images, and the corresponding C_{HbO}, C_{HbR}, C_{HbT}, StO_2 and scattering power b images reconstructed from the RGB images) under white light illumination. The white boxes in RGB images indicate region of interest (ROI_s) for the time courses.

Time courses of the changes in C_{HbO}, C_{HbR}, C_{HbT}, and StO_2 averaged over the samples and over the entire imaged area (region of interest, ROI_1), relatively homogeneous region (region of interest, ROI_2), and relatively heterogeneous region (region of interest, ROI_3) indicated in fig. 5.4 at the time courses of pre-ischemia (oxygen breathing and air breathing), ischemia, reperfusion, and post-mortem are plotted in Fig. 5.5, 5.6, and 5.7, respectively. Error bar indicates the standard deviation over the five samples.

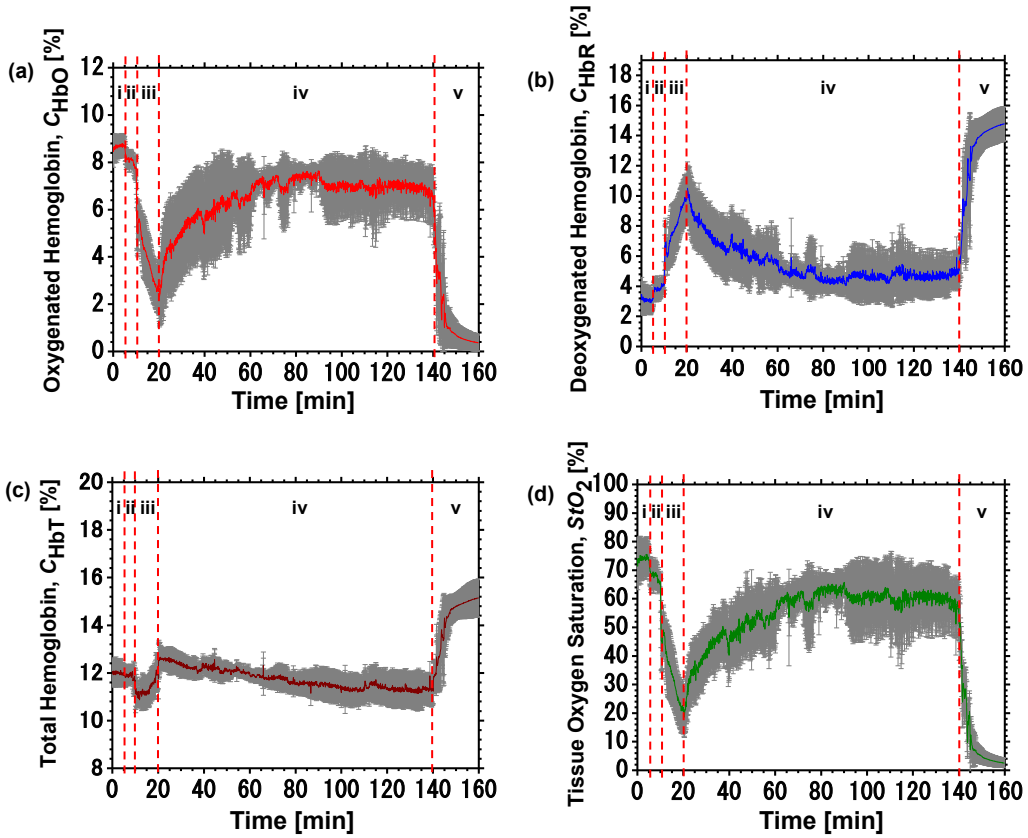

Fig. 5.5. Typical time courses of chromophore concentrations and tissue oxygen saturation averaged over five samples and averaged over the region of interest (ROI_1 for entire image) for (a) Oxygenated hemoglobin, C_{HbO}, (b) Deoxygenated hemoglobin, C_{HbR}, (c) Total hemoglobin, C_{HbT}, and (d) Tissue oxygen saturation, StO_2. Error bars represent the standard deviation (n=5). The symbols i, ii, iii, iv, and v in each figure indicate O_2-breathing, air-breathing, ischemia under air-breathing, reperfusion under air-breathing, and post-mortem, respectively.

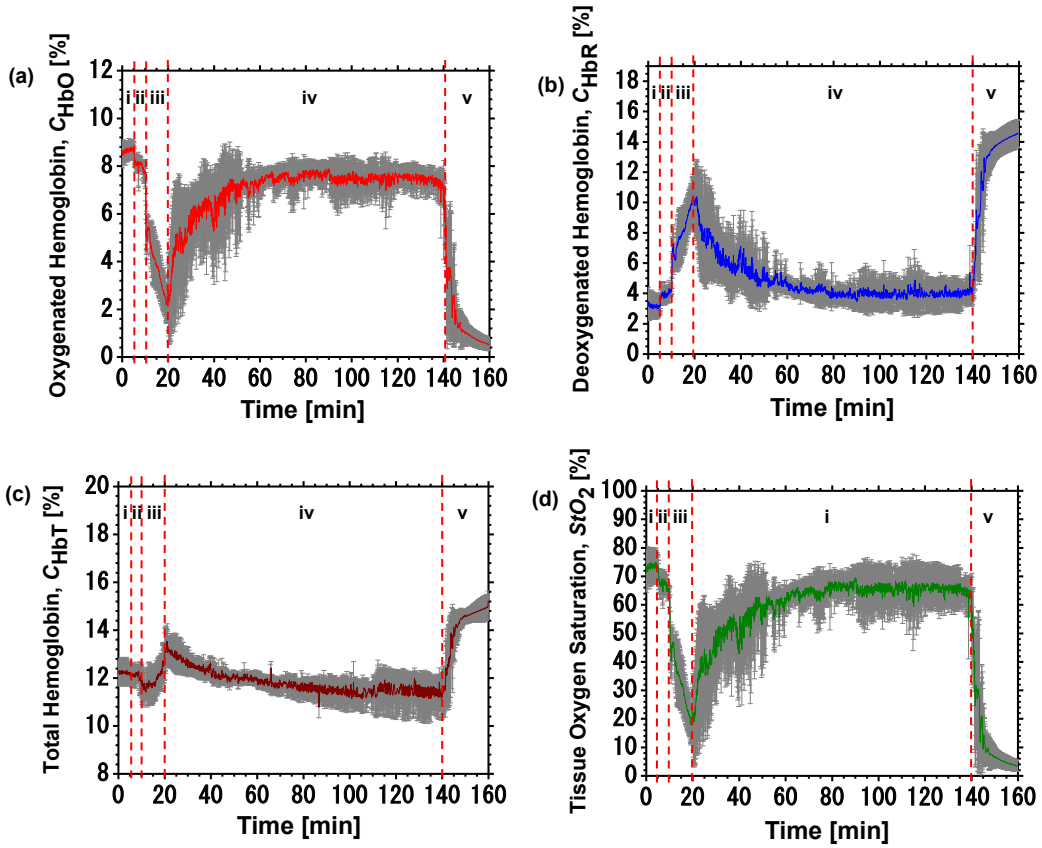

Fig. 5.6. Typical time courses of chromophore concentrations and tissue oxygen saturation averaged over five samples and averaged over the region of interest (ROI_2 for relatively homogeneous region of perfusion) for (a) Oxygenated hemoglobin, C_{HbO}, (b) Deoxygenated hemoglobin, C_{HbR}, (c) Total hemoglobin, C_{HbT}, and (d) Tissue oxygen saturation, StO_2. Error bars represent the standard deviation (n=5). The symbols i, ii, iii, iv, and v in each figure indicate O_2-breathing, air-breathing, ischemia under air-breathing, reperfusion under air-breathing, and post-mortem, respectively.

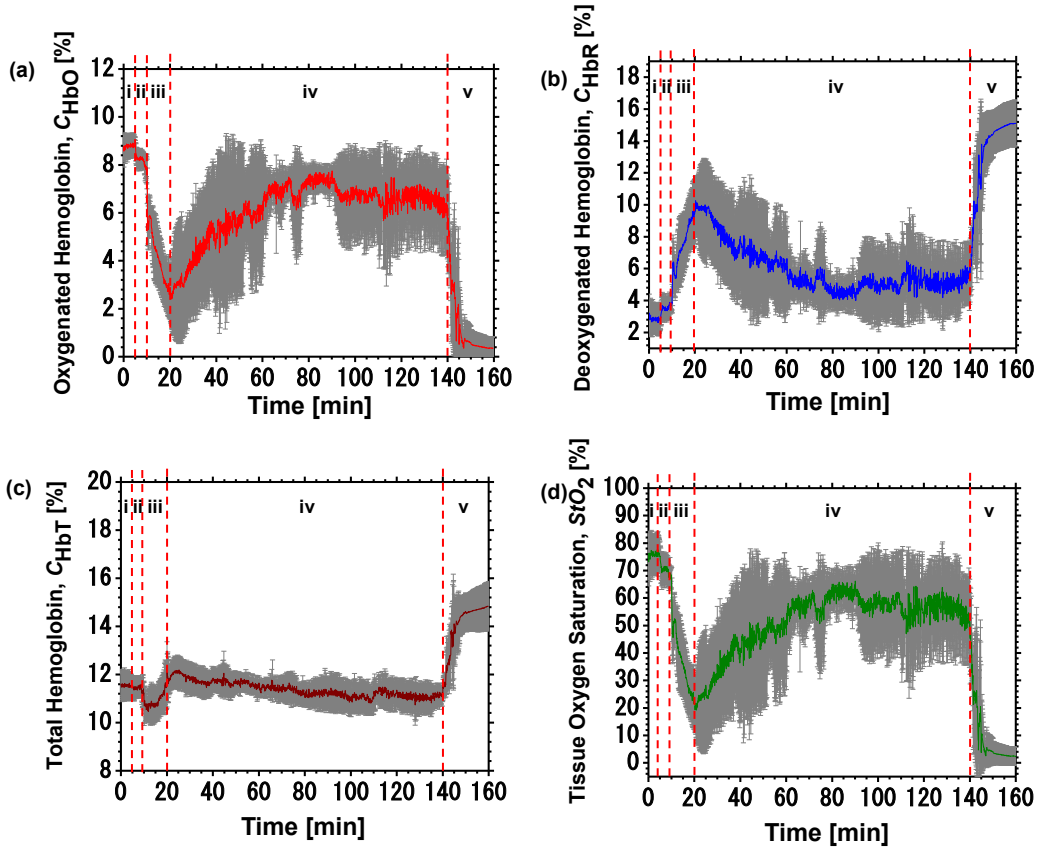

Fig. 5.7. Typical time courses of chromophore concentrations and tissue oxygen saturation averaged over five samples and averaged over the region of interest (ROI_3 for relatively heterogeneous region of perfusion) for (a) Oxygenated hemoglobin, C_{HbO}, (b) Deoxygenated hemoglobin, C_{HbR}, (c) Total hemoglobin, C_{HbT}, and (d) Tissue oxygen saturation, StO_2. Error bars represent the standard deviation (n=5). The symbols i, ii, iii, iv, and v in each figure indicate O_2-breathing, air-breathing, ischemia under air-breathing, reperfusion under air-breathing, and post-mortem, respectively.

Histograms of average values of concentrations of oxyhemoglobin C_{HbO}, deoxyhemoglobin C_{HbR}, total hemoglobin C_{HbT}, and tissue oxygen saturation StO_2, averaged over five samples over ROI_1, ROI_2, and ROI_3 are averaged over each time course and are shown in fig. 5.8, 5.9, and 5.10, respectively.

Whereas the average values of C_{HbO}, C_{HbR}, C_{HbT}, and StO_2 over each period and over ROI_1, ROI_2, and ROI_3 are compiled in table 5.1, table 5.2, and table 5.3, respectively.

Table 5.1. Concentration of oxyhemoglobin C_{HbO}, deoxyhemoglobin C_{HbR}, total hemoglobin C_{HbT}, and tissue oxygen saturation, StO_2 (for ROI_1 shown in fig. 4) of *in vivo* rat liver averaged over the time course of oxygen breathing, air breathing, ischemia, reperfusion, and post-mortem. Results are showed as mean ± SD for 5 rats. Unpaired *t*-test explained the significant differences among the air breathing phase with the other phases. *$P < 0.05$.

Parameters	O_2 breathing	Air breathing	Ischemia	Reperfusion	N_2 breathing
C_{HbO} [Vol. %]	8.67±0.06 *	8.08±0.19	4.02±1.07 *	6.55±0.92 *	1.33±1.41 *
C_{HbR} [Vol. %]	3.09±0.09 *	3.82±0.20	7.95±1.27 *	5.40±1.22 *	12.96±2.40 *
C_{HbT} [Vol. %]	11.99±0.05 *	11.87±0.10	11.36±0.31 *	11.74±0.40 *	14.30±1.01 *
StO_2 [%]	74.09±0.70 *	68.12±1.68	34.19±9.48 *	55.48±8.72 *	10.50±12.22*

Table 5.2. Concentration of oxyhemoglobin C_{HbO}, deoxyhemoglobin C_{HbR}, total hemoglobin C_{HbT}, and tissue oxygen saturation, StO_2 (for ROI_2 shown in fig. 4) of *in vivo* rat liver averaged over the time courses of oxygen breathing, air breathing, ischemia, reperfusion, and post-mortem. Results are shown as mean ± SD for 5 rats. Unpaired *t*-test explained the significant differences between the air breathing phase with the other phases. *$P < 0.05$.

Parameters	O_2 breathing	Air breathing	Ischemia	Reperfusion	N_2 breathing
C_{HbO} [Vol. %]	8.65±0.07 *	8.04±0.21	3.88±1.12 *	7.05±0.93 *	1.59±1.41 *
C_{HbR} [Vol. %]	3.15±0.10 *	3.92±0.23	8.18±1.32 *	4.71±1.26 *	12.60±2.53 *
C_{HbT} [Vol. %]	12.22±0.05 *	12.10±0.11	11.92±0.33 *	11.81±0.47 *	14.37±1.03 *
StO_2 [%]	73.59±0.72 *	67.36±1.87	32.68±9.74 *	60.52±8.99 *	12.21±12.48*

Table 5.3. Concentration of oxyhemoglobin C_{HbO}, deoxyhemoglobin C_{HbR}, total hemoglobin C_{HbT}, and tissue oxygen saturation, StO_2 (for ROI_3 represented in fig. 4) of *in vivo* rat liver averaged over the time courses of oxygen breathing, air breathing, ischemia, reperfusion, and post-mortem. Results are shown as mean ± SD for 5 rats. Unpaired *t*-test explained the significant differences between the air breathing phase with the other phases. *$P < 0.05$.

Parameters	O_2 breathing	Air breathing	Ischemia	Reperfusion	N_2 breathing
C_{HbO} [Vol. %]	8.79±0.06 *	8.20±0.20	4.21±1.11 *	6.14±1.18 *	1.10±1.24 *
C_{HbR} [Vol. %]	2.83±0.10 *	3.54±0.19	7.56±1.34 *	5.92±1.46 *	13.40±2.32 *
C_{HbT} [Vol. %]	11.53±0.05 *	11.41±0.10	10.92±0.29 *	11.38±0.31	14.06±0.98 *
StO_2 [%]	75.98±0.78 *	70.03±1.68	36.46±10.04 *	51.59±10.53*	8.74±10.59 *

In this study oxygenated and deoxygenated hemoglobin concentrations have been used as indexes of total hemoglobin concentration and tissue oxygenation. From the time series evaluations we found that C_{HbO} and C_{HbR} declined and raised respectively following onset of ischemia compared to the preischemic level, consequently the StO_2 decreased which reflect reduced blood flow and oxygen supply to the tissue. Ligation of hepatic pedicle of the median and left lateral lobes resulted in approximately 70% occlusion or ischemia of the liver [61], as indicated by a rapid decrease of hepatic StO_2, on initiation of ischemia. Note that the decrease in C_{HbT} found at ischemia possibly due to hepatic inflow occlusion and keeping the outflow. Hepatic tissue oxygen saturation during oxygen breathing and air breathing (baseline) averaged on five samples over the entire region of image (ROI_1) were estimated to be 74.09±0.70% and 68.12±1.68%, respectively which is compatible with or slightly than that hepatic hemoglobin oxygen saturation, 57.4%±2.5% (n=7) of rabbit calculated at room air [60]. Immediately after reflow of the portal triad, hepatic StO_2 showed remarkably heterogeneous distribution with an average of 55.48±8.72% at ROI_1, after 120 min of reperfusion but did not return to the baseline level. Average StO_2 level at the end of reperfusion for a relatively homogeneous region of interest (ROI_2) is recorded to be 60.52±8.99% which is relatively higher than that recorded from the entire imaged area (ROI_1). Whereas, hepatic tissue oxygen saturation averaged from relatively heterogeneous region of interest (ROI_3) showed lower reperfusion level in comparison to that are recorded from the

entire image (ROI_1) and from relatively homogeneous region of interest (ROI_2) of all five rats. The low hepatic StO_2 is possibly associated with the heterogeneity of sinusoidal length in rat liver, creating heterogeneity in hepatic blood flow [129]. In contrast, C_{HbR} calculated from ROI_1, ROI_2 and ROI_3 increased significantly during ischemia probably due to tissue extraction of oxygen from hemoglobin and slowly decreased with the time courses of reperfusion. It is also interesting to note that immediately after respiratory arrest, C_{HbO} and C_{HbR} declined and raised respectively, therefore the value of StO_2 dropped sharply compare to the reperfusion level. The time courses between the onset of nitrogen breathing and the occurrence of respiratory arrest averaged over all five samples was recorded to be 144±70.92 sec. Total hemoglobin concentration C_{HbT}, started to increase after onset of nitrogen breathing and reached a maximum level immediately after respiratory arrest which may be associated with high venous or intrahepatic blood pressure during the first few minutes of asphyxia and may persists for hours after death [93]. Time periods of C_{HbO}, C_{HbR}, C_{HbT}, and StO_2 over the ROI_s (depicted in fig. 5.5, 5.6, and 5.7) revealed that the hemodynamics response of liver tissue associated with ischemia-reperfusion is characterized by a significant decrease in C_{HbO} and StO_2 with the onset of ischemia compared to the preischemic level. Additionally, subsequent reperfusion resulted in gradual increase in C_{HbO} and StO_2 with simultaneous decrease in C_{HbR} related to the ischemic level. The time courses of C_{HbO}, C_{HbR}, C_{HbT}, and StO_2 during hepatic inflow occlusion and on subsequent reflow are consistent with the hemodynamic responses of hepatic ischemia-reperfusion.

Histograms 5.8, 5.9, and 5.10 illustrate the averages of time series for C_{HbO}, C_{HbR}, C_{HbT}, and StO_2 over the time courses of oxygen breathing, air breathing, ischemia, reperfusion and post-mortem averaged over the region of interest ROI_1, ROI_2 and ROI_3, respectively for all five samples.

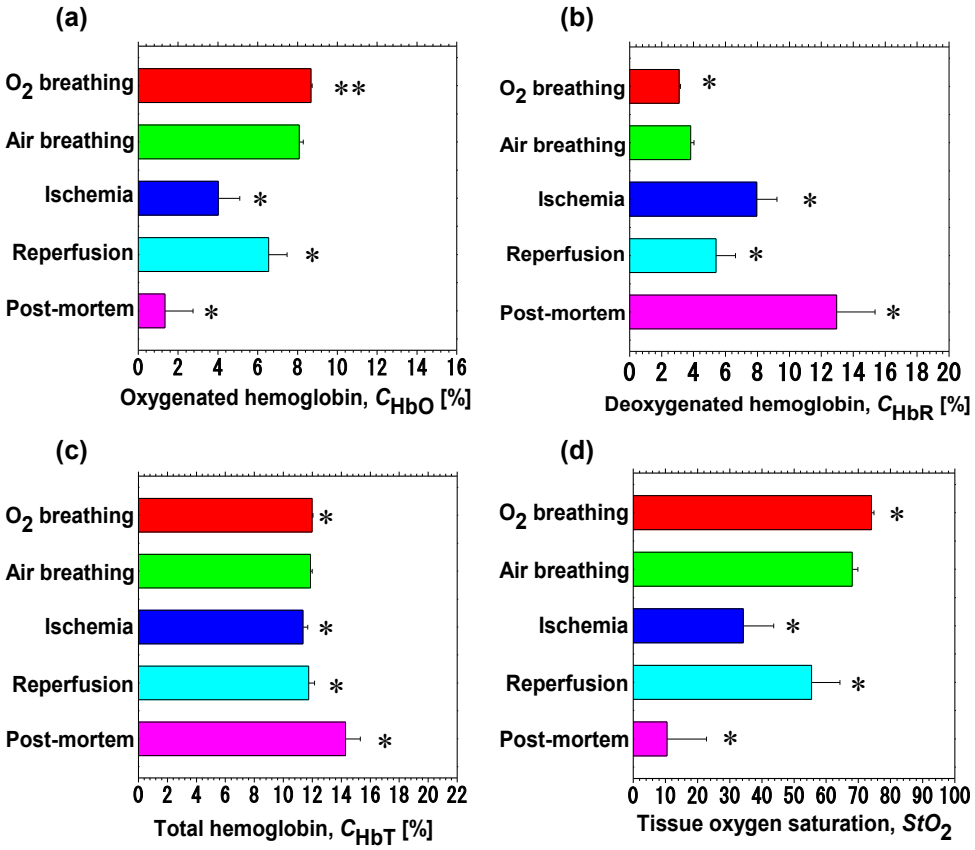

Fig. 5.8. Histograms show the average values of chromophore concentrations and tissue oxygen saturation (for ROI_1 shown in fig. 4) averaged over the period of oxygen breathing, air breathing, ischemia, reperfusion and post-mortem in five rats for (a) Oxygenated hemoglobin, C_{HbO}, (b) Deoxygenated hemoglobin, C_{HbR}, (c) Total hemoglobin, C_{HbT}, and (d) Tissue oxygen saturation, StO_2. Data are represented as mean ± SD. Unpaired *t*-test declared the significant differences among the air breathing phase with the other phases. $^*P < 0.05$.

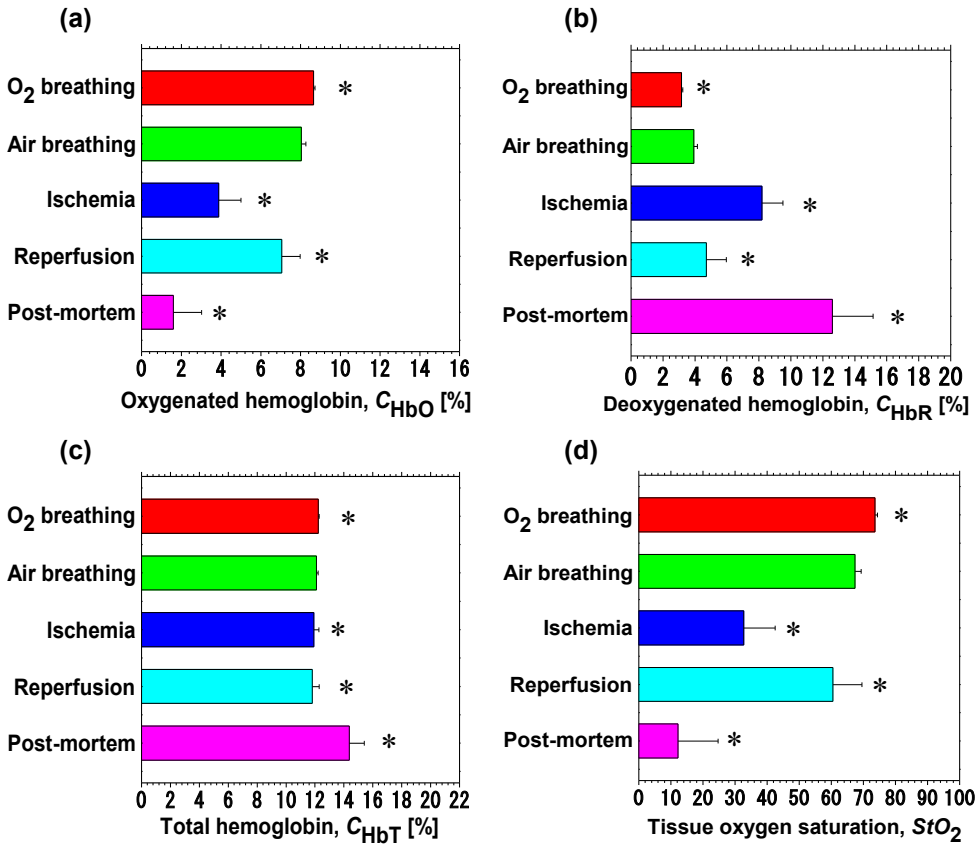

Fig. 5.9. Histograms show the average values of chromophore concentrations and tissue oxygen saturation (for ROI_2 shown in fig. 4) averaged over the period of oxygen breathing, air breathing, ischemia, reperfusion and post-mortem in five rats for (a) Oxygenated hemoglobin, C_{HbO}, (b) Deoxygenated hemoglobin, C_{HbR}, (c) Total hemoglobin, C_{HbT}, and (d) Tissue oxygen saturation, StO_2. Data are represented as mean ± SD. Unpaired *t*-test declared the significant differences among the air breathing phase with the other phases. *$P < 0.05$.

Average oxyhemoglobin concentration was found to be decreased significantly at 10 minutes of ischemia which again gradually improved on reperfusion. Similarly, tissue oxygen saturation dropped sharply following onset of hepatic inflow occlusion. Oxygenated hemoglobin concentration averaged over each period of five samples over the region of interest (ROI_1) was calculated to be 8.67±0.06 at oxygen breathing, 8.08±0.19 at air breathing, 4.02±1.07 at ischemia, 6.55±0.92 at post-reperfusion, and 1.33±1.41 at post-mortem.

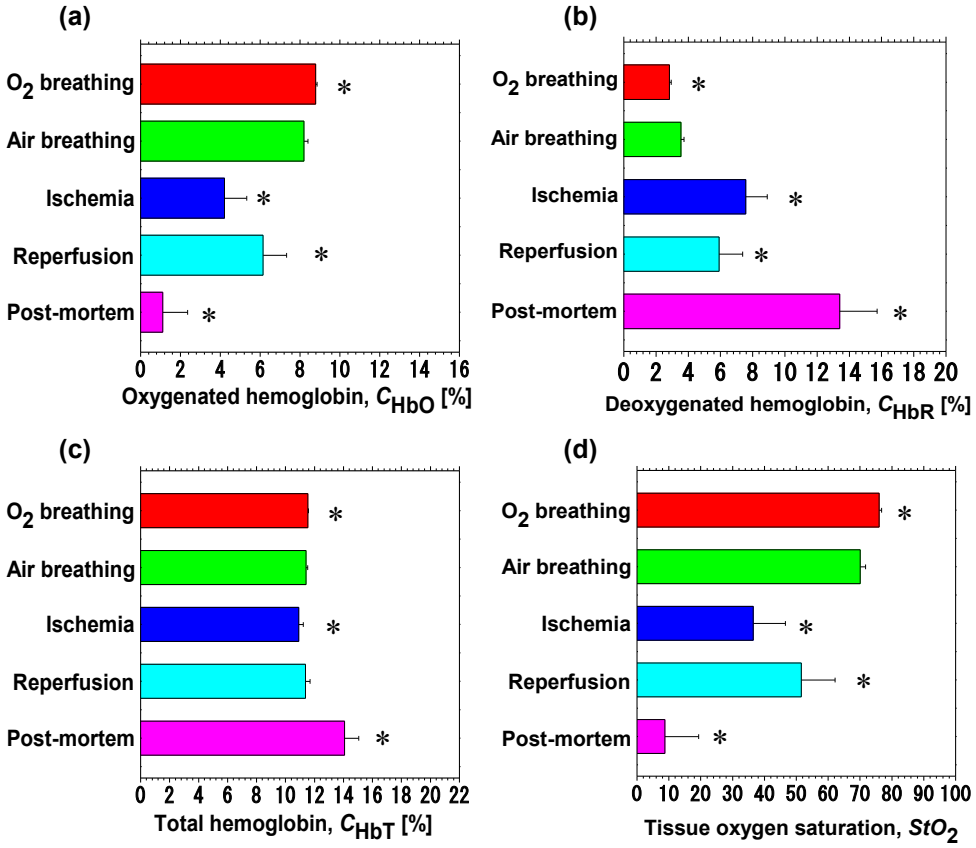

Fig. 5.10. Histograms show the average values of chromophore concentrations and tissue oxygen saturation (for ROI_2 shown in fig. 4) averaged over the period of oxygen breathing, air breathing, ischemia, reperfusion and post-mortem in five rats for (a) Oxygenated hemoglobin, C_{HbO}, (b) Deoxygenated hemoglobin, C_{HbR}, (c) Total hemoglobin, C_{HbT}, and (d) Tissue oxygen saturation, StO_2. Data are as mean ± SD. Unpaired *t*-test declared the significant differences among the air breathing phase with the other phases. *$P < 0.05$.

Whereas, tissue oxygen saturation level of air breathing phase, 68.12±1.68% decreased to a value of 34.19±9.48% at the end of ischemia, while during reperfusion recovered to 55.48±8.72% but not completely reverted to the preischemic level possibly due to ischemia-reperfusion associated hepatic dysfunction.

Changes in the average scattering power, *b* over time for the ROIs of five rats represented in fig. 5.4 are plotted in fig. 5.11. The mean scattering power decreased significantly with ischemia can be described by the rise in the mean size of scatterers. The average value of

scattering power, *b* at reperfusion obtained from the entire image, ROI_1 is comparatively higher than that recorded from the relatively heterogeneous ROI_3 (Fig.5.11). The maximum level of *b* was recorded from the relatively homogeneous region of interest (ROI_2) at the end of reperfusion indicating less ischemia induced damage compare to that occurred in ROI_1 and ROI_3 depicted in fig. 5.12 and are summarized in table 5.4. After onset of nitrogen breathing, a biphasic alteration in scattering power was detected, with an initial decrease in *b*, followed by a progressive increase. Observations from the current study indicate that in addition to significant changes in C_{HbO}, C_{HbR}, C_{HbT}, and StO_2 during hepatic ischemia, Monte Carlo simulation based multiple regression analysis demonstrates alteration in scattering power, *b* that are consistent with the ischemia induced changes in cellular and subcellular structures of hepatic tissue.

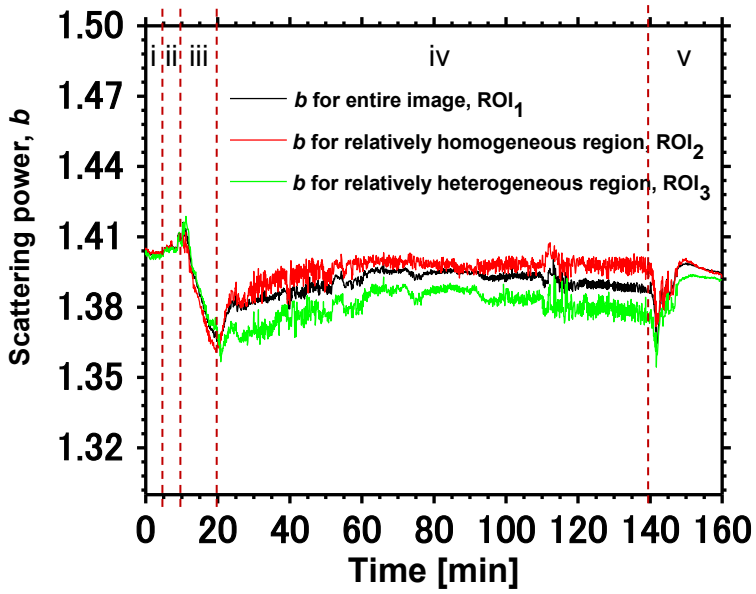

Fig. 5.11. Typical result of time courses in scattering power, *b* averaged over five samples and averaged over the region of interest (ROI_1 for entire image, ROI_2 for relatively homogeneous region of perfusion, and ROI_3 for relatively heterogeneous region of perfusion). Error bars show the standard deviation (n=5). The symbols i, ii, iii, iv, and v in each figure indicate O_2-breathing, air-breathing, ischemia under air-breathing, reperfusion under air-breathing, and post-mortem, respectively.

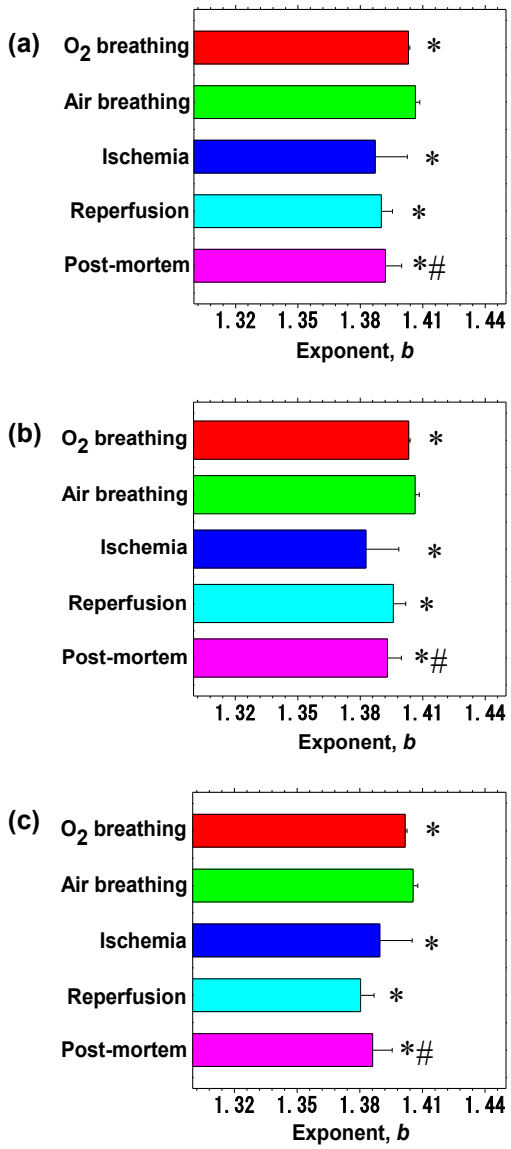

Fig. 5.12. Histograms show the average value of scattering power, *b* averaged over the time course of oxygen breathing, air breathing, ischemia, reperfusion, and post-mortem in five rats for (a) Entire imaged area (ROI_1), (b) Relatively homogeneous region (ROI_2), and (c) Relatively heterogeneous region (ROI_3). Data are represented as mean ± SD. Statistical significant differences are marked: * differences among air breathing phase with the other phases ($P < 0.05$), # difference between reperfusion and post-mortem phase ($P < 0.05$).

Table 5.4. Scattering power, b (for ROI_1, ROI_2, and ROI_3 shown in fig. 4) of in vivo rat liver averaged over the time courses of oxygen breathing, air breathing, ischemia, reperfusion, and post-mortem. Data showed as mean ± SD for 5 rats. Unpaired t-test declared the significant differences. Statistical significant differences are marked: * differences among air breathing

phase with the other phases ($P < 0.05$), # difference reperfusion and post-mortem phase ($P < 0.05$).

Parameters	O_2 breathing	Air breathing	Ischemia	Reperfusion	N_2 breathing
b for ROI_1	1.40±0.00 *	1.41±0.00	1.39±0.02 *	1.39±0.01 *	1.39±0.01 *#
b for ROI_2	1.40±0.00 *	1.41±0.00	1.38±0.02 *	1.40±0.01 *	1.39±0.01 *#
b for ROI_3	1.40±0.00 *	1.41±0.00	1.39±0.02 *	1.38±0.01 *	1.39±0.01 *#

5.5. Discussion

Inthe current chapter a method for light transport in tissue is used to analyze the reflectance spectra of hepatic tissue following ischemia-reperfusion and post-mortem using the RGB imaging instrument. With the RGB imaging technique, it was feasible to estimate images of oxyhemoglobin concentration, deoxyhemoglobin concentration, and scattering power. From these estimated images of oxyhemoglobin and deoxyhemoglobin concentrations, the images of total hemoglobin concentration and tissue oxygen saturation were reestablished.

In chapter 5, the hemodynamic responses of rat liver at the time of ischemia-reperfusion induced by portal triad occlusion was examined. In section 5.4, we have demonstrated that 10 minutes of hepatic ischemia and 120 minutes of reperfusion are associated with disruption of hepatic blood flow with subsequent hemodynamic instability which results in decreased C_{HbO}, C_{HbT}, and StO_2 during ischemia and reperfusion compared to the baseline level. We also observed that during a 120-min period of reperfusion there was a gradual rise in C_{HbO} and StO_2 along with a partial recovery of the initially severely depressed hepatic tissue which is compatible with the hypothesis of no reflow of sinusoids during the early stage of reperfusion, followed by subsequent reflow [99]. Alterations in hepatic microvascular diameter at the time of early phase of reperfusion emerge to be associated in the postischemic reperfusion failure

[99]. The major dysfunction of hepatic ischemia is the lack of re-establishment of nutritive blood flow, which causes hemoconcentration, including endothelial cell swelling, interstitial edema formation, and ultimately alters the microcirculation during reperfusion [130]. Microcirculatory dysfunction is characterized by heterogeneous perfusion of liver lobule observed at the time of early phase of reperfusion indicated by extravasation of erythrocytes, and ultimately petechial bleedings [131].

The combination of a diverse architecture, large size, and low pressure gradient of liver more likely makes the heterogeneous perfusion of the hepatic vascular bed and the distribution of portal blood to different portion of the liver lobes [132]. Furthermore, little differences in hydrostatic pressure could result in large imbalances in the flow of portal blood to different part of the liver at scales ranging from individual sinusoids to entire liver lobes leading to heterogeneity in perfusion [132]. Occlusion of both hepatic artery and portal vein (Pringle maneuver) increased heterogeneity of perfusion compared to perfusion via only portal vein [132] or only hepatic artery [133]. However, we have not observed perfusion failure of entire liver lobules (shown in fig. 4) following 10 minutes of portal triad occlusion, which is in contrast to studies on hepatic microcirculation after a longer period of ischemia (90 min) [134] and reperfusion (3 hours) [135] which is characterized by a noticeable decrease of densely perfused sinusoids associated with increased number of nonperfused liver lobules. Hepatocellular damage due to longer ischemia-reperfusion periods caused by acute cellular injury at 3 to 6 hours of post reperfusion includes the onset of necrosis and apoptosis [135]. The prolongation of both ischemia and reperfusion periods may be the causative factor for the gradual suspension of sinusoids from perfusion also called secondary sinusoidal perfusion failure [132], which ultimately yields a total microcirculatory shutdown of entire liver lobules.

Using RGB imaging of rat liver we have demonstrated that the changes in hemodynamics in liver tissue correlates with the decreased C_{HbO} and StO_2 along with scattered hepatic lobular perfusion, indicating the influence of nutritive perfusion deficiency in the expression of ischemia-reperfusion injury. The result propose that a decrease in hepatic C_{HbO} and StO_2 after reperfusion compared to the baseline level is presumably associated in the mechanism of hepatocellular impairment that results later. Measurement of hepatic tissue oxygen saturation at the time of early phase of reperfusion is important to predict the strength of later liver injury and, ultimately prognosis.

Furthermore, hepatic tissue oxygen saturation StO_2, and hepatic energy state could be the dependable indices of the ischemia-reperfusion liver injury, notably to diagnose the early graft rejection after liver transplantation. The estimated hepatic tissue oxygen saturation depends primarily on the hepatic blood flow, oxygen content of hepatic artery and portal vein, and the hepatic oxygen consumption [113]. Reduced hepatic tissue oxygen saturation was observed at reperfusion compared to the baseline level. The reduced StO_2 reveals the disparity between the oxygen supply and the oxygen demand as StO_2 displays a equity between hepatic oxygen supply and the requirement of oxygen in hepatocytes. Moreover, oxygen requirement in the early stage of reperfusion was showed to be less than in the preischemic time, due to impaired respiratory functions of mitochondria in the hepatocytes after ischemia-reflow process [136] which is implied by a declined reperfusion level of StO_2. The decreased tissue hemoglobin indicates a decrease in local blood volume in the liver proposing that the declined tissue oxygen saturation is for the declined blood flow involved with insufficient oxygen supply. Factors yielding an inequality among hepatic oxygen supply and requirement, effect a corresponding alteration in hepatic venous oxygen saturation, and low oxygen saturation recommend the presence of areas with very low oxygen tension in the liver [137]. Additionally, changes in C_{HbO} during ischemia-reperfusion is indicated by a

significant decrease in C_{HbO} with initiation of ischemia and a gradual increase following reperfusion but lower than the preichemic level. The lower C_{HbO} level of reperfusion phase implies a decline local in regional blood volume in the liver tissue, proposing that the reduced StO_2 is due to reduced blood flow involved with insufficient oxygen supply. The disturbances in tissue oxygen saturation were concurrently caused by an increase in C_{HbR} and a decrease in C_{HbO} due to hepatic inflow occlusion leading to a decrease in total hemoglobin concentration, C_{HbT} during ischemia. The value of C_{HbT} was started to increase on initiation of nitrogen breathing and reached to the maximum level after respiratory arrest, revealing increased intrahepatic blood flow. Decrease in hepatic C_{HbO}, C_{HbT}, and StO_2 during ischemia measured in this chapter were assumedto be largely due to temporary deterioration of hepatic blood supply which then recovered gradually on subsequent reflow. With respect to the decreased hepatic blood flow, it has been demonstrated that in a ischemic model, hepatic blood flow during the early stage of reperfusion is reportedly 30% to 75% of the initial values [136]. Moreover, Clemens et al. [134] showed that the number of perfused sinusoids on the surface of liver lobe was decreased after ischemia and reperfusion, which are consistent with our findings that C_{HbO} and StO_2 after reperfusion remained lower than the baseline value. Decrease in oxygen supply and oxygen demand might develop in the initial stage of reperfusion to the magnitude that insufficient oxygen supply may be dominant factor contributing to decrease in C_{HbO} and StO_2, which in turn lead to local liver hypoxia [118]. However, the exact mechanism related to the reduced C_{HbO} is still not clear; involvement of reperfusion injury might be responsible. It has been suggested that excess production of toxic oxygen free radicals, followed by endothelial cell impairment during reperfusion [138] as well as cell swelling due to ischemia resulted in alteration of hepatic blood flow [139]. Several mechanisms may be proposed to contribute to postischemic reperfusion failure, including sinusoidal endothelial cell swelling with luminal narrowing, intracellular edema

formation, and intravascular hemoconcentration [140]. Certain vasoactive substances, released on reperfusion may lead to vasoconstriction of sinusoids in the liver due to the ischemia-reperfusion process, which results in microcirculatory disturbances. The microcirculatory alterations may cause regional hypoxia in liver tissue, resulting liver impairment. On the basis of our current findings, we assume that hepatic hemoglobin concentrations and tissue oxygen saturation after initiation of reperfusion can be an acceptable symbol of later liver impairment and prognosis in a clinical situation.

On the other hand, the decrease in scattering power, *b* at the time of ischemia and immediately after onset of nitrogen breathing is probably associated with depletion of mitochondrial energy production leading to rounding and swelling of mitochondria, dilatation of the endoplasmic reticulum, and formation of plasma membrane protrusions called *blebs* [141]. Short period of ischemia or anoxia is characterized by a rapid end of *bleb* formation during reoxygenation [141], whereas hepatocyte vacuolation is more evident at 3-4 min after death under an anoxic condition [92,93].

Optical imaging system using RGB color camera described in chapter 5 has the ability to deduce new vision into the spatiotemporal dynamics of hepatic function during ischemia-reperfusion. In addition to broad hemodynamic changes in time courses such as those that occur during ischemia compared to preischemia situation, the RGB camera can also image the spatial changes in hemoglobin concentrations and tissue oxygen saturation during reperfusion. There is a correlation among the time courses of StO_2 recovered during reperfusion obtained by diffuse reflectance spectroscopic technique [114], explained in chapter 3 and 4, and the findings of the current study obtained by RGB imaging method. Thus, the RGB imaging method may be helpful in monitoring the hemodynamics response of liver tissue resulted from ischemia-reflow process. Our obtained data regarding the time

period in C_{HbO}, C_{HbR}, C_{HbT}, and StO_2 are in good accordance with the hemodynamics of liver tissue.

The model of hepatic inflow occlusion by portal triad clamping allows us to evaluate the impact of ischemia and reperfusion of the liver in terms of changes in $C_{HbO,}$ C_{HbR}, C_{HbT}, StO_2, and *b* of *in vivo* exposed liver tissue. Post-ischemic changes were also found in the current study, showing scattered hepatic lobular perfusion during the initial phase of reperfusion. In addition, post-ischemic hyperemic response at the time of initial reperfusion phase [142] due to ischemia and denervation of the liver tissue may be also associated in heterogeneous perfusion of liver lobule along with decreased tissue oxygen saturation level. The heterogeneous distribution of hepatic StO_2 observed immediately after reperfusion of the portal triad is attributable to the heterogeneous distribution of intrahepatic blood flow.

Impaired hepatic blood flow following hepatic ischemia may be a major cause of hepatocellular dysfunction. Changes in hepatic blood flow can motive changes in nutritive blood flow through the hepatic sinusoids and may devoted to the subsequent advancement of hepatocellular injury. It is not clear whether the observed decrease in the blood flow during reperfusion is a primary or secondary event in the pathophysiology of the injury [143]. However, the reduced C_{HbO} and StO_2 during reperfusion may also be a useful indicator of graft function. The results of spatial and temporal changes in $C_{HbO,}$ C_{HbR}, C_{HbT}, StO_2, and *b* following ischemia and reperfusion demonstrated that our method is reliable and reproducible for evaluating the hepatic hemodynamic parameters and tissue morphology. A notable association is found between the hemodynamic parameters measured by RGB imaging technique and the tissue oxygenation parameters (StO_2 and cytochrome c oxidase) measured by reflectance fiber probe based diffuse reflectance spectroscopy [114,125] explained in chapter 3 and 4, which agreed the value of RGB imaging technique in monitoring hepatic tissue perfusion.

5.6. Conclusions

In summary, method is applied using RGB camera to visualize the hemodynamic consequences and tissue morphology of hepatic ischemia-reperfusion in exposed rat liver. By illuminating the surface of rat liver with white LED and recording the resultant RGB images, the images of hemodynamic parameters and scattering power b are reconstructed. Hepatic hemodynamic responses to ischemia-reperfusion were studied in five rats to investigate the time courses and spatial distribution of chromophore concentrations and tissue oxygenation. Our data support the view that hemodynamic changes in rat liver tissue under conditions of hepatic inflow occlusion resulted in ischemic changes of the liver tissue followed by a subsequent recovery during reperfusion. Early reperfusion of liver tissue after 10-min of portal triad occlusion is characterized by heterogeneous perfusion of liver lobule with decreased oxygenated hemoglobin, whereas prolongation of reperfusion period for two hours reduced the spatial inhomogeneity. Ischemia results in a fast increase in C_{HbR} and decrease in C_{HbO} and StO_2 leading to a decrease in C_{HbT} which may be associated with decreased hepatic blood flow. Time course of changes in C_{HbO} are very similar to the time course of changes in StO_2 during ischemia-reperfusion. The results of hepatic ischemia-reperfusion showed the spatial changes in hepatic hemodynamics, an increase in deoxygenated hemoglobin concentration, decrease in oxygenated hemoglobin concentration and tissue oxygen saturation during ischemia which subsequently recovered on reperfusion. Time courses of changes in C_{HbO}, C_{HbR}, C_{HbT}, and StO_2 during hepatic inflow occlusion and on subsequent reflow are agreeable with the hemodynamic responses of hepatic ischemia-reperfusion. The results demonstrated that the imaging method could accurately monitor the changes in hemodynamic parameters resulting from hepatic inflow occlusion and could reflect the ischemia-reperfusion induced hepatic dysfunction after reperfusion. The method presented in this chapter is noninvasive and can be used to evaluate spatial and temporal changes in hepatic

hemodynamic parameters at the same time. As our method can detect ischemia and reperfusion successfully, we believe that simultaneous measurement of spatial and temporal changes in C_{HbO}, C_{HbR}, C_{HbT}, StO_2, and b has great potential for the diagnosis of tissue ischemia and reperfusion. This study shows the potential of RGB imaging to assess hepatic hemodynamics as an indicator of hepatic tissue viability in liver transplantation. We intend to further extend the proposed method to visualize the absorption and scattering properties of liver tissue to investigate the pathophysiological and morphological changes resulting from hepatic ischemia-reperfusion.

Chapter 6

Concluding Remarks

In the current dissertation two main studies have been developed.

Firstly, Single-reflectance-fiber probe based diffuse reflectance spectroscopy is employed for estimating the reduced scattering coefficient, the absorption coefficient, the tissue oxygen saturation, and the reduction of heme *aa*3 of *in vivo* liver tissue. The main goal of the first study was to assess the ability of diffuse reflectance spectroscopy in monitoring the optical properties of liver tissue during ischemia-reperfusion. The results of the first study demonstrate the possible application of the DRS system in assessing the pathophysiological status of *in vivo* liver tissue. The usefulness of the current technique are its simplicity and portability, because the only devices needed are a white light source, fiber optics, and two spectrometers. As the proposed technique can be applied to simultaneously estimate the hemodynamic responses, mitochondrial energy state, and tissue morphology, this technique would be valuable for determing viability of *in vivo* liver tissue.

The principle aim of the second study is to evaluate the potential of RGB imaging system to visualize the changes in hemodynamics parameters such as concentration of oxyhemoglobin, deoxyhemoglobin, total hemoglobin and tissue oxygen saturation, and scattering parameter of *in vivo* liver tissue resulted from ischemia-reperfusion. The results of the second study demonstrated that the RGB imaging technique could accurately monitor the changes in hemodynamic and scattering parameter resulting from hepatic inflow occlusion.

Chapter 2 focused on the description of fundamental theories and principles considered in this dissertation. A review on optical properties of tissue were introduced in section 2.2. The

algorithm of the Monte Carlo simulation for the light transport in tissue has been mentioned in Section 2.4. The spectrocolorimetry and CIE color system have been presented in Section 2.5.

Chapter 3 considered the *in vivo* recordings of diffuse reflectance spectra for exposed rat liver during the ischemia-reperfusion induced by the hepatic portal (hepatic artery, portal vein, and bile duct) occlusion. In this chapter a technique for estimating the reduced scattering coefficient, absorption coefficient, tissue oxygen saturation, and the reduction of heme *aa*3 of *in vivo* liver tissue applying a single-reflectance-fiber probe with two source-collector geometries was investigated. The geometries of reflectance fiber probe system was demonstrated in section 3.2. Multiple regression analysis aided by the Monte Carlo simulation was successfully employed to determine the regression coefficients of oxyhemoglobin and deoxyhemoglobin. With regard to validate the use of $\mu_a(605)/\mu_a(620)$ to demonstrate the redox state of heme aa_3 in CcO of liver tissue, prior experiments with an *in vitro* excised liver sample was carried out. A rat model with ischemia and reperfusion was represented in section 3.3. In section 3.3 and 3.4, the potential of this method was validated by the phantom experiments. The DRS data analysis showed promising results in the use of this technology for diagnosing ischemia-reperfusion injury. Significant changes in both absorption and scattering properties were demonstrated in the results of *in vivo* experiments during ischemia-reperfusion induced by hepatic portal triad occlusion. Changes in $\mu_a(605)/\mu_a(620)$ during ischemia and after euthanasia indicate the reduction in heme *aa*3, an indication of mitochondrial energy failure. Interestingly, the scattering change in the NIR wavelength region after death demonstrates the hepatocyte vacuolation. These promising findings demonstrated the ability of DRS to augment the current clinical application in liver transplantation.

Chapter 4 extended the study demonstrated in chapter 3. A novel algorithm is developed to evaluate the oxidation of heme *aa*3 in cytochrome c oxidase from the regression coefficients of oxidized heme (a_{HmO}) and reduced heme (a_{HmR}) in *in vivo* liver tissue applying a single reflectance fiber probe setup in a more efficient manner. Monte Carlo simulation based multiple regression analysis was carried out to estimate the regression coefficients of a_{HmO} and a_{HmR} for evaluating the oxidation of heme *aa*3 in CcO. Estimation of oxidation of heme *aa*3 described in chapter 4 is different from the ratio metric evaluation documented in chapter 3 in terms of the application of the regression coefficients of a_{HmO} and a_{HmR} obtained from the multiple regression analysis. *In vivo* experimental results presented in section 4.4 showed that DRS was found suitable to measure oxidation of heme aa_3 in cytochrome *in vivo* following ischemia-reperfusion. The results for StO_2 and $OHaa_3$ revealed that the method implemented in the present chapter is feasible and has possible application in the intraoperative evaluation of hepatic tissue oxygenation and mitochondrial energy state.

Chapter 5 presented the hemodynamic responses and tissue morphology of *in vivo* liver tissue during hepatic ischemia-reperfusion of rats, induced by portal triad occlusion using a RGB color camera. In this chapter the emphasis is put on the investigation of a method for visualizing the concentrations of oxygenated hemoglobin (C_{HbO}), deoxygenated hemoglobin (C_{HbR}), total hemoglobin (C_{HbT}), tissue oxygen saturation (StO_2), and scattering power (b) in liver tissue derived from RGB images. This method was applied to imaging hemodynamics of liver tissue during pathophysiologic events such as hepatic inflow occlusion and subsequent reperfusion. In the proposed method the RGB values were converted into the tristimulus values using a color transformation matrix. A Monte Carlo simulation (MCS) model of light transport for tissue was applied to determine the relationship among the tristimulus values and the concentrations of oxyhemoglobin, deoxyhemoglobin and scattering power b. Images of total hemoglobin concentration and tissue oxygen saturation are

reconstructed from the results of oxygenated hemoglobin and deoxygenated hemoglobin concentrations. *In vivo* experimental results of C_{HbO}, C_{HbR}, C_{HbT}, and StO_2 for rat liver exhibited the ability of the method to approximated the changes in hemodynamics of liver tissue during ischemia-reperfusion. Accordingly, we found that ischemia-reperfusion driven changes in chromophore concentrations and tissue oxygen saturation are associated with spatial heterogeneity in perfusion of liver lobule which ultimately alters the hemodynamics in liver tissue. The change in average scatterers size with hepatic ischemia and/or anoxia is characterized by the change in scattering power *b*, suggests the morphological degeneration in the cellular and subcellular structures evoked by ischemia or anoxia. The ability of RGB color imaging to assess the hemodynamic responses and tissue morphology following hepatic ischemia-reperfusion would provide important diagnostic information to the extent of ischemia-reperfusion injury resulting from liver transplantation or resection surgery.

This thesis emphasizes on applications of diffuse reflectance spectroscopy for the detection of hepatic ischemia-reperfusion. Reflectance spectroscopy in the visible part of the spectrum has been proved to be a valuable tool in the diagnostics of liver pathophysiology. The usefulness of the proposed method are its directness and portability, because the only devices needed are a white light source, fiber optics, and two spectrometers. Besides, the noninvasive RGB imaging method presented in this dissertation can be used to simultaneously evaluate spatial and temporal changes in hepatic hemodynamic parameters and tissue morphology. The above studies show the potential of diffuse reflectance spectroscopy and RGB imaging to assess hepatic hemodynamics as an indicator of hepatic tissue viability in liver transplantation. The experiment has evolved from single point measurement using reflectance fiber probe based spectroscopy to RGB imaging, presenting a possibility of spatial analyzes of the chromophore content, tissue oxygen saturation, and scattering power in the liver tissue.

Future research could build upon this dissertation in several directions. For example, if the imaging technique can be adopted to take both scattering amplitude and scattering power into account, this could be used for estimating reduced scattering coefficient of liver tissue to identify the normal hepatic texture and any irregularity due to pathologic conditions. Further, special interest should be paid for multispectral/hyperspectral imaging of *in vivo* liver tissue to improve monitoring of chromophore concentrations and scattering parameters. In addition, the experimental setup must be further improved with a view to lessen acquisition times, increase the accessibility, improve the algorithms and ultimately acquire measurements with high specificity and sensitivity to scope the clinical settings where a need exists for microcirculatory assessment.

Acknowledgement

I would like to acknowledge the amazing mentorship that I received from my research Advisor Dr. Izumi Nishidate during my study at Tokyo University of Agriculture and Technology. Dr. Nishidate was always a patient and kind mentor who I can thank for helping me get into TUAT. The mentoring I received from him in my formative years of graduate school helped me grow and identify my strengths and weaknesses which will lead me towards my future goals. I am extremely fortunate to have had the chance of learn from him, not only in the professional realm but also personally. I am deeply appreciative. I am ever thankful to Dr. Toshiaki Iwai for his support, persistent inspiration and always keeping me motivated in my studies. Also, I owe a big thanks to Dr. Shunichi Sato and Dr. Satoko Kawauchi for their cooperation and contributions, their technical guidance led me past many difficulties. I also wish to thank all my co-authors for their cooperation and contribution in my work. I want to acknowledge Dr. Nakano for his scientific input, concise and insightful comments. I wish to give my thanks to all of my lab mates; working with them was not only enjoyable, but enlightening. Never have I had the opportunity to work with a group of such intelligent individuals who were always ready to lend a helping hand. Finally, but most importantly, I want to thank my parents and my husband for their love and support. Each of you have been encouraging me tremendously in this long path to the Ph.D.

Sharmin Akter

Bibliography

[1] T. J. Farrell, M. S. Patterson, and B. Wilson, "A diffusion theory model of spatially resolved, steady-state diffuse reflectance for the noninvasive determination of tissue optical properties in vivo," *Med Phys*. **19**(4), 879-888 (1992).

[2] N. Yoroslavsky, A. V. Priezzhev, J. Rodriguez, I. V. Yoroslavsky, and H. Battarbee, "Optics of Blood," in *Handbook of Optical Biomedical Diagnostics*, V. V. Tuchin, ed. (SPIE- The International Society for Optical Engineering, Bellingham, 2002).

[3] S. Chandrasekhar, *Radiative Transfer* (Courier Dover Publications, 1960).

[4] L. Wang, and H. Wu, *Biomedical Optics: Principles and Imaging* (John Wiley & Sons, Inc., Hoboken, 2007).

[5] Z. Guo, S. K. Wan, K. Kim, and C. Kosaraju, "Comparing diffusion approximation with radiative transfer analysis for light transport in tissues," *Optical Review*. **10**(5) 415-421 (2003).

[6] H. Gandjbakhche, G. H. Weiss, R. F. Bonner, and R. Nossal, Phys. Rev. **E48**, 810-818 (1993).

[7] W. F. Cheong, S. A. Prahl, and A. J. Welch, "A review of the Optical-properties of Biological Tissues", *IEEE Journal of Quantum Electronics*, **26**(12), 2166-2185 (1990).

[8] Ciani, K.-U. Goss, and R. P. Schwarzenbach, "Light penetration in soil and particulate minerals," Eur. J. Soil Sci. **56**(5), 561–574 (2005).

[9] G. Osborne, T. Fearn, and P. H. Hindle, "Practical NIR Spectroscopy with Applications in Food and Beverage Analysis", Longman Publishing Group, Harlow, 2nd edition (1993).

[10] G. M. Palmer, and N. Ramanujam, "Monte Carlo-based inverse model for calculating tissue optical properties. Part I: Theory and validation on synthetic phantoms," *Appl Opt*. **45**, 1062-1071 (2006).

[11] B. C. Wilson, and G. Adam, "A Monte Carlo model for the absorption and flux distributions of light in tissue," *Medical Physics*. **10,** 824 (1983).

[12] T. J. Pfefer, L. S. Matchette, C. L. Bennett, J. A. Gall, J. N. Wilke, A. J. Durkin, and M. N. Ediger, "Reflectance-based determination of optical properties in highly attenuating tissue," *J Biomed Opt*. **8,** 206-215 (2003).

[13] Ungut, G. Grehan, and G. Gouesbet. Comparisons between geometrical optics and lorenz-mie theory. *Applied Optics*. 20(17), 2911-2918 (1981).

[14] L. T. Perelman, V. Backman, M. Wallace, G. Zonios, R. Manoharan, A. Nusrat, S. Shields, M. Seiler, C. Lima, T. Hamano, et al., "Observation of periodic fine structure in reflectance from biological tissue: A new technique for measuring nuclear size distribution," *Phys. Rev. Lett.* **80**(3), 627-630 (1998).

[15] S. J. Matcher, "Signal Quantification and Localization in Tissue Near-Infrared Spectroscopy," in *Handbook of Optical Biomedical Diagnostics*, V. V. Tuchin, ed. (SPIE - The International Society for Optical Engineering, Bellingham, 2002).

[16] B. J. Tromberg, O. Coquoz, J. B. Fishkin, T. Pham, E. R. Anderson, J. Butler, M. Cahn, J. D. Gross, V. Venugopalan, and D. Pham, "Non-invasive measurements of breast tissue optical properties using frequency-domain photon migration," *Philos Trans R Soc Lond B Biol Sci*. **352,** 661-668 (1997).

[17] B. J. Tromberg, N. Shah, R. Lanning, A. Cerussi, J. Espinoza, T. Pham, L. Svaasand, and J. Butler, "Non-invasive in vivo characterization of breast tumors using photon migration spectroscopy," *Neoplasia* **2**, 26-40 (2000).

[18] M. S. Patterson, B. Chance, and B. C. Wilson, "Time resolved reflectance and transmittance for the non-invasive measurement of optical properties", *Appl. Opt.* **28,** 2331-2336 (1989).

[19] D. T. Delpy, M. Cope, P. van der Zee, S. Wray, and J. Watt, "Estimation of optical pathlength through tissue from direct time of flight measurement", *Phys. Med. Biol.* **33,** 1433-1442 (1988).

[20] J.H. Pringle, "Notes on the arrest of hepatic haemorrhage due to trauma", *Ann. Surg*. **48,** 541-549 (1908).

[21] C. Huguet, A. Gavelli, P. A. Chieco, S. Bona, J. Harb, J.M. Joseph, J. Jobard, M. Gramaglia, and M. Lasserre "Liver ischemia for hepatic resection: where is the limit?", *Surgery*. **11,** 251-259 (1992).

[22] C. Peralta, M.B. Jiménez-Castro, and J Gracia-Sancho, "Hepatic ischemia and reperfusion injury: effects on the liver sinusoidal milieu", *J Hepatol.* **59**(5), 1094-106 (2013).

[23] Y. Zhai, H. Petrowsky, J.C. Hong, R. W. Busuttil, and J.W. Kupiec-Weglinski, "Ischemia-reperfusion injury in liver tissue transplantation--from bench to bedside", *Nat Rev Gastroenterol Hepatol*. **10**(2), 79-89 (2013).

[24] J.S. Soares, I Barman, N.C. Dingari, Z. Volynskaya, W. Liu, N. Klein, D. Plecha,R. R. Dasari, and M. Fitzmaurice, "Diagnostic power of diffuse reflectance spectroscopy for targeted detection of breast lesions with microcalcifications", *Proc Natl Acad Sci USA*. **110**(2), 471-6 (2013).

[25] J. W. W. F. Cheong, and S. A. Prahl, "A review of the optical properties of biological tissue," 1990.

[26] R. R. Anderson, and J. A. Parrish, “Optical Properties of Human Skin,” in The Science of Photomedicine, J. D. Regan and J. A. Parrish, eds. 1982, Plenum Press: New York. pp. 147-194.

[27] P. Bouguer, “Essai d’ optiquesur la graduationde la lumiere, Jombert, Paris,” 1729.

[28] J. H. Lambert, “Photometria sive de mensure et gradibus luminis, colorum et umbrae, Klett, Augsberg,” 1760.

[29] Beer, “Bestimmung der absorptiondes rothen lichts in farbien Flüssigkeiten,” *Annalen der Physik*, vol. **86**, (1852) pp. 74-88.

[30] F. Bohren, and D. R. Huffman, “Absorption and scattering of light by small particles” John Wiley and Sons, 2008.

[31] J. Mobley and T. Vo-Dinh, “Optical Properties of Tissue”, in Biomedical photonics handbook, T. Vo-Dinh, ed.2003, CRC Press: Boca Raton, Fla. p. 2-1-2-75.

[32] W. P., “Approximation formulae for the light scattering coefficient of dielectric spheres,” *Brit. J. Appl. Phys*. 15, July 1964.

[33] M. G., “Contribution to the optical properties of turbid media, in particular of colloidal suspensions of metals,” *Ann. Phys*. (Leipzig), 1908.

[34] L. G. Henyey, and J. L. Greenstein, “Diffuse radiation in the galaxy”, *Astrophys. J*. **93,** (1941) 70-83.

[35] H. F. Bunn, and B. G. Forget, “Hemoglobin: molecular, genetic and clinical aspects”, pp. 690, Saunders, Philadelphia, 1986.

[36] S. A. Prahl, “Tabulated Molar Extinction Coefficient for Hemoglobin in Water,” http://omlc.ogi.edu/spectra/hemoglobin/summary.html (1999).

[37] W. G. Zijlstra, A. Buursma, and O. W. van Assendelft, “Visible and Near Infrared Absorption Spectra of Human and Animal Haemoglobin”, pp. 368, VSP BV, Leiden, The Netherlands, 2000.

[38] R. L. Bick, J. M. Bennet, R. K. Brynes, M. J. Cline, L. Kass, G. Murano, S. B. Shoet, and P. C. J. Ward, eds. "Hematology: clinical and laboratory practice", Vol. 1. 1993, Mosby: St. Louis. p. 3-852.

[39] R. A. Capaldi, "Structure and function of cytochrome c oxidase", *Annu Rev. Biochem*. **59,** 569-596 (1990).

[40] P. Rolfe, "In vivo near-infrared spectroscopy", *Annu. Rev Biomed Engin*. **2,** 715-754 (2000).

[41] F. F. Jöbsis-VanderVliet, C. A. Piantadosi, A. L. Sylvia, S. K. Lucas, and H. H. Keizer, "Near-infrared monitoring of cerebral oxygen sufficiency. I. Spectra of cytochrome c oxidase", *Neurological research*. **10**(1), 7-17 (1988).

[42] F. F. Jobsis et al., "Reflectance spectrophotometry of cytochrome aa3 in vivo," *J. Appl. Physiol.* **43**(5), 858-872 (1977).

[43] C. E. Cooper, M. Cope, V. Quaresima, M. Ferrari, E. Nemoto, R. Springett, S. Matcher, P. Amess, J. Penrice, L. Tyszczuk, J. Wyatt, and D. T. Dely, "Measurement of cytochrome oxidase redox state by near infrared spectroscopy", *Optical Imaging of Brain Function and Metabolism*. **2** 413, 63-73 (1997).

[44] E. Marieb, Human Anatomy and Physiology, 1995.

[45] F. P. Bolin, L. E. Preuss, R. C. Taylor, and R. J. Ference, "Refrective index of some mammalian tissue using a fiber optic cladding method," *Appl. Opt*. **28,** (1989).

[46] S. T. Flock, B. C. Wilson, and M. S. Patterson, "Total attenuation coefficients and scattering phase functions of tissues and phantom materials at 633 nm," *Med. Phys*. **14**, (1987).

[47] R. A. Johnson, and G. K. Bhattacharjee, "Statistics Principles and Methods" (Wiley, New York, 1996) 3rd ed.

[48] L-H. Wang, S. L. Jacques, and L-Q Zheng, "MCML- Monte Carlo modeling of photon transport in multi-layered tissues," *Comput. Methods Programs Biomed*. **47,** 131-146 (1995).

[49] S. A. Prahl, M. Keijzer, S. L. Jacques, and A. J. Welch, "A Monte Carlo model of light propagation in tissue," SPIE Institute Series IS5, 102-111 (1989).

[50] L. L. Carter, and E. D. Cashwell, "Particle-Transport Simulation with the Monte Carlo Method", Oak Ridge: USERDA Technical Information Center (1975).

[51] A Roggan, M. Friebel, K. Dörschel, A. Hahn, and G. Muller, "Optical properties of circulating human blood in the wavelength range 400-2500 nm," *J. Biomed Opt*. **4**, 36-46 (1999).

[52] S. J. Dam, T. Dalgaard, P. E. Fabricious, and S. Andersson-Engels, "Multiple polynomial method for determination of biomedical optical properties from integrating sphere measurements," *Appl. Opt*. **7,** 1202-1209 (2000).

[53] R.W.G. Hunt "Measuring Colour," (Fountain Press, Kingston-upon-Thames, England, 1998) 3rd ed.

[54] G. Wyszecki and W. S. Stiles "Color Science Concepts and Methods, Quantitative Data and Formulae," (John Wiley & Sons, New York, 1982).

[55] J. W. Kupiec-Weglinski, and R.W. Busuttil "Ischemia and reperfusion injury in liver transplantation," *Transplant Proc*. **37**(4), 1653-1656 (2005).

[56] M. Kretzschmar, A. Krüger, and W. Schirrmeister, "Hepatic ischemia-reperfusion syndrome after partial liver resection (LR): hepatic venous oxygen saturation, enzyme pattern, reduced and oxidized glutathione, procalcitonin and interleukin-6," *Exp Toxicol Pathol.* **54**(5-6), 423-431 (2003).

[57] S. H. Tseng, C. K. Hsu, J. Yu-Yun Lee, S. Y. Tzeng, W. R. Chen, and Y. K. Liaw, "Noninvasive evaluation of collagen and hemoglobin contents and scattering property

of in vivo keloid scars and normal skin using diffuse reflectance spectroscopy: pilot study," *J Biomed Opt*. 17(7), 077005 (2012).

[58] D. Fabila, J. M. de la Rosa, S. Stolik, E. Moreno, K. Suárez-Álvarez, G. López-Navarrete, C. Guzmán, J. Aguirre-García, C. Acevedo-García, D. Keshenobich, and G. Escobedo, "In vivo assessment of liver fibrosis using diffuse reflectance and fluorescence spectroscopy: a proof of concept," *Photodiagnosis Photodyn Ther*. 9(4), 376-382 (2012).

[59] T. Kitai, A. Tanaka, A Tokuka, B. Sato, S. Mori, N. Yanabu, T. Inomoto, S. Umeto, K. Tanaka, and Y. Yamaoka, "Intraoperative measurement of the graft oxygenation state in living related liver transplantation by near infrared spectroscopy," *Transplant.Int.* **8**(2), 111-118 (1995).

[60] T. Kitai, A. Tanaka, A. Tokuka, K. Tanaka, Y. Yamaoka, K. Ozawa, and K. Hirao, "Quantitative detection of hemoglobin saturation in the liver with near-infrared spectroscopy," *Hepatology* **18**(4), 926-936 (1993).

[61] E. EI-Desoky, D. T. Delpy, B. R. Davidson, and A. M. Seifalian, "Assessment of hepatic ischaemia reperfusion injury by measuring intracellular tissue oxygenation using near infrared spectroscopy," *Liver* **21**(1), 37-44 (2001).

[62] L. Sikurova, P. Balis, and M. Zvarik, "Penetration of laser light through red blood cell ghosts," *J Photochem Photobiol B.* **103**(3), 230-233 (2011).

[63] R Nachabé, B. H. Hendriks, A. E. Desjardins, M. van der Voort, M. B. van der Mark, and H. J. Sterenborg, "Estimation of lipid and water concentrations in scattering media with diffuse optical spectroscopy from 900 to 1,600 nm," *J Biomed Opt.* **15**(3):037015 (2010).

[64] D. J. Evers, R. Nachabé, D. Hompes, F. van Coevorden, G. W. Lucassen, B. H. Hendriks, M. L. van Velthuysen, J. Wesseling, and T. J. Ruers,

"Optical sensing for tumor detection in the liver," *Eur J Surg Oncol.* **39**(1), 68-75 (2013).

[65] Y. Fawzy, M. Petek, M. Tercelj and H. Zeng, "*In vivo* assessment and evaluation of lung tissue morphologic and physiological changes from noncontact endoscopic reflectance spectroscopy for improving lung cancer detection," *J Biomed Opt.* **11**(4), 044003 (2006).

[66] J. B. Fishkin, O. Coquoz, E. R. Anderson, M. Brenner, and B. J. Tromberg, "Frequency-domain photon migration measurements of normal and malignant tissue optical properties in a human subject," *Appl. Opt.* **36**(1), 10-20 (1997).

[67] G. Yoon, D. N. Ghosh Roy and R. C. Straight, "Coherent backscattering in biological media: measurement and estimation of optical properties," *Appl. Opt.* **32**(4) 580–585 (1993).

[68] S. A. Prahl and I. A. Vitkin, "Determination of optical properties of turbid media using pulsed photothermal radiometry," *Phys. Med. Biol.* **37**(6) 1203–1217 (1992).

[69] L. Wang and S. L. Jacques, "Use of a laser beam with an oblique angle on incidence to measure the reduced scattering coefficient of a turbid medium," *Appl. Opt.* **34**(13), 2362-2366 (1995).

[70] Kienle, L. Lilge, M. S. Patterson, R. Hibst, R. Steiner, and B. C. Wilson, "Spatially resolved absolute diffuse reflectance measurements for noninvasive determination of the optical scattering and absorption coefficients of biological tissue," *Appl. Opt.* **35**(13), 2304-2314 (1996).

[71] S.-P. Lin, L.-H. Wang, S. L. Jacques, and F. K. Tittel, "Measurement of tissue optical properties by the use of oblique-incidence optical fiber reflectometry," *Appl. Opt.* **36**(1), 136-143 (1997).

[72] T. M. Bydlon, R. Nachabé, N. Ramanujam, H. J. Sterenborg, and B. H. Hendriks, "Chromophore based analyses of steadystate diffuse reflectance spectroscopy: current status and perspectivesfor clinical adoption," *J Biophotonics.* **8**(1-2), 9-24 (2015).

[73] S. Kennedy, J. Geradts, T. Bydlon, J. Q. Brown, J. Gallagher, M. Junker, W. Barry, N. Ramanujam, and L. Wilke, "Optical breast cancer margin assessment: an observational study of the effects of tissue heterogeneity on optical contrast," *Breast Cancer Res.* **12**(6), R91 (2010).

[74] M. D. Keller, S. K. Majumder, M. C. Kelley, I. M. Meszoely, F. I. Boulos, G. M. Olivares, A. Mahadevan-Jansen, "Autofluorescence and diffuse reflectance spectroscopy and spectral imaging for breast surgical margin analysis," *Lasers Surg Med.* **42**(1), 15–23 (2010).

[75] J. Brown, L. Wilke, J. Geradts, S. Kennedy, G. Palmer, and N. Ramanujam, "Quantitative optical spectroscopy: a robust tool for direct measurement of breast cancer vascular oxygenation and total hemoglobin content *in vivo*," *Cancer Res.* **69**(7), 2919–2926 (2009).

[76] P. R. Bargo, S. A. Prahl, T. T. Goodell, R. A. Sleven, G. Koval, G. Blair, and S. L. Jacques, "*In vivo* determination of optical properties of normal and tumor tissue with white light reflectance and empirical light transport model during endoscopy," *J. Biomed. Opt.* **10**(3), 034018 (2005).

[77] S. Kawauchi, S. Sato, H. Ooigawa, H. Nawashiro, M. Ishihara, and M. Kikuchi, "Simultaneous measurement of changes in light absorption due to the reduction of cytochrome c oxidase and light scattering in rat brains during loss of tissue viability," *Appl. Opt.* **47**(22), 4164-4176 (2008).

[78] C. Hsu, M. Razavi, S. So, I. H. Parachikov, and D. A. Benaron, "Liver tumor gross margin identification and ablation monitoring during liver radiofrequency treatment," *J. Vasc. Interv Radiol.* **16**(11), 1473–8 (2005).

[79] S. Wong, P. Mangu, and M. Choti, "American Society of Clinical Oncology 2009 clinical evidence reviewon radiofrequency ablation of hepatic metastases from colorectal cancer," *J. Clin. Oncol.* **28**(3), 493–508 (2010).

[80] T. M. Pawlik, C. R. Scoggins, D. Zorzi, E. K. Abdalla, A. Andres, C. Eng, S. A. Curley, E. M. Loyer, A. Muratore, G. Mentha, L. Capussotti, and J. N. Vauthey, "Effect of surgical margin status on survival and site of recurrence after hepatic resection for colorectal metastases," *Ann. Surg.* **241**(5), 715–722 (2005).

[81] B. Nordlinger, H. Sorbye, and B. Glimelius, et al., "Perioperative chemotherapy with FOLFOX4 and surgery versus surgery alone for resectable liver metastases from colorectal cancer (EORTC Intergroup trial 40983): a randomised controlled trial," *Lancet* **371**(9617), 1007–1016 (2008).

[82] Muratore, D. Ribero, G. Zimmitti, A. Mellano, S. Langella, and L. Capussotti, "Resection margin and recurrence-free survival after liver resection of colorectal metastases," *Ann. Surg. Oncol.* **17**(5), 1324–1329 (2010).

[83] R. Karakas, A. Sircan-Kücüksayan, O. E. Elpek, and M. Canpolat, "Investigating viability of intestine using spectroscopy: a pilot study," *J. Surg. Res.* **191**(1) 91-8 (2014).

[84] Yu, H. Fu, T. Bydlon, J. E. Bender, and N. Ramanujam, "Diffuse reflectance spectroscopy with a self-calibrating fiber optic probe," *Opt. Letters* **33**(16), 1783-1785 (2008).

[85] J. Y. Lo, B. Yu, H. L. Fu, J. E. Bender, G. M. Palmer, T. F. Kuech, and N. Ramanujam, "A strategy for quantitative spectral imaging of tissue absorption and scattering using light emitting diodes and photodiodes," *Opt. Express* **17**(3), 1372-1384 (2009).

[86] Kim, M. Roy, F. Dadani, and B. C. Wilson, "A fiber optic reflectance probe with multiple source-collector separations to increase the dynamic range of derived tissue optical absorption and scattering coefficients," *Opt. Express* **18**(6), 5580-5594 (2010).

[87] Nishidate, C. Mizushima, K. Yoshida, S. Kawauchi, S. Sato, and M. Sato, "*In vivo* estimation of light scattering and absorption properties of rat brain using a single-reflectance fiber probe during cortical spreading depression," *J. Biomed. Opt.* **20**(2), 027003 (2015).

[88] H. J. van Staveren, C. J. Moes, J. van Marie, S. A. Prahl, and M. J. Gamert, "Light scattering in Intralipid-10% in the wavelength range of 400–1100 nm," *Appl. Opt.* **30**(31), 4507-4514 (1991).

[89] D.C. Wharton and A. Tzagoloff, "Studies on the electron transfer system. LVII. The near infrared absorption band of cytochrome oxidase," *J. Biol. Chem.* **239**(6), 2036-2041(1964).

[90] J. H. Dong, X. D. He, K. Li, H. C. Duan, Z. M. Peng, and J. X. Cai, "Tolerance limit of rats to normothermic hepatic inflow occlusion under portal blood bypass," *Hepatobiliary Pancreat. Dis. Int.* **1**(1), 57–62 (2002).

[91] T. Kitai, M. Miwa, H. Liu, B. Beauvoit, B. Chance, and Y. Yamaoka, "Application of near-infrared time-resolved spectroscopy to rat liver--a preliminary report for surgical application," *Phys. Med. Biol.* **44**(8), 2049-2061 (1999).

[92] B. I. Sykes, E. Penny, and F. H. Purchase, "Hepatocyte vacuolation and increased liver weight occurring in anoxic rat," *Toxicol. Appl. Pharmacol.* 36, 31-39 (1976).

[93] A. Trowell, "The experimental production of watery vacuolation of the liver," *J. Physiol.* **105**, 268-297 (1946).

[94] X. Li, M. R. Elwell, A. M. Ryan, and R. Ochoa, "Morphogenesis of postmortem hepatocyte vacuolation and liver weight increases in Sprague-Dawley rats," *Toxicol. Pathol.* **31**, 682-688 (2003).

[95] C. H. Li, H. D. Wang, J. j. Hu, X. L. Ge, K. Pan, A. Q. Zhang, and J. H. Dong, "The monitoring of microvascular liver blood flow changes during ischemia and reperfusion using laser speckle contrast imaging," *Microvasc. Res.* **94** 28–35 (2014).

[96] C. K. Sun, X. Y. Zhang, A. Zimmermann, G. Davis, and A. M. Wheatley, "Effect of ischemia-reperfusion injury on the microcirculation of the steatotic liver of the Zucker rat," *Transplantation* **72**(10), 1625-1631 (2010).

[97] C. E. Cooper and R. Springett, "Measurement of cytochrome oxidase and mitochondrial energetics by near-infrared spectroscopy," *Philos. Trans. R. Soc.* **B352**(1354), 669-676(1997).

[98] C. E. Cooper, M. Cope, V. Quaresima, M. Ferrari, E. Nemoto, R. Springett, S. Matcher, P. Amess, J. Penrice, L. Tyszczuk, J. Wyatt, and D. T. Delpy, "Measurement of cytochrome oxidase redox state by near infrared spectroscopy," *Adv. Exp. Med. Biol.* **413**, 63-73 (1997).

[99] T. Kondo, T. Todoroki, T. Hirano, F. W. Schildberg, and K. Messmer, "Impact of ischemia-reperfusion injury on dimensional changes of hepatic microvessels," *Res. Exp. Med.* (Berl). **198**(2), 63-72 (1998).

[100] B. Vollmar, J. Glasz, S. Post, and M. D. Menger, "Role of microcirculatory derangements in manifestation of portal triad cross-clamping-induced hepatic reperfusion injury," *J. Surg. Res.* **60**(1), 49–54 (1996).

[101] V. Tuchin, [Tissue Optics: Light Scattering Methods and Instruments for Medical Diagnosis, 2nd ed.], SPIE Press, Bellingham, WA, 2007.

[102] S. L. Jacques and S. A. Prahl, "Some biological scatteres," 1998, http://omlc.org/classroom/ece532/class3/scatterers.html (13 August 2014).

[103] H. Fang, M. Ollero, E. Vitkin, L. M. Kimerer, P. B. Hanlon, and L. T. Prelman, "Noninvasive sizing of subcellular organelles with light scattering spectroscopy, *IEEE J. Sel. Top. Quantum. Electron.* **9**(2), 267-276 (2003).

[104] J. R. Mourant, J. P. Freyer, A. H. Hielscher, A. A. Eick, D. Shen, and T. M. Johnson, "Mechanisms of light scattering from biological cells relevant to noninvasive optical-diagnostics," *Appl. Opt.* **37**(16), 3586-3593 (1998).

[105] B. González-Flecha, J. C. Cutrin, and A. Boveris, "Time course and mechanism of oxidative stress and tissue damage in rat liver subjected to *in vivo* ischemia-reperfusion," *J Clin Invest.* **91**(2), 456-64 (1993).

[106] S. Suzuki, L. H. Toledo-Pereyra, and F. J. Rodriguez, "Role of neutrophils during the first 24 hours after liver ischemia and reperfusion injury," *Transplant Proc.* **26**(6), 3695-700 (1994).

[107] R. M. Goldstein, C. L. Secrest, G. B. Klintmalm, and B. S. Husberg, "Problematic vascular reconstruction in liver transplantation. Part I. Arterial", *Surgery* **107**(5) 540-543 (1990).

[108] D. M. Payen, M. D. Fratacci, P. Dupuy, C. Gatecel, C. Vigouroux, Y. Ozier, D. Houssin, and Y. Chapuis, "Portal and hepatic arterial blood flow measurement of human transplanted livers by implanted Doppler probes: interest for early complications and nutrition," *Surgery* **107**(4), 540-543 (1990).

[109] R. Cursio, P. Colosetti, M. C. Saint-Paul, S. Pagnotta, P. Gounon, A. Iannelli, P. Auberger, and J. Gugenheim, "Induction of different types of cell death after normothermic liver ischemia-reperfusion," *Transplant Proc.* **42**(10), 3977-3980 (2010).

[110] T. Kiuchi, H. J. Schlitt, K. J. Oldhafer, B. Nashan, A. Tanaka, K. Wonigeit, B. Ringe, K. Tanaka, Y. Yamaoka, and R. Pichlmayr, "Early acute rejection after hepatic graft reperfusion: association with ischemic injury with good function, oxygenation heterogeneity, and leukocyte adhesion without aggregation," *Transplant Proc.* **29**(1-2), 364-365 (1997).

[111] H. de Groot and T. Noll, "Halothane-induced lipid peroxidation and glucose-6-phosphatase inactivation in microsomes under hypoxic conditions," *Anesthesiology* **62**(1), 44-48 (1985).

[112] N. S. Chandel, G. R. Budinger, S. H. Choe, and P. T. Schumacker, "Cellular respiration during hypoxia. Role of cytochrome oxidase as the oxygen sensor in hepatocytes," *J. Biol. Chem.* **272**(30), 18808–18816 (1997).

[113] N. Sato, N. Hayashi, S. Kawano, T. Kamada, and H. Abe, "Hepatic hemodynamics in patients with chronic hepatitis or cirrhosis as assessed by organ-reflectance spectrophotometry," *Gastroenterology* **84**(3), 611-616 (1983).

[114] S. Akter, S. Maejima, S. Kawauchi, S. Sato, A. Hinoki, S. Aosasa, J. Yamamoto, and I. Nishidate, "Evaluation of light scattering and absorption properties of *in vivo* rat liver using a single-reflectance fiber probe during preischemia, ischemia-reperfusion, and postmortem," *J. Biomed. Opt.* **20**(7), 076010 (2015).

[115] "CytochromeSpectra," http://www.ucl.ac.uk/medphys/research/borl/intro/spectra (2005).

[116] Y. Hoshi, O. Hazeki, Y. Kakihana, and M. Tamura, "Redox behavior of cytochrome oxidase in the rat brain measured by near-infrared spectroscopy," *J. Appl. Physiol.* **83**(6), 1842-1848 (1997).

[117] K. Chun, J. Zhang, J. Biewer, D. Ferguson, and M. G. Clemens, "Microcirculatory failure determines lethal hepatocyte injury in ischemia/reperfused rat livers," *Shock*. **1**(1), 3-9 (1994).

[118] M. Goto, S. Kawano, H. Yoshihara, Y. Takei, T. Hijioka, H. Fukui, T. Matsunaga, M. Oshita, T. Kashiwagi, H. Fusamoto, et al., "Hepatic tissue oxygenation as a predictive indicator of ischemia-reperfusion liver injury," *Hepatology*. **15**(3), 432-437 (1992).

[119] D. Abookasis, C. C. Lay, M. S. Mathews, M. E. Linskey, R. D. Frostig, and B. J. Tromberg, "Imaging cortical absorption, scattering, and hemodynamic response during ischemic stroke using specially modulated near-infrared illumination," *J Biomed Opt*. **14**(2), 024033 (2009).

[120] X. Wang, B. W. Pogue, S. Jiang, X. Song, K. D. Paulsen, C. Kogel, S. P. Poplack, and W. A. Wells, "Approximation of Mie scattering parameters in near-infrared tomography of normal breast tissue in vivo," *J Biomed Opt*. **10**(5), 051704 (2005).

[121] J. R. Mourant, T. Fuselier, J. Boyer, T. M. Johnson, and I. J. Bigio, "Predictions and measurements of scattering and absorption over broad wavelength ranges in tissue phantoms," *Appl Opt*. **36**(4), 949-957 (1997).

[122] S. Marubayashi, M. Takenaka, K. Dohi, H. Ezaki, and T. Kawasaki, "Adenine nucleotide metabolism during hepatic ischemia and subsequent blood reflow periods and its relation to organ viability," *Transplantation*. **30**(4), 294-296 (1980).

[123] W. Kamiike, M. Nakahara, K. Nakao, M. Koseki, T. Nishida, Y. Kawashima, F. Watanabe, and K. Tagawa, "Correlation between cellular ATP level and bile excretion in the rat liver," *Transplantation*. **39**(1), 50-55, (1985).

[124] J. J. Lemasters, H. Bunzendahl, and R. G. Thurman, "Reperfusion injury to donor livers stored for transplantation," *Liver Transpl Surg*. **1**(2), 124-138 (1995).

[125] S. Akter, T. Tanabe, S. Maejima, S. Kawauchi, S. Sato, A. Hinoki, S. Aosasa, J. Yamamoto, and I. Nishidate, "In vivo estimation of optical properties of rat liver using single-reflectance fiber probe during ischemia and reperfusion," *Optical Review*. **22**(6), 1-6 (2015).

[126] Nishidate, N. Tanaka, T. Kawase, T. Maeda, T. Yuasa, Y. Aizu, T. Yuasa, and K. Niikeji, "Noninvasive imaging of human skin hemodynamics using a digital red-green-blue camera," *J Biomed Opt*. **16**(8), 086012 (2011).

[127] K. Yoshida, I. Nishidate, T. Ishizuka, S. Kawauchi, S. Sato, M. Sato, "Multispectral imaging of absorption and scattering properties of in vivo exposed rat brain using a digital red-green-blue camera", *J Biomed Opt*. **20**(5) 051026 2015.

[128] Nishidate, T. Ishizuka, A. Mustari, K. Yoshida, S. Kawauchi, S. Sato, and M. Sato, "Evaluation of Cerebral Hemodynamics and Tissue Morphology of In Vivo Rat Brain Using Spectral Diffuse Reflectance Imaging," *Appl Spectrosc*. 2016. [Epub ahead of print].

[129] Koo, I. Y. Liang, and K. K. Cheng, "The terminal hepatic microcirculation in the rat," *Q J Exp Physiol Cogn Med Sci*. **60**(4), 261-266 (1975).

[130] M. D. Menger, M. Rücker, and B. Vollmar, "Capillary dysfunction in striated muscle ischemia/reperfusion: on the mechanisms of capillary "no-reflow"," *Shock*. **8**(1), 2-7 (1997).

[131] B. Vollmar, J. Glasz, R. Leiderer, S. Post, and M. D. Menger, "Hepatic microcirculatory perfusion failure is a determinant of liver dysfunction in warm ischemia-reperfusion," *Am J Pathol*. **145**(6), 1421-1431 (1994).

[132] F. J. Burczunski, B. A. Luxon, and R. A. Weisiger, "Intrahepatic blood flow distribution in the perfused rat liver: effect of hepatic artery perfusion," *Am J Physiol*. **271**(4 pt 1), G561-7 (1996).

[133] M. N. Tawadrous, X. Y. Zhang, and A. M. Wheatley, "Microvascular origin of laser Doppler flux signal from the surface of normal and injured liver of the rat," *Microvasc Res*. **62**(3), 355-65 (2001).

[134] M. G. Clemens, P. F. McDonagh, I. H. Chaudry, and A. E. Baue, "Hepatic microcirculatory failure after ischemia and reperfusion: improvement with ATP-$MgCl_2$ treatment," *Am J Physiol*. **248** (6 Pt 2), H804-11 (1985).

[135] R. M. Zwacka, Y. Zhang, W. Zhou, J. Halldorson, and J. F. Engelhardt, "Ischemia/reperfusion injury in the liver of BALB/c mice activates AP-1 and nuclear factor kappaB independently of IkappaB degradation," *Hepatology*. **28**(4), 1022-1030 (1998).

[136] M. Ohkawa, I. H. Chaudry, M. G. Clemens, and A. E. Baue, "ATP-$MgCl_2$ produces sustained improvement in hepatic mitochondrial function and blood flow after hepatic ischemia," *J Surg Res*. **37**(3), 226-234 (1984).

[137] M. Andreen, "Inhalation versus intravenous anaesthesia. Effects on the hepatic and splanchnic circulation," *Acta Anaesthesiol Scand Suppl*. **75**, 25-31 (1982).

[138] J. C. Caldwell-Kenkel, R. T. Currin, T. Tanaka, R. G. Thurman, and J. J. Lemasters, "Reperfusion injury to endothelial cells following cold ischemic storage of rat livers," *Hepatology*. **10**(3), 292-299 (1989).

[139] Leaf, "Cell swelling. A factor in ischemic tissue injury," *Circulation*. **48**(3), 455-458 (1973).

[140] M. D. Menger, S. Pelikan, D. Steiner, and K. Messmer, "Microvascular ischemia/reperfusion injury in striated muscle: significance of "reflow-paradox," *Am J Physiol*. **263**, H1901-H1906 (1992).

[141] J. J. Lemasters and H. Jaeschke, "Apoptosis versus oncotic necrosis in hepatic ischemia/reperfusion injury," *Gastroenterology*. **125**(4), 1246-1257 (2003).

[142] K. D. Schaser, G. Puhl, B. Vollmar, M. D. Menger, J. F. Stover, K. Köhler, P. neuhaus, and U. Settmacher, "In vivo imaging of human pancreatic microcirculation and pancreatic tissue injury in clinical pancreas transplantation," *Am J Transplant*. **5**(2), 341-350 (2005).

[143] M. D. Kelly, H. Shiba, S. Nakagawa, S. Irefin, B. Eghtesad, C. Quintni, F. Aucejo, K. Hashimoto, J. J. Fung, and C. Miller, "Hepatic blood flow plays an important role in ischemia-reperfusion injury," *Liver Transpl*. **17**(12), 1448-1456 (2011).

List of Publications by the Author

[1] S. Akter, S, Maejima, S. Kawauchi, S. Sato, A. Hinoki, S. Aosasa, J. Yamamoto, and I Nishidate, "Evaluation of light scattering and absorption properties of *in vivo* rat liver using a single-reflectance fiber probe during preischemia, ischemia-reperfusion, and postmortem," **J Biomed. Opt. 20**(7), 076010 (2015).

[2] S. Akter, T. Tanabe, S. Maejima, S. Kawauchi, S. Sato, A. Hinoki, S. Aosasa, J. Yamamoto, and I. Nishidate, "*In vivo* estimation of optical properties of rat liver using single-reflectance fiber probe during ischemia and reperfusion," **Opt. Rev. 22**(6), 1-6 (2015).

[3] S. Akter, S. Kawauchi, S. Sato, S. Aosasa, J. Yamamoto, and I Nishidate, "*In vivo* imaging of hepatic hemodynamics and light scattering property during ischemia-reperfusion in rats based on spectrocolorimetry," **Biomed. Opt. Express 8**(2), 974-992 (2017).